Design and Commissioning of an XUV and Soft X-Ray FEL Pulse Shaper

Dissertation
zur Erlangung des Doktorgrades
an der Fakultät für Mathematik, Informatik und Naturwissenschaften
Fachbereich Physik
der Universität Hamburg

vorgelegt von

Leslie Lamberto Lazzarino

Hamburg

2018

Gutachter der Dissertation:	Priv. Doz. Dr. Tim Laarmann Prof. Dr. Jörg Rossbach
Zusammensetzung der Prüfungskommission:	Prof. Dr. Wolfgang Hillert Priv. Doz. Dr. Tim Laarmann Prof. Dr. Gudrid Moortgat-Pick Prof. Dr. Jörg Rossbach Prof. Dr. Michael A. Rübhausen
Vorsitzende/r der Prüfungskommission:	Prof. Dr. Michael A. Rübhausen
Datum der Disputation:	18.12.2018
Vorsitzender Fach-Promotionsausschusses PHYSIK:	Prof. Dr. Wolfgang Hansen
Leiter des Fachbereichs PHYSIK:	Prof. Dr. Michael Potthoff
Dekan der Fakultät MIN:	Prof. Dr. Heinrich Graener

Eidesstattliche Versicherung / Declaration on Oath

Hiermit versichere ich an Eides statt, die vorliegende Dissertationsschrift selbst verfasst und keine anderen als die angegebenen Hilfsmittel und Quellen benutzt zu haben.

Die eingereichte schriftliche Fassung entspricht der auf dem elektronischen Speichermedium.

Die Dissertation wurde in der vorgelegten oder einer ähnlichen Form nicht schon einmal in einem früheren Promotionsverfahren angenommen oder als ungenügend beurteilt.

Hamburg, den 21.09.2018

L'imagination gouverne le monde.

Imagination rules the world.

Napoleon Bonaparte

Contents

List of Publications

Papers

A. Azima, J. Bödewadt, O. Becker, S. Duester, N. Ekanayake, R. Ivanov, M. M. Kazemi, **L. L. Lazzarino**, C. Lechner, T. Maltezopoulos, B. Manschwetus, V. Miltchev, J. Müller, T. Plath, A. Przystawik, M. Wieland, R. Assmann, I. Hartl, T. Laarmann, J. Rossbach, W. Wurth and M. Drescher, *Direct Measurement of the Pulse Duration and Frequency Chirp of Seeded XUV Free Electron Laser Pulses*,
New Journal of Physics **20**, 013010 (2018)
DOI: 10.1088/1367-2630/aa9b4c

S. Usenko, A. Przystawik, **L. L. Lazzarino**, M. A. Jakob, F. Jacobs, C. Becker, C. Haunhorst, D. Kip and T. Laarmann, *Split-And-Delay Unit for FEL Interferometry in the XUV Spectral Range*,
Applied Sciences **7**(6), 544 (2017)
DOI: 10.3390/app7060544

S. Usenko, A. Przystawik, M. A. Jakob, **L. L. Lazzarino**, G. Brenner, S. Toleikis, C. Haunhorst, D. Kip and T. Laarmann, *Attosecond Interferometry With Self-Amplified Spontaneous Emission of a Free-Electron Laser*,
Nat. Comm. **8**, 15626 (2017)
DOI: 10.1038/ncomms15626

T. Plath, C. Lechner, V. Miltchev, P. Amstutz, N. Ekanayake, **L. L. Lazzarino**, T. Maltezopoulos, J. Bödewadt, T. Laarmann and J. Rossbach, *Mapping few-femtosecond slices of ultra-relativistic electron bunches*,
Scientific Reports **7**, 2431 (2017)
DOI: 10.1038/s41598-017-02184-3

T. Plath, P. Amstutz, J. Bödewadt, G. Brenner, N. Ekanayake, B. Faatz, K. Hacker, K. Honkavaara, **L. L. Lazzarino**, C. Lechner, T. Maltezopoulos, M. Scholz, S. Schreiber, M. Vogt, J. Zemella, and T. Laarmann, *Free-Electron Laser Multiplex driven by a Superconducting Linear Accelerator*,
J. Synchrotron Rad. **23**, 1070 (2016)
DOI: 10.1107/S1600577516009620

S. Usenko, M. Schüler, A. Azima, M. A. Jakob, **L. L. Lazzarino**, Y. Pavlyukh, A. Przystawik, M. Drescher, T. Laarmann and J. Berakdar, *Femtosecond Dynamics of Correlated Many-Body States in C_{60} Fullerenes*,
New Journal of Physics **18**, 113055 (2016)
DOI: 10.1088/1367-2630/18/11/113055

K. Hacker, R. Molo, S. Khan, **L. L. Lazzarino**, C. Lechner, Th. Maltezopoulos, T. Plath, J. Rossbach, S. Ackermann, J. Bödewadt, M. Dohlus, N. Ekanayake, T. Laarmann, H. Schlarb, *Measurement and Simulations of Seeded Electron Microbunches with Collective Effects*, Phys. Rev. ST Accel. Beams **18**, 090704 (2015)
DOI: 10.1103/PhysRevSTAB.18.090704

Conference Proceedings

J. Bödewadt, R. Assmann, N. Ekanayake, B. Faatz, I. Hartl, M. M. Kazemi, T. Laarmann, C. Lechner, A. Przystawik, Ph. Amstutz, A. Azima, M. Drescher, W. Hillert, **L. L. Lazzarino**, Th. Maltezopoulos, V. Miltchev, T. Plath, J. Rossbach, K. Hacker, S. Khan, N. Lockmann, R. Molo, *Experience in Operating sFLASH with High-Gain Harmonic Generation*,
Proc. 8th International Particle Accelerator Conference, Copenhagen, Denmark (2017)

T. Plath, S. Khan, Ph. Amstutz, **L. L. Lazzarino**, V. Miltchev, J. Rossbach, Th. Maltezopoulos, J. Bödewadt, T. Laarmann, C. Lechner, N. Ekanayake, *Extraction of the Longitudinal Profile of the Transverse Emittance From Single-Shot RF Deflector Measurements at sFLASH*,
Proc. 38th International Free-Electron Laser Conference, Santa Fe, NM, USA (2017)

J. Bödewadt, R. Assmann, M. M. Kazemi, C. Lechner, **L. L. Lazzarino**, T. Plath, J. Rossbach, *Determination of the Slice Energy Spread of Ultra-Relativistic Electron Beams by Scanning Seeded Coherent Undulator Radiation*,
Proc. 38th International Free-Electron Laser Conference, Santa Fe, NM, USA (2017)

V. Grattoni, R. Assmann, J. Bödewadt, I. Hartl, T. Laarmann, C. Lechner, M. M. Kazemi, A. Przystawik, S. Khan, N. M. Lockmann, T. Plath, A. Azima, M. Drescher, W. C. A. Hillert, **L. L. Lazzarino**, V. Miltchev, J. Rossbach, *Status of the Seeding Development at sFLASH*,
Proc. 38th International Free-Electron Laser Conference, Santa Fe, NM, USA (2017)

C. Lechner, A. Azima, M. Drescher, **L. L. Lazzarino**, Th. Maltezopoulos, V. Miltchev, T. Plath, J. Rönsch-Schulenburg, J. Rossbach, K. E. Hacker, S. Khan, R. Molo, S. Ackermann, J. Bödewadt, G. Brenner, M. Dohlus, N. Ekanayake, T. Golz, T. Laarmann, T. Limberg, E. Schneidmiller, N. Stojanovic, M. Yurkov, *Suppression of FEL Lasing by a Seeded Microbunching Instability*,
Proc. 37th International Free-Electron Laser Conference, Daejeon, Korea (2015)

K. Hacker, S. Khan, R. Molo, S. Ackermann, R. Assmann, J. Bödewadt, N. Ekanayake, B. Faatz, I. Hartl, R. Ivanov, T. Laarmann, J. Müller, H. Schlarb, P. Amstutz, A. Azima, M. Drescher, **L. L. Lazzarino**, C. Lechner, T. Maltezopoulos, T. Plath, J. Rossbach, *First Lasing of an HGHG Seeded FEL at FLASH*,
Proc. 37th International Free-Electron Laser Conference, Daejeon, Korea (2015)

J. Bödewadt, S. Ackermann, R. Assmann, N. Ekanayake, B. Faatz, G. Feng, I. Hartl, R. Ivanov, T. Laarmann, J. Müller, T. Tanikawa, Ph. Amstutz, A. Azima, M. Drescher, **L. L. Lazzarino**, C. Lechner, Th. Maltezopoulos, V. Miltchev, T. Plath, J. Rossbach, K. Hacker, S. Khan, R. Molo, *Recent Results from FEL Seeding at FLASH*,
Proc. 6th International Particle Accelerator Conference, Richmond, VA, USA (2015)

C. Lechner, A. Azima, M. Drescher, **L.L. Lazzarino**, Th. Maltezopoulos, V. Miltchev, T. Plath, J. Rönsch-Schulenburg, J. Rossbach, K. E. Hacker, S. Khan, R. Molo, S. Ackermann, J. Bödewadt, G. Brenner, M. Dohlus, N. Ekanayake, T. Golz, E. Hass, K. Honkavaara, T. Laarmann, T. Limberg, E. Schneidmiller, N. Stojanovic, M. Yurkov, *Demonstration of SASE Suppression Through a Seeded Microbunching Instability*,
Proc. 36th International Free-Electron Laser Conference, Basel, Switzerland (2014)

C. Lechner, A. Azima, M. Drescher, **L. L. Lazzarino**, Th. Maltezopoulos, V. Miltchev, T. Plath, J. Rönsch-Schulenburg, J. Rossbach, M. Wieland, K. E. Hacker, S. Khan, R. Molo, S. Ackermann, J. Bödewadt, H. Dachraoui, N. Ekanayake, B. Faatz, M. Felber, K. Honkavaara, T. Laarmann, J. Müller, H. Schlarb, S. Schreiber, S. Schulz, P. Salen, P. van der Meulen, G. Angelova, *Measurements of the Timing Stability at the FLASH1 Seeding Experiment*,
Proc. 36th International Free-Electron Laser Conference, Basel, Switzerland (2014)

T. Plath, **L. L. Lazzarino**, K. E. Hacker, *Conceptual Study of Self-seeding Scheme at FLASH2*,
Proc. 36th International Free-Electron Laser Conference, Basel, Switzerland (2014)

Abstract

In the course of the present experimental PhD work the first extreme ultraviolet (XUV) and soft x-ray pulse shaper relying on reflective optics has been developed. Its use will allow arbitrary control on the time-frequency spectrum of femtosecond pulses generated by seeded free-electron lasers (FEL) and high-harmonic generation (HHG) sources.
The device is based on the geometry of a 4f grating compressor. It has been applied to shorter wavelengths through the use of grazing incidence optics operated under ultra-high vacuum conditions. The design blaze angle and line density of the gratings allow the manipulation of all the different harmonics typical of high-gain harmonic generation (HGHG) and echo-enabled harmonic generation (EEHG) FELs, as well as of HHG sources, without the need of realignment of the instrument and even simultaneously in multicolor experiments.
Furthermore, the diagnostics necessary for commissioning of the pulse shaper have been realized, including an UV-IR cross-correlator for initial studies using 266 nm femtosecond pulses. HGHG seeding at FLASH and temporal characterization of the amplified XUV and soft x-rays by means of THz streaking has been achieved with important contributions by the author of this thesis. These longitudinally fully coherent FEL pulses are well-suited for future shaping applications.
A successful proof-of-principle pulse shaping experiment using 266 nm light has been performed, demonstrating spectral phase-control on femtosecond UV pulses.

Zusammenfassung

Im Zuge der vorliegenden experimentellen Doktorarbeit wurde der erste Pulsformer für extrem ultraviolette (XUV) und weiche Röntgenstrahlen entwickelt, der ausschließlich auf reflektierende Optik setzt. Seine Nutzung wird die beliebige Steuerung des Zeit-Frequenz-Spektrums der Femtosekundenpulse ermöglichen, die von *seeded* Freie-Elektronen-Lasern (FEL) und Hohe-Harmonischen Quellen (*high harmonic generation*, HHG) generiert werden.
Das Gerät basiert auf der Geometrie eines 4f Gitterkompressors. Der Einsatz für kürzere Wellenlängen wird durch die Verwendung von Optiken unter streifendem Einfall im Ultrahochvakuum ermöglicht. Die Blazewinkel und Liniendichte der Gitter wurden so ausgewählt, dass die Manipulation aller verschiedenen Harmonischen für *high-gain harmonic generation* (HGHG) und *echo-enabled harmonic generation* (EEHG) FELs sowie für HHG Quellen ermöglicht wird, ohne eine Neujustage des Instruments zu erfordern, und erlaubt sogar die gleichzeitige Nutzung mehrerer Harmonischer in Mehrfarben-Experimenten. Ferner wurden Diagnosegeräte entworfen, die für die Inbetriebnahme des Pulsformers nötig sind, inklusive eines UV-IR Cross-Korrelators für die ersten Versuchen mit 266 nm Femtosekundenpulsen.
HGHG Seeding bei FLASH und die zeitliche Charakterisierung der verstärkten XUV- und weichen Röntgenstrahlen mittels THz *Streaking* wurde mit wichtigen Beiträgen des Autors dieser Doktorarbeit erreicht. Diese longitudinal vollständig kohärenten FEL-Impulse sind für zukünftige Experimente mit geformten Pulsen gut geeignet.
Ein Nachweis der Funktionalität des Pulsformers wurde unter Nutzung von 266 nm Licht erfolgreich erbracht, indem die spektrale Phasensteuerung an Femtosekunden-UV-Pulsen demonstriertet wurde.

Introduction

In the last decade a new window of opportunities has opened up using intense **f**ree-**e**lectron **l**aser (**FEL**) pulses in the XUV and soft x-ray regime for photon science applications. Pioneering work has been done at FELs like FLASH at DESY in Hamburg and FERMI at Electra in Trieste. Both have been recently expanded with a second FEL line, due to the high demand of their photon pulses for experiments.
The implementation of so-called seeding schemes at these facilities, which allows for the generation of fully coherent photon pulses, paved the way for applying quantum control methodologies at FELs (see [1] and references therein). First experiments have been conducted at FERMI, tuning the machine parameters in order to tailor the photon pulse characteristics [2–4]. Further research and development of photon pulse shaping capabilities at FELs would enable current experimental techniques to be transferred from the optical spectral range (IR, visible and UV) to the short-wavelength limit, e.g. four-wave mixing [5].
The PhD project pursued in the present work has been focused on three main objectives:

1. *Feasibility study of an **X**UV and soft **x**-ray **p**ulse **s**haper (**XXPS**) relying on grazing incidence optics within the limits of current technology.*

While the use of photon pulse shapers is nowadays widespread for optical wavelengths, applying this technology to shorter wavelengths presents several challenges. The typical shaper geometry is that of a zero-dispersion compressor comprising of a symmetric arrangement of two gratings and focusing optics depicted in Fig. 0.1. Due to the shorter wavelength, requirements on positioning accuracy and surface quality of the optics are much tighter. In addition, to achieve a sufficient resolution the dispersion section after the diffraction gratings needs to be lengthened and the size of the optical elements on the shaping (phase) mask needs to be reduced by a large factor. The choice in optical elements is greatly reduced, with the use

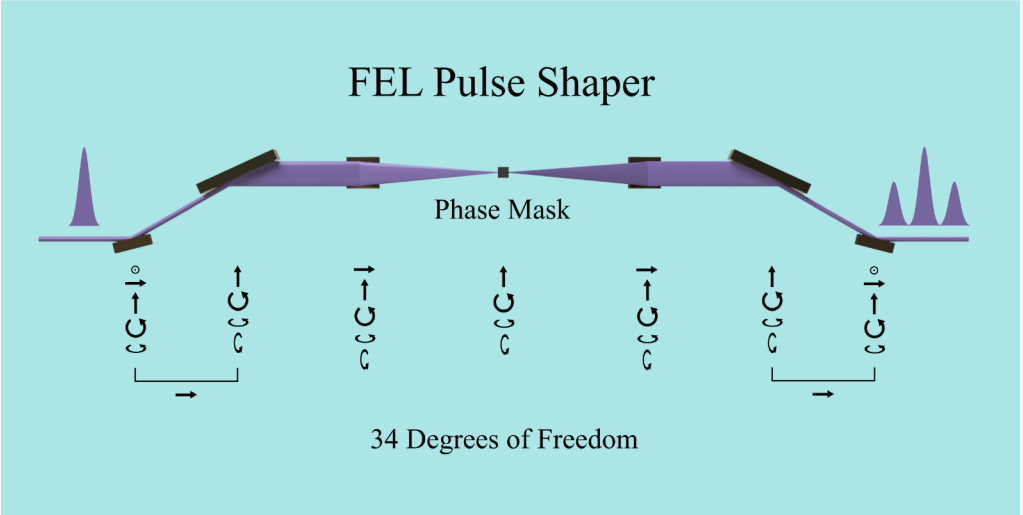

*Figure 0.1: View of the optical elements of the **X**UV and soft **x**-ray **p**ulse **s**haper (**XXPS**) designed by the author. The motorized degrees of freedom indicate the mechanical complexity of the device.*

of lenses being excluded due to the lack of transparent materials in the XUV and soft x-ray regime and reflective optics showing high reflectivity only at grazing incidence. The first stage of the project consisted in determining if available technology is sufficient to develop a pulse shaper overcoming these limits.

2. *Designing of the XXPS apparatus.*

The expected performances of the device needed to be sufficient for the envisioned shaping capabilities, with a particular focus on dispersion, focus size in the Fourier plane (more on the topic in Chapter 2) and overall transmission. The higher the spectral resolution in the Fourier plane the more sophisticated electromagnetic waveforms can be synthesized. The shaper needed to be compact enough to fit into the predisposed experimental hutch, with the flexibility to greatly increase the dispersion length of the pulse shaper with minimal changes, in case of experiments requiring higher resolution and taking place at other FEL facilities.

3. *Shaped pulse diagnostic development and commissioning strategy.*

FEL beam time is a scarce and expensive commodity. The commissioning of a novel device, including new custom-designed optical elements, typically requires a considerable amount of time. Therefore the need to devise

a commissioning strategy requiring as little as possible use of intense XUV and soft x-ray sources, that favors instead the use of conventional fs lasers. As will be explained in detail in Chapter 3 a smart grating design allowed use of subharmonics of the seeded XUV radiation (off-line), i.e. the optical 266 nm seed laser itself, without changing the overall alignment. It goes without saying that appropriate diagnostic tools had to be developed as well.

Within the present PhD work it is described how these three objectives have been achieved, and the results are discussed. In chapters 1 and 2, introductions to FELs and pulse shaping in general are given, respectively. In Chapter 3, the design of the XXPS is described, in both its anticipated XUV (15 nm-40 nm) and soft x-ray (4 nm-15 nm) implementation, together with the diagnostics developed for its commissioning. The expected performances are discussed in detail. Finally, in Chapter 4 the results of the first proof-of-principle pulse shaping experiment using UV laser light are highlighted.

Chapter 1

Seeding the Free-Electron Laser FLASH

Free-**e**lectron **l**asers (**FEL**s) are currently the main source of high-peak-power (GW) femtosecond laser pulses in the e**x**treme **u**ltra**v**iolet (**XUV**, 10-40 nm) and soft x-ray (1-10 nm) wavelength range. They are particle accelerators which generate radiation starting from ultrarelativistic electron bunches. This chapter begins with a short introduction to the basics of FEL physics (Section 1.1). Sections 1.1.1, 1.1.2 and 1.1.3 closely follow the the book "Ultraviolet and Soft X-Ray Free-Electron Lasers" by Schmüser, Dohlus and Rossbach [6], where in-depth discussions of the presented topics can be found with detailed mathematical derivations of all described effects. Seeding techniques allow generation of longitudinally fully coherent pulses[1]. Because this is a prerequisite for any photon pulse shaping device and its application, the main characteristics of those schemes are given in Section 1.2. In particular the seeded photon beam parameters and performance are compared to the **s**elf-**a**mplified **s**pontaneous **e**mission (**SASE**) scheme, used by most FELs in the world.
Research and development of **s**eeding at **FLASH** (in the course of this thesis called **sFLASH**) is described in Section 1.3. It makes use of part of the FLASH accelerator at DESY in Hamburg (Germany), which since opening in 2005 is the first XUV and soft x-ray FEL available to the photon science user community for experiments.

[1]The longitudinal coherence of a pulsed light source is determined by the degree of phase correlation along the pulse. A light pulse is said to be longitudinally coherent if there is a strong degree of phase correlation along the whole pulse, as shown e.g. by strong interference pattern when different sections of the pulse are overlapped through a split and delay unit. A more exhaustive discussion of the topic can be found in Section 1.2.3.

Key components for the reliable operation of FELs and their control are electron and photon diagnostics. The most important devices, and how they help in tailoring the ultraviolet seed laser, relativistic electron bunches and FEL radiation, are covered in Section 1.4.
The chapter ends with a short summary of the sFLASH R&D activities, in which the author played an active role between 2014 and 2018 (Section 1.5).
Note that in Accelerator Physics, the coordinate system is usually oriented with the z-axis along the electron beam direction, the y-axis pointing upwards and the x-axis horizontally according to the right-hand rule. Such convention is followed in the totality of this work.

1.1 FEL Physics and Seeding Schemes

An FEL consists of two main components: a particle accelerator and an undulator (or sometimes multiple). The particle accelerator accelerates electrons up to ultra-relativistic speeds. Electrons are used because of their ease of production (compared to positrons) and low mass, because the instantaneous power emission of a charged particle on a circular trajectory is:

$$P = \frac{cq^2\gamma^4}{6\pi\epsilon_0 R^2} \tag{1.1}$$

where c is the speed of light, q is the particle's charge, γ is its Lorentz factor, ϵ_0 is the permittivity of the vacuum and R is the radius of the trajectory [7].
Linear **ac**celerators (**linac**s) are usually preferred over storage rings due to their higher peak-current and lower energy spread[2]. The undulator is a straight section containing one or more periodically poled magnet structures, called undulator modules. While traversing these insertion devices the electron bunches emit synchrotron radiation pulses with a small energy bandwidth.

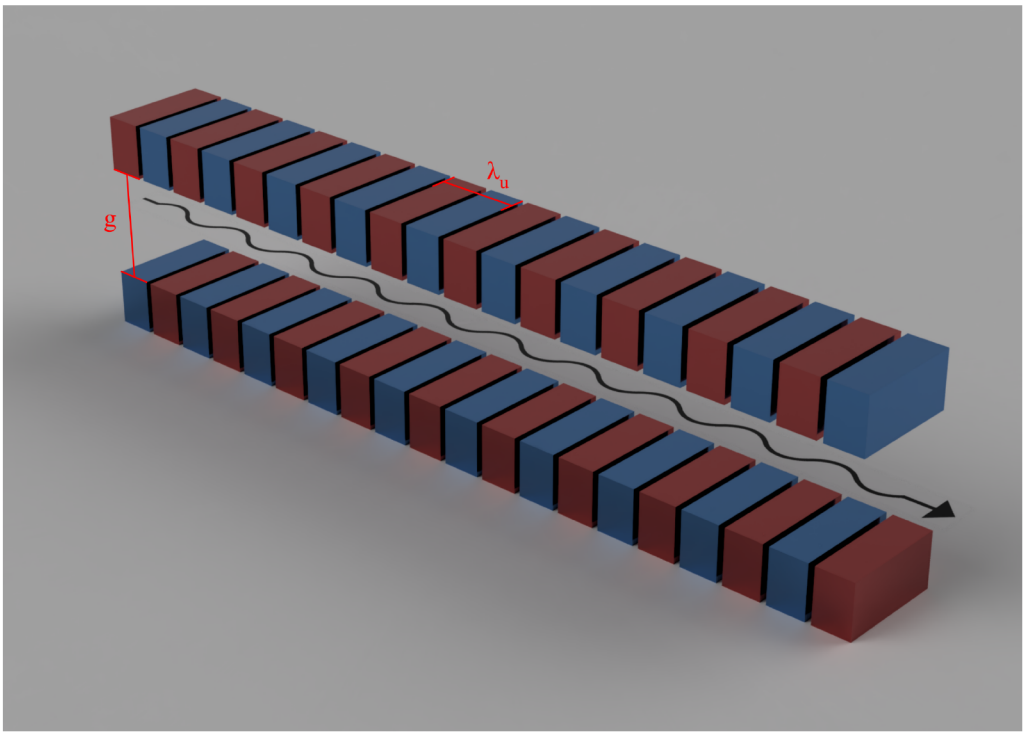

Figure 1.1: Basic representation of an undulator. It is made of a series of standardly short dipoles with alternating polarity.

1.1.1 Undulator radiation

An undulator module is a magnet comprised of a series of dipoles. By far the most widely used undulator variant is the planar undulator, where all the dipoles are parallel with alternating polarity (Fig. 1.1). All FLASH undulator modules, including sFLASH modules, are planar. The distance between a dipole and the next one with the same polarity is called the undulator period λ_u. The undulator gap g is the distance between the poles in the dipoles, and in most undulators it is constant along the magnet (tapered undulators are becoming popular as means of increasing the amount of energy extracted from the electron beam, more on the topic in Section 1.1.3). The gap can be tuned in variable-gap undulators, changing the strength of the magnetic field in the undulator and therefore the wavelength of the radiation generated.
The electrons in a planar undulator travel in a sinusoidal path. Due to the

[2]The energy spread of an electron bunch is the rms width of the electron energy distribution. How the energy spread influences FEL performance is covered in Section 1.1.3.

curved trajectory they emit synchrotron light. This radiation is emitted into a cone with a semi-angle of $1/(2\gamma)$, with its axis centered on the instantaneous electron trajectory [7]. Due to the periodicity of the electron motion and due to the small amplitude of their sinusoidal path, strong interference phenomena occur, with constructive interference of emitted photons in a band around the resonant wavelength, given by:

$$\lambda_{rad} = \frac{\lambda_u}{2\gamma^2}\left(1 + \frac{K_u^2}{2}\right) \tag{1.2}$$

where λ_u is the undulator period length, γ is the relativistic Lorentz factor and $K_u = \frac{\lambda_u e B_0}{2\pi m_e c}$, where B_0 is the on-axis peak magnetic field, e and m_e are respectively the electron charge and mass, and c is the speed of light. Constructive interference also happens for the harmonics of the resonant wavelength. In an undulator the amplitude of the sinusoidal motion is small (compared to what happens in a wiggler, which is an insertion device with the same magnetic structure of an undulator but stronger dipoles and larger period). Thus, the photons are emitted in a small, only slightly elliptical cone along the z-axis in the forward direction. The electric field of the emitted radiation is parallel to the sinusoid plane, i.e. the radiation emitted is linearly polarized along the plane of oscillation (all the modules currently in operation at FLASH are such conventional planar undulators, albeit undulators designed to generate circularly polarized radiation do exist [8]). The bandwidth of the undulator radiation, centered around the resonant wavelength and with an almost Gaussian distribution, has its fwhm given by:

$$\Delta\omega = \frac{\omega_{rad}}{N_u} \tag{1.3}$$

where ω_{rad} is the angular frequency of the resonant wavelength and N_u is the number of periods in the undulator.

1.1.2 Energy exchange between electrons and radiation

Let's now consider the effect of radiation on the electrons present in the undulator, when the radiation propagates along the axis of the electron sinusoidal motion with the electric field in the plane of the electron motion. The power exchange between electrons and electric field E is given by the interaction with the Lorentz Force as:

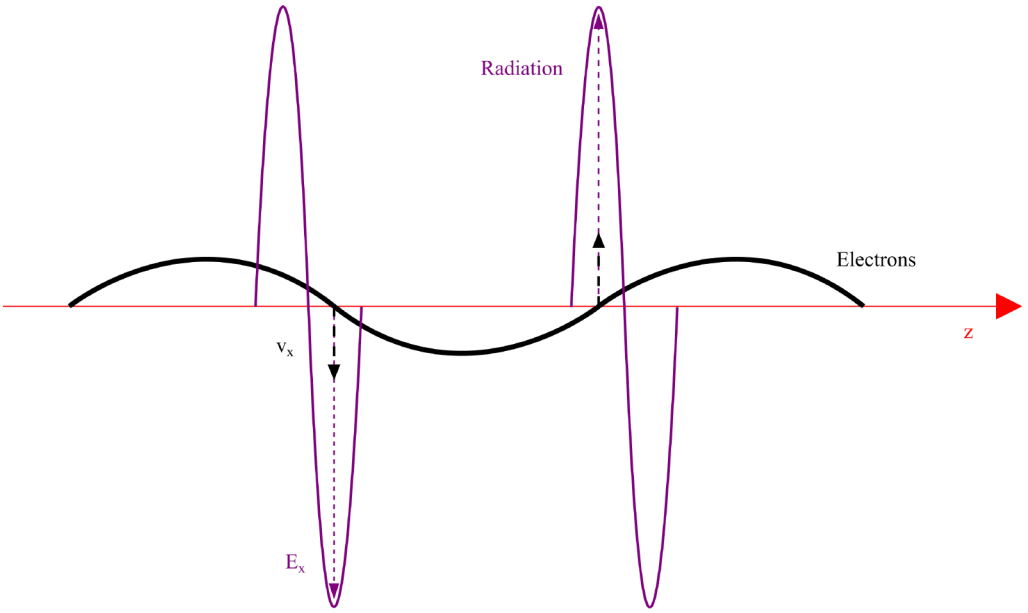

Figure 1.2: Simplified representation of the electron radiation coupling in an undulator. Coupling takes place in the electron oscillation plane, between the electrons and the light electric field.

$$P = \vec{v} \cdot \vec{F} = v_x e E \tag{1.4}$$

where $\vec{F}$ is the Lorentz force, $\vec{v}$ is the electron velocity and e is the electron charge (see Fig. 1.2). The electric field of the emitted radiation interacts with the electrons in the bunch, leading to energy exchange between the two. The energy transfer from electrons to radiation is maximum when the relative phase slippage of the electron oscillation and radiation electric field oscillation is constant, and the electron has maximum transverse velocity when the electric field peaks. The first condition is satisfied when the wavelength of the radiation is the undulator resonant wavelength or, to a lesser extent, within the undulator bandwidth. It follows that this process of stimulated radiation emission, which takes the name of FEL process, can be started by the undulator's spontaneous radiation.

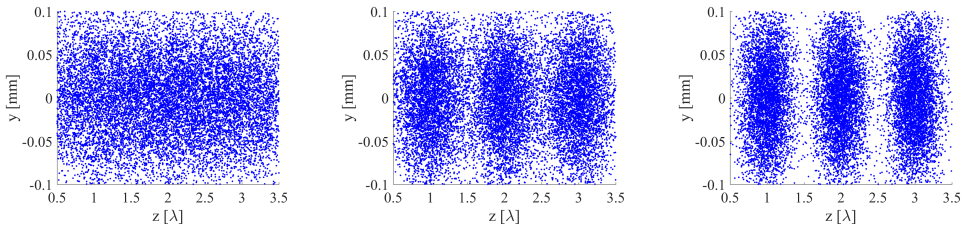

(a) (b) (c)

Figure 1.3: The microbunching process. Due to the energy exchange with the radiation, electrons in an undulator change their effective longitudinal velocity and slowly accumulate within small slices. Such slices are located periodically near the points of maximum electron-radiation exchange. At the undulator entrance the electrons in the bunch are uniformly distributed (a). Slowly their density starts to modulate (b) until they reach the maximum density allowed by Coulomb repulsion (c).

1.1.3 Working principle of a SASE FEL

Conventional optical lasing schemes, e.g. resonance cavities, are not possible at short wavelength, where mirrors with high 90°-reflectivity are not available. Therefore single-pass FELs are used to generate XUV and soft x-rays. In single-pass FELs each light pulse is generated by a single electron bunch, passing through the undulator only once. The physical process responsible for the high laser peak power output typical of such devices is called microbunching. Electrons that have lost energy to the radiation travel on a sinusoid with higher amplitude compared to electrons that gained energy, due to their lower momentum and nearly-identical magnetic force because of their ultrarelativistic speed. A modulation of the electrons' longitudinal velocity follows, leading to modulation of the electron density in the bunch.
The electrons accumulate in tight slices with the periodicity of the undulator resonant wavelength. Thus, the radiation emitted by the electrons from different slices close to the resonant wavelength interferes constructively. Due to superradiance, the intensity of the radiation grows with the square of the number of electrons in these slices or 'microbunches' (Fig. 1.3). The mathematical derivation of this process can be found in [6].
The microbunching process is at the root of the three power growth regimes in a single-pass FEL, which are shown in Fig. 1.4. They are called the lethargy regime, the exponential growth regime and the saturation regime. At the undulator entrance the FEL is in lethargy regime. The densely

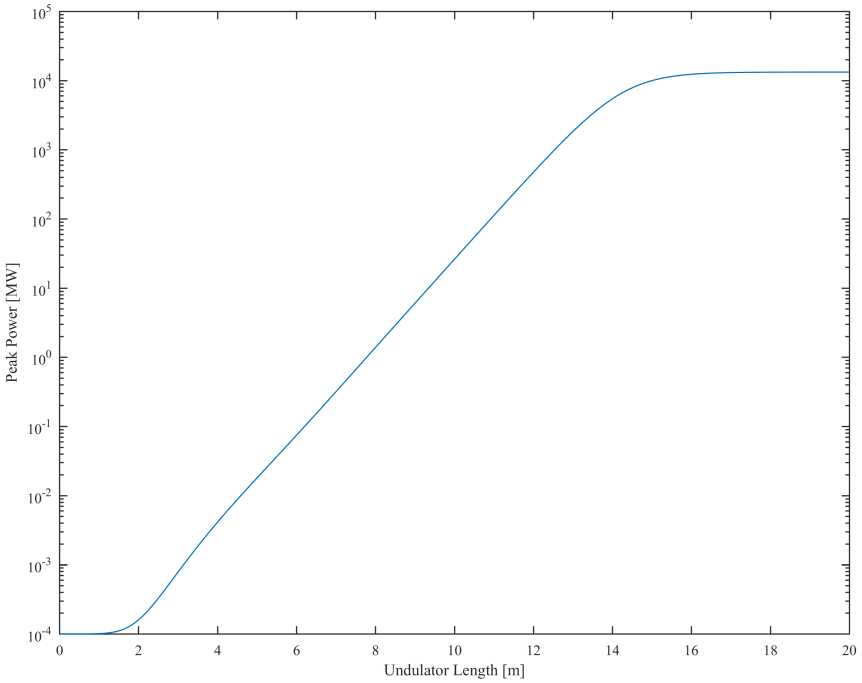

Figure 1.4: The FEL power gain curve. In a SASE single-pass FEL at the beginning of the undulator the microbunches are still not formed, therefore the FEL power growth is slow. This phase is called the lethargy regime. When the microbunches are sufficiently developed, the power growth quickly becomes exponential. When the microbunches approach their maximum development, the power growth slows and quickly reaches a maximum saturation level.

packed slices are slowly starting to form, and the power increase is approximately linear. When the slices are sufficiently dense and the electric field of the radiation is sufficiently intense the power growth rapidly becomes exponential. Once the electrons in the slices are packed as closely as possible due to Coulomb repulsion the power growth reaches saturation. In this regime further energy losses bring the electrons out of phase with the electromagnetic field, therefore electrons gain energy back from the radiation. Such a limit can be overcome with the addition of afterburners, i.e. tapered undulators whose magnetic field progressively decreases in order to keep microbunches and radiation in phase, thus increasing the amount of energy that can be extracted from the ultra-relativistic electron bunches [9].

To reach saturation typically several meters of undulator are needed, and the shorter the wavelength the longer the undulator must be (undulators for hard x-ray generation in the new European XFEL are up to 256 m long [10]). The use of afterburners further increases the undulator length.
Commonly, undulator lengths are expressed in terms of the gain length L_g, i.e. the length where the power grows by a factor e in the exponential growth regime. It can be calculated approximately analytically, using 1D theory, though 3D simulations are needed for an accurate prediction. The bandwidth rms of an FEL holds:

$$\frac{\Delta\lambda}{\lambda} \approx 2\rho \tag{1.5}$$

The Pierce parameter ρ is a dimensionless quantity connected to the maximum tolerable beam energy spread: as a rule of thumb, a relative energy spread greater than the Pierce parameter leads to a significant gain length increase and smaller saturation power. It is defined as:

$$\rho = \frac{1}{4\pi}(\pi g_0)^{\frac{1}{3}} \tag{1.6}$$

The gain parameter g_0 is a dimensionless parameter defined as:

$$g_0 = 4\pi\frac{J}{I_0}(\frac{(\lambda_u K_u)^2}{\gamma^3})(\lambda_u K_u f_b)^2 \tag{1.7}$$

where J is the current density of the electron beam, $I_0 = 17045.09A$ is the Alfvèn current and f_b is the Bessel factor, defined in a planar undulator as:

$$f_b = J_0(\xi) - J_1(\xi) \tag{1.8}$$

Here J_n are the cylindrical Bessel functions, while ξ is defined as:

$$\xi = \frac{1}{2}K_u^2(1 + K_u^2)^{-1} \tag{1.9}$$

Self-**a**mplified **s**pontaneous **e**mission (**SASE**) is a well-established mode of operation that has been used to operate the first single-pass FELs. The electron bunch generated by a linac is directly fed into the undulator. The electrons spontaneously start emitting synchrotron radiation, that slowly begins to create microbunches in a stochastic fashion. Due to the low intensity the lethargy regime is several gain lengths long. In SASE FELs

saturation is typically reached in about 18-20 L_g [6]. The bandwidth of each pulse covers usually most of the FEL bandwidth, with shot-to-shot variations.
The pulses generated by SASE FELs have several limitations. Their longitudinal coherence is poor and the spectrum of each single SASE shot presents many spikes at different wavelengths. The peak positions and amplitude vary from shot to shot, along with the power output.

1.1.4 Seeding schemes

In order to improve FEL pulse characteristics, an external laser can be used to initiate the microbunching process. Important laser beam attributes, like longitudinal (temporal) coherence, photon and pulse energy stability and a Gaussian spectrum, can be transferred from the seed laser to the electron bunch modulation and finally to the FEL pulses. In general, two approaches can be distinguished. The electron beam can be injected into the FEL undulator overlapped with a seed laser beam on the FEL resonance. This configuration, in which the FEL acts as an amplifier of the input signal, is called direct seeding. Alternatively, the seed can interact with the electrons, starting the microbunching process in a controlled way before the electrons enter the final FEL undulator. The first method is used in direct seeding and self-seeding schemes, while the second one is used in **h**igh-**g**ain **h**armonic **g**eneration (**HGHG**) [11, 12] and **e**cho-**e**nabled **h**armonic **g**eneration (**EEHG**) [13, 14].
When a seeding scheme is used, the SASE process is taking place in parts of the electron beam that are not seeded. Seeding schemes require shorter undulators compared to SASE, due to the fact that the lethargy regime is shorter. It follows that the undulator length can be optimized in such a way that the resulting seeded FEL power approaches saturation while the SASE one is multiple orders of magnitude weaker.
At sFLASH currently HGHG is being studied, while EEHG is under development. Both of these schemes are briefly described in the following sections.

1.1.5 High-gain harmonic generation: single stage and cascaded

Compared to direct seeding the HGHG scheme requires additional hardware in the accelerator: a second undulator and a magnetic chicane are added between the linac and the main undulator (see Fig. 1.5).
The first undulator entered by the electron bunch at the linac exit is called

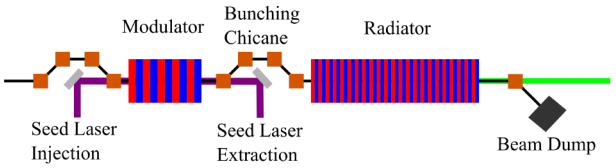

Figure 1.5: Sketch of the HGHG implementation. The seed laser is overlapped with the electron beam in a short undulator called a modulator, which is resonant with the seed laser wavelength. The interaction of the beam with the seed laser produces a periodic energy modulation. Such an energy modulation is then converted into a charge density modulation by a dispersive magnetic chicane. Subsequently the electron beam enters the main undulator, called a radiator. The radiator can be tuned to high harmonics of the seed laser wavelength, as long as sufficient microbunching is present to start the FEL lasing process.

a modulator. It is a relatively short undulator (5 periods at sFLASH) resonant with the seed laser wavelength. The seed laser is a high-power, pulsed femtosecond laser, often a solid-state Ti:Sa. Its pulses overlap the electron bunch in the modulator and induce a longitudinally (and therefore temporally) coherent energy modulation (see Fig. 1.6 (a) and (b)). The laser pulses are much shorter than the electron bunch, to make sure that the seed pulse always hits the useful part of the electron bunch in spite of their timing jitter, that is on the order of 30 to 50 fs at sFLASH, depending on the synchronization method used (see Section 1.3.1). In alternative, a seed pulse much longer than the electron beam could be used to achieve the same result. A shorter laser pulse is usually preferred in order to reduce the required seed-laser pulse energy. Due to the short length of the modulator, the amount of microbunching introduced in the modulator is negligible.
The induced average energy modulation has a period equal to the laser wavelength. Behind the modulator the electron bunch passes through a magnetic chicane (also called bunching chicane), comprised of 4 dipole magnets. In the chicane higher energy electrons, whose trajectory is bent less by the dipoles, travel a shorter path than lower energy electrons. It follows that, with appropriately tuned dipole field strengths, the electron current distribution in the bunch can be changed dramatically (see Fig. 1.6 (c) and (d)). The induced charge density modulation has the same periodicity of the kinetic energy modulation, and maintains its longitudinal coherence. The most important aspect for HGHG is that the Fourier transform of this current profile reveals its rich harmonic content. The current modulation at each harmonic can be expressed in terms of the bunching factor:

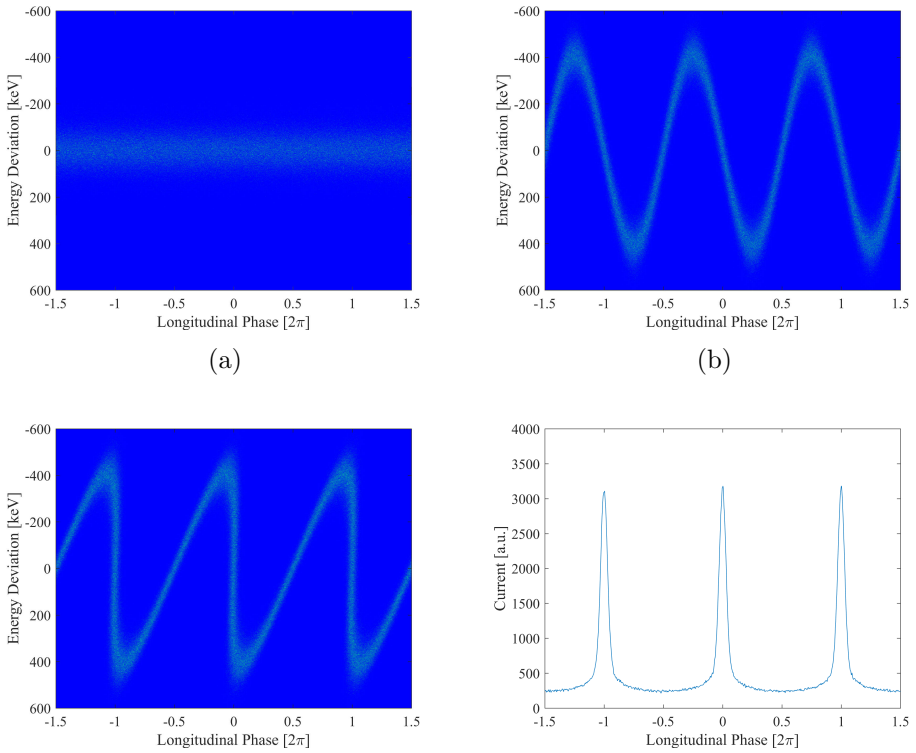

Figure 1.6: Evolution of the longitudinal phase-space distribution of the electron bunch in the HGHG scheme. A section of the electron bunch before (a) and after (b) the modulator and after the bunching chicane (c) are compared. The resulting charge distribution after the chicane is also shown (d). Pictures courtesy of Tim Plath.

$$b_n = J_n\left(nkR_{56}\frac{\Delta\gamma}{\gamma}\right)\exp\left(-\frac{1}{2}[nkR_{56}\frac{\sigma_\gamma}{\gamma}]\right) \tag{1.10}$$

where n is the harmonic number, k is the wavenumber of the seed laser, R_{56} is the corresponding element of the chicane transfer matrix that correlates the energy difference of an electron from the beam mean energy to its position change after the chicane in the longitudinal phase-space, $\Delta\gamma$ is the amplitude of the energy modulation introduced in the modulator and σ_γ is the electron energy spread, both expressed in terms of the Lorentz factor γ. Uniformly distributed electrons give $b = 0$, while $b \approx 0.6$ at saturation. Bunching factors for typical sFLASH parameters are shown in Figure 1.7.

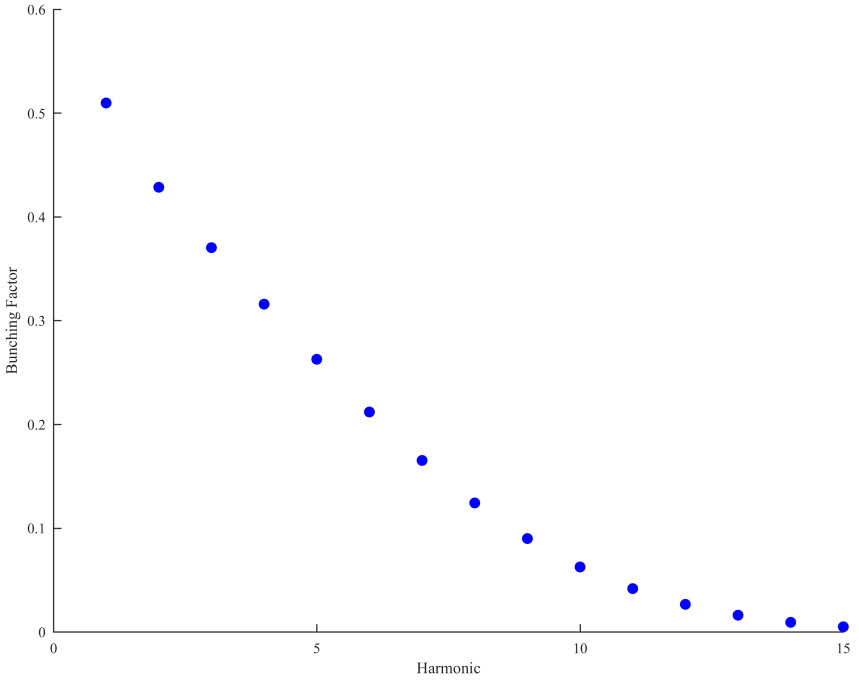

Figure 1.7: Bunching factor at the radiator entrance for typical sFLASH parameters.

After the chicane the electron bunch enters the main FEL undulator, called a radiator. If the radiator is tuned to a harmonic of the seed laser wavelength, then the electron bunching at that particular harmonic will start the FEL power growth. The radiator is much longer than the modulator (300 periods at sFLASH), but it is still shorter than the SASE undulator (400 to 500 periods) that would be required with the same electron bunch characteristics, because of the already partially developed microbunches. The shorter length of the insertion device reduces space requirements for seeded FEL facilities, and keeps the SASE background low. At sFLASH it is typically about 1000 times lower than seeded power.
The highest harmonic at which the radiator can be operated is limited by certain constraints. As a rule of thumb, in order to generate sufficient bunching at the h-th harmonic the amplitude of the energy modulation induced in the modulator needs to be approximately h times the initial electron energy spread. However, the energy spread induced by the modulation can severely spoil FEL performances. With state-of-the-art tech-

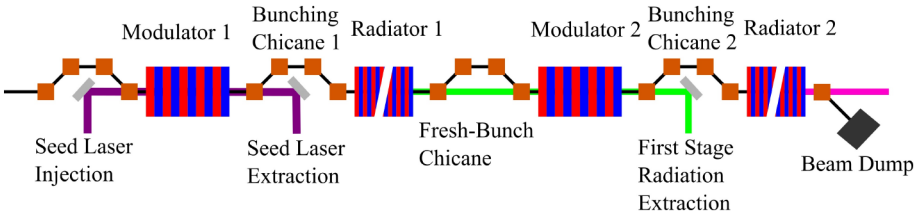

Figure 1.8: Sketch of a two stage cascaded HGHG FEL. The first HGHG stage generates laser pulses at a harmonic of the external seed laser, whose pulses are much shorter than the electron bunch. Then the electrons are sent through a magnetic chicane, in order to delay them with respect to the FEL light pulse. The radiation is overlapped in the second stage modulator with a "fresh" part of the electron bunch, with no bunching due to the previous stage. The downstream FEL radiator is then tuned to a harmonic of the upstream FEL, generating light of much shorter wavelength.

niques the highest harmonic that has been used in the XUV is the 13th [8]. Such physical limits, together with the current lack of high-repetition rate femtosecond lasers suitable as seeds below 230 nm [8], restricts the shortest wavelength reachable with a common HGHG scheme to about 20 nm.
To access lower wavelengths with the HGHG scheme, two HGHG FELs can be cascaded. The light pulses generated by the upstream FEL are used to seed the downstream FEL (see Fig. 1.8).
The first one operates as a conventional one-stage HGHG FEL: an external pulsed seed laser is used to induce the electron energy modulation, while the radiator is tuned to one of its harmonics as described above. The only difference compared to the single-stage scheme is the electron bunch length, which is much greater. At the exit of the first radiator the electron bunch enters a chicane, which delays it with respect to the FEL light. Both are then overlapped in a second modulator in such a way that the FEL pulse is interacting with a "fresh" part of the electron bunch, with no energy spread increase due to seeding in the previous stage. The microbunching introduced by SASE has been smeared out by the chicane. Finally the electron beam enters the second stage radiator, which is tuned to a harmonic of the first stage. With this scheme FEL operation up to the 100th harmonic of the external seed laser can be reached [15,16]. With a two-stage cascaded HGHG FEL it is possible to cover the water window, i.e. the wavelength range between the carbon K-edge absorption band at 4.4 nm and the oxygen K-edge band at 2.34 nm where the water is transparent. Due to this property the water window is of interest for studies in the fields of biology and organic chemistry at FELs. Two-stage cascaded HGHG FEL opera-

tion has been demonstrated at FERMI, with $h_1 = 6$ in the first stage while $h_2 = 10$ in the second stage[3] [16].
Though not experimentally shown yet, a cascaded HGHG FEL could in principle incorporate more than two stages to go even further down in wavelength. It can be calculated analytically that the following inequality must hold for the HGHG process to take place [17]:

$$h_{tot} \ll \sqrt{\frac{P_{m,1}}{P_{n,1}}} \tag{1.11}$$

Here h_{tot} is the harmonic of the seed laser generated at the output of the last stage, while $P_{m,1}$ and $P_{n,1}$ are respectively the seed power and the shot noise power in the first modulator, with the second being usually in the order of 100 W. Because the modulation process increases the energy spread there is an upper limit to the amount of seed power, and therefore to the harmonic that can be reached. This inequality can be regarded as an upper limit. More detailed 3D electron beam dynamics simulations must be run to pinpoint FEL performance parameters.

1.1.6 HGHG photon pulse properties

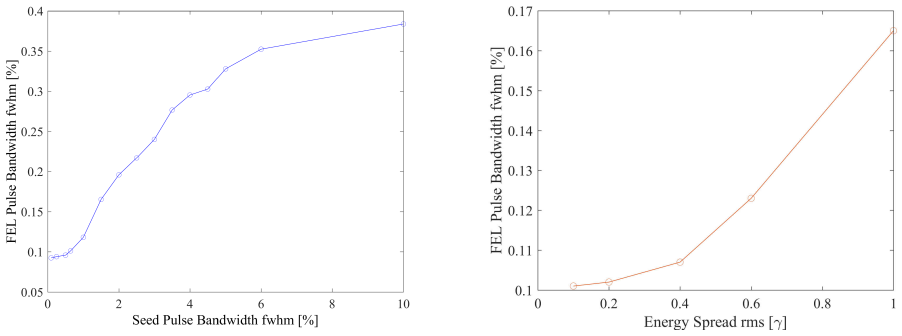

(a) (b)

Figure 1.9: HGHG FEL energy bandwidth, as a function of seed laser bandwidth (a) and initial energy spread (b), for standard sFLASH parameters, in particular 266 nm seed wavelength and radiator tuned to the 7th harmonic.

HGHG FELs generate longitudinally fully coherent pulses, with only small shot-to-shot variations in temporal profile and energy bandwidth.

[3] h_n is the resonant harmonic of the radiator with respect to the modulator in the n-th stage

Thus, they are ideally suited for pulse shaping, where coherence and constant properties of a pulse are of the utmost importance.
The time duration of the pulses generated by a HGHG FEL depends on the seed laser time duration and on the harmonic to which the radiator is resonant. The pulse time duration can be estimated with the equation:

$$\Delta t_{FEL} = \frac{\Delta t_{seed}}{\sqrt[3]{h}} \tag{1.12}$$

where Δt_{FEL} is the duration of the seeded FEL pulse, Δt_{seed} is the duration of the optical seed laser and h is the number of the harmonic at which the radiator is tuned. This prediction has been shown to be consistent with experimental data [4] and can be obtained as a fit of analytical predictions, but for an extra 7/6 factor [18].
The energy bandwidth of an HGHG FEL depends on the seed laser bandwidth and on the initial electron energy spread. An increase in the seed laser bandwidth translates to an increase of the FEL pulse bandwidth, as long as the spectrum of the seed laser remains within the modulator bandwidth. An increase in the energy spread also translates to a larger FEL pulse bandwidth, but at the cost of degraded FEL performances. There is no analytical way available for estimating this quantity with sufficient accuracy. The effects of initial energy spread or seed bandwidth variation at sFLASH have been simulated using the well-established FEL simulation code GENESIS 1.3 [19] and the results are shown in Fig. 1.9. Typical values at sFLASH are 135 keV for the energy spread and 0.64% for the seed laser bandwidth fwhm. In the simulations, one of the parameters was kept fixed while the other was varied.
It can be seen that an increase in seed laser bandwidth can considerably increase the resulting bandwidth of the FEL pulse. However changing the seed laser bandwidth beyond 6% has a rather small effect. Compared to this an increased electron energy spread affects the resulting bandwidth of the FEL pulse much less, keeping in mind that this goes hand-in-hand with an increase of the saturation length and degraded FEL performance.

1.1.7 Towards shorter wavelengths with EEHG

Echo-**e**nabled **h**armonic **g**eneration (**EEHG**) is a more advanced seeding scheme compared to the approaches described above, because of the increased complexity of the electron bunch manipulation involved [13]. Much shorter wavelengths are within reach of a single stage. In an EEHG FEL two modulators are present, each followed by a magnetic chicane as shown

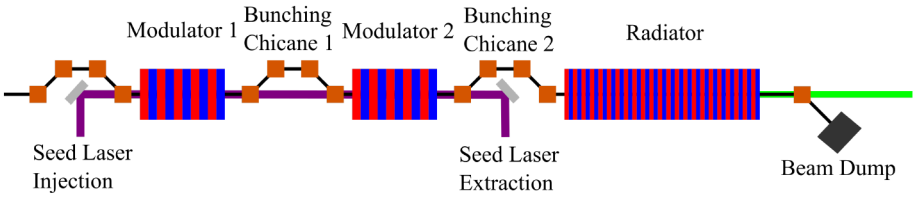

Figure 1.10: Sketch of the EEHG setup. While in HGHG FELs a single modulator and magnetic chicane are present, in EEHG two modulators are needed, each followed by a magnetic chicane.

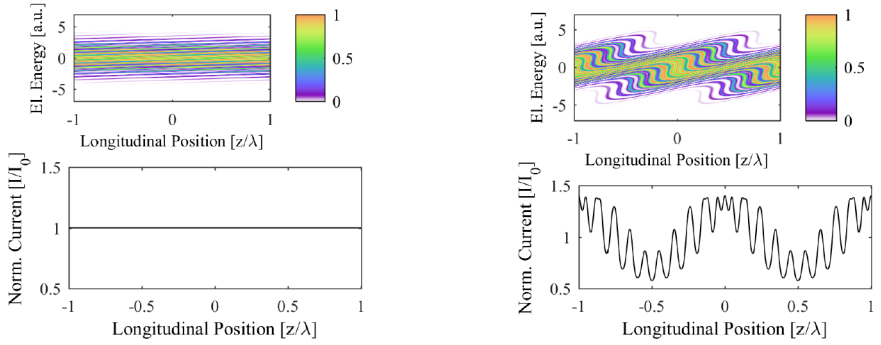

Figure 1.11: Bunching process in EEHG. The plots show the longitudinal phase-space distribution of the electrons in a small portion of the electron bunch. After the first bunching chicane, with R_{56} much greater then HGHG bunching chicanes, the electron bunch is over-sheared and energy bands are created (a). The second bunching chicane introduces a periodical current modulation (b), rich in harmonic content. In the top plots, the color-code indicates the particle density in arbitrary units. Pictures courtesy of Christoph Lechner.

in Fig. 1.10. Such an arrangement enables seeding at higher harmonics of the seed laser with a much shorter setup compared to cascaded HGHG FELs.

In the first modulator the electron bunch is modulated by a seed laser with wavelength λ_1. The following chicane is operated at a much higher R_{56} compared to a HGHG equivalent, inducing much higher dispersion. This results in the creation of separate energy bands in the electron bunch (see Fig. 1.11) by over-shearing the energy modulation.

In the second modulator the electron beam energy is modulated by a second

seed laser of wavelength λ_2, where λ_2 is usually a harmonic or subharmonic of λ_1 or even $\lambda_2 = \lambda_1$. The second pulse can be injected in the first bunching chicane, or even together with the first seed pulse if the two pulses are polarized orthogonally to each other and the electron wiggling planes of the modulators are similarly perpendicular. Such arrangement requires only a single seed laser injection beamline, and is realized at sFLASH. The dispersive strength of the second chicane is comparable to typical HGHG values, and it induces the electron bunch current modulation. Its magnetic field is tuned in order to maximize the electron bunching at the selected radiator harmonic. The described scheme induces a bunching factor $b_h \propto h^{-\frac{1}{3}}$, which is comparable to HGHG values for low harmonics of the seed lasers but much higher for the tenth harmonic and above. The EEHG scheme has been first demonstrated in the UV spectral range at the **N**ext **L**inear **C**ollider **T**est **A**ccelerator (**NLCTA**) at SLAC [20]. With seed wavelengths of $\lambda_1 = 800\,\text{nm}$ and $\lambda_2 = 2400\,\text{nm}$, seeding at the 15th harmonic of 2400 nm was achieved, i.e. at 160 nm. The viability of much higher harmonics is currently under study at the NLCTA, and bunching up to the 75th harmonic has been recently shown [21], although the small bunch current of the facility does not allow for the high-gain FEL process to start.

1.2 HGHG vs SASE Pulses: a Comparison

SASE and HGHG FEL pulses differ in many characteristics. The main differences are to be found in their spectrum, pulse energy and longitudinal coherence. Of particular interest for many applications is the achievable contrast between seeded pulse and SASE background in HGHG. These characteristics are discussed in some detail in the next subsections. When not otherwise specified, SASE data shown is from FLASH1, the worldwide first XUV and soft x-ray SASE FEL, available for user experiments since 2005. HGHG data is either from sFLASH or from FERMI, the first XUV and soft x-ray HGHG seeded FEL, that started FEL user operations in 2012.

1.2.1 Pulse spectrum

The SASE process is started from random emission of synchrotron radiation in the first undulator periods (shot noise). Such a process starts simultaneously everywhere along the bunch. In the undulator the emitted radiation travels on a straight line and therefore overtakes the electrons. Thus, while slipping forward through the electron bunch, the radiation interacts with

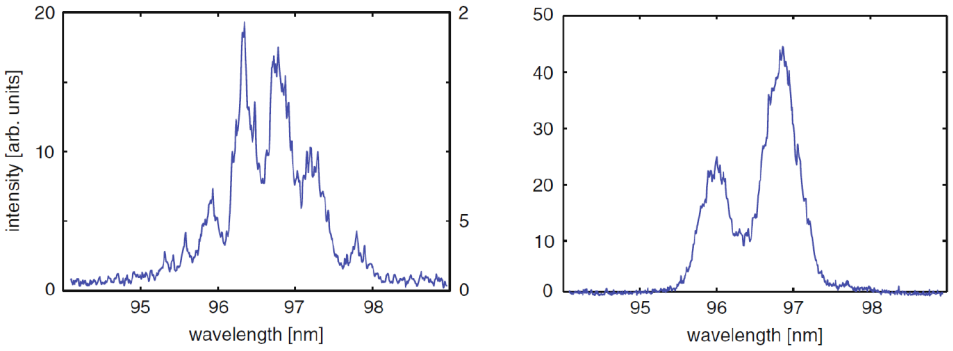

(a) (b)

Figure 1.12: SASE spectrum generated from a long (a) or short (b) electron bunch. Figure reprinted by permission from Springer Nature: [22].

different parts of the bunch. This phenomenon is called slippage. Due to this effect, the parts of the bunch that stochastically started the SASE process faster, condition the neighboring preceding electrons to radiate in phase at the same wavelength. This process creates the spikes typical to the SASE spectrum, each of them due to a different section of the bunch radiating coherently at a different wavelength. The distance the radiation slips forward over the gain length is called cooperation length. The average number of spikes in a single pulse depends on the ratio between the electron bunch length and cooperation length, and will be approximately equal to that ratio. Obviously shorter electron bunches exhibit less spikes in the spectrum as shown in Figure 1.12.

In HGHG FELs the lasing process is started from the bunching in the electron beam induced by the seed as discussed in Section 1.1.5. The bunching has inherited the longitudinal coherence of the seed laser, therefore all of the seeded parts of the electron beam radiate coherently (in phase) at the same wavelength. It follows that the spectrum of the FEL pulse shows an approximately Gaussian shape and is typically smaller than the FEL amplification bandwidth (see Fig. 1.13). Typically, the shot-to-shot variations of the HGHG spectra are negligible and given by the spectral stability of the optical seed.

Usually the SASE pulses bandwidth (which covers the full FEL amplification bandwidth) is on the order of 1-2%. The bandwidth of HGHG pulses can be extremely small (0.3‰ fwhm achieved at FERMI [16]), or much larger (bandwidths close to 0.6% fwhm measured at sFLASH).

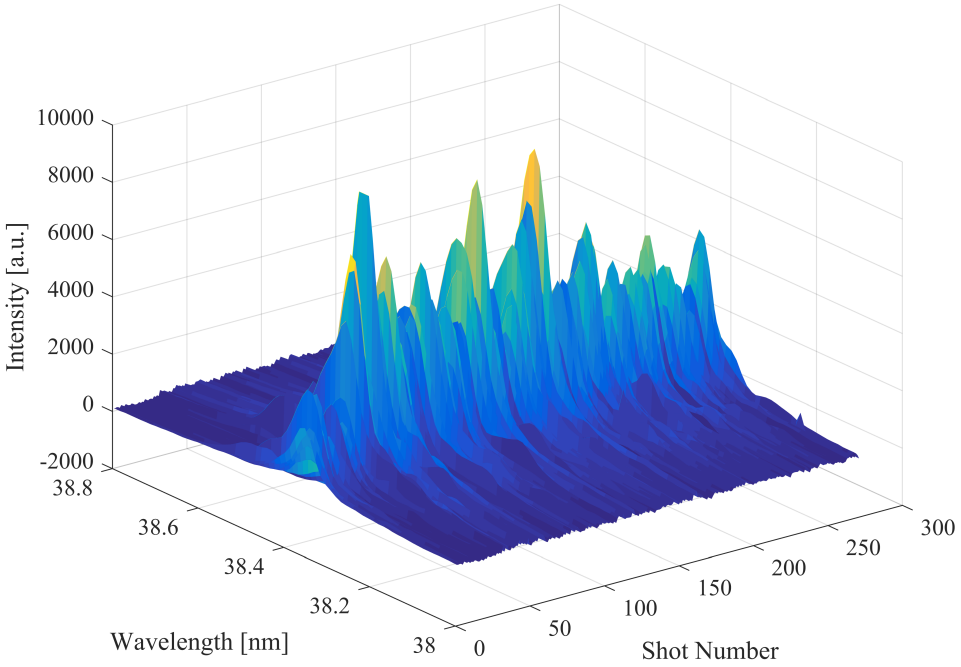

Figure 1.13: HGHG FEL spectrum at sFLASH. The spectrum of successive pulses is shown. The shot-to-shot spectral stability is very good, both in central wavelength and in spectral bandwidth. The FEL spectrum is approximately Gaussian. Picture courtesy of Tim Plath.

1.2.2 Pulse energy and contrast

The energy distribution of SASE pulses depends drastically on the undulator length. If the undulator is not long enough to reach saturation, shot-to-shot energy fluctuations are huge due to the variable duration of the lethargy regime. The resulting energy distribution follows a gamma distribution (as depicted in Fig. 1.14 (a)). However if the undulator is long enough that the FEL process reaches saturation for each electron bunch, then the energy jitter is smaller, and the energy distribution is approximately Gaussian, as can be seen in Fig. 1.14 (b) [23]. If the undulator length is such that only some of the pulses reach saturation, the energy distribution will be a weighted combination of the two.
Sometimes a monochromator is used at the exit of a SASE FEL to select a single wavelength for spectroscopic applications. A monochromator reduces the FEL pulse bandwidth and fixes its central value, at the expense of re-

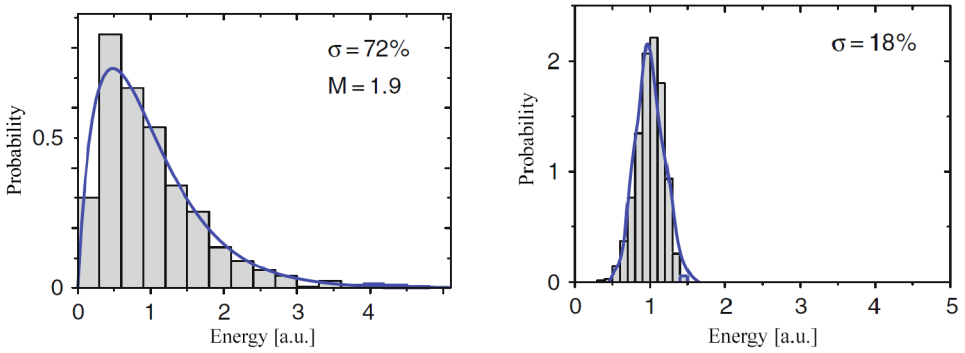

Figure 1.14: Energy distribution of SASE pulses in the exponential (a) and saturation (b) regimes. If the FEL process ends during the exponential regime the energy of SASE pulses shows huge fluctuations, due to the stochastic nature of the lethargy regime. The energy probability distribution at the exit of the undulator follows a gamma distribution. When the SASE process reaches saturation at every shot, power fluctuations are mitigated. The resulting power distribution is approximately Gaussian. Figure reprinted by permission from Springer Nature: [23].

duced pulse energy and 100 % energy fluctuations. This is shown in Figure 1.15. By restricting the bandwidth below the width of one SASE mode the pulses can be made fully longitudinally coherent (more on longitudinal coherence in Section 1.2.3).
The pulse energy in single-stage HGHG FELs is usually more stable than in saturated SASE FELs. Its distribution depends on the seed laser intensity fluctuations and timing jitter. In the radiator of HGHG FELs the SASE power growth takes place when the seeded part is just a small section of the electron beam, as it is usually the case. FELs optimized for HGHG operation nevertheless reaches signal-to-noise ratios in the order of 10^5 [24].

1.2.3 Transversal and longitudinal coherence

Full transversal and longitudinal coherence are mandatory requirements for pulse shaping experiments. In the theory of coherence, the **m**utual **c**oherence **f**unction (**MCF**) is used to describe the second order correlation of light sources [27, 28]. The MCF is defined as:

$$\Gamma(\boldsymbol{r}_1, \boldsymbol{r}_2, \tau) = \langle E(\boldsymbol{r}_1, t) \cdot E(\boldsymbol{r}_2, t+\tau) \rangle \tag{1.13}$$

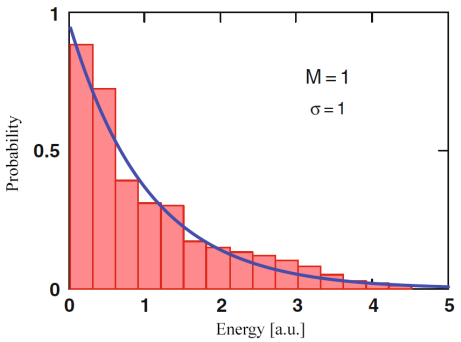

Figure 1.15: Energy distribution of a SASE FEL after a monochromator. A monochromator is an effective solution for limiting and fixing the bandwidth of SASE FELs. This result comes at expense of significant energy reduction and increase in the energy fluctuation, whose single shot energy distribution has $\sigma = 100$ %. Figure reprinted by permission from Springer Nature: [22].

Here $E(\boldsymbol{r}_1, t)$ and $E(\boldsymbol{r}_2, t+\tau)$ denote the complex electric field (see Eq. 2.1) at positions $\boldsymbol{r}_1$ and $\boldsymbol{r}_2$ separated by a time interval τ, while $\langle\rangle$ indicates that the value is averaged over the ensemble. The complex degree of coherence is defined as:

$$\gamma_{12}(\tau) = \Gamma(\boldsymbol{r}_1, \boldsymbol{r}_2, \tau)/I(\boldsymbol{r}_1)^{1/2} I(\boldsymbol{r}_2)^{1/2} \tag{1.14}$$

with $I(\boldsymbol{r}_1)$ and $I(\boldsymbol{r}_2)$ being the average intensities in $\boldsymbol{r}_1$ and $\boldsymbol{r}_2$. The direct measurement of the contrast of the fringes in a double-slit experiment returns the modulus of $\gamma_{12}(\tau)$.
In the lethargy regime at the beginning of the SASE process many $\mathrm{TEM}_{\mathrm{mn}}$ modes are present. However only the TEM_{00} mode has its maximum at the center of the undulator axis, where the electron density on average is highest. The better overlap with the electron beam greatly favors the TEM_{00} power growth in the exponential regime. As a result, it is by far the dominant mode in a saturated SASE beam.
The FEL radiation is diffracted by the electrons in the electron beam from the axis outwards. It is a slow effect, that makes the outer beam electrons interact in the undulator with radiation produced by electrons closer to the beam core. The result is some transversal coherence being introduced to the SASE pulse (see Fig. 1.16) [25, 29]. In HGHG a high degree of transversal coherence is inherited from the seed laser.(see Fig. 1.17).
The longitudinal coherence of SASE pulses is poor. The coherence length is

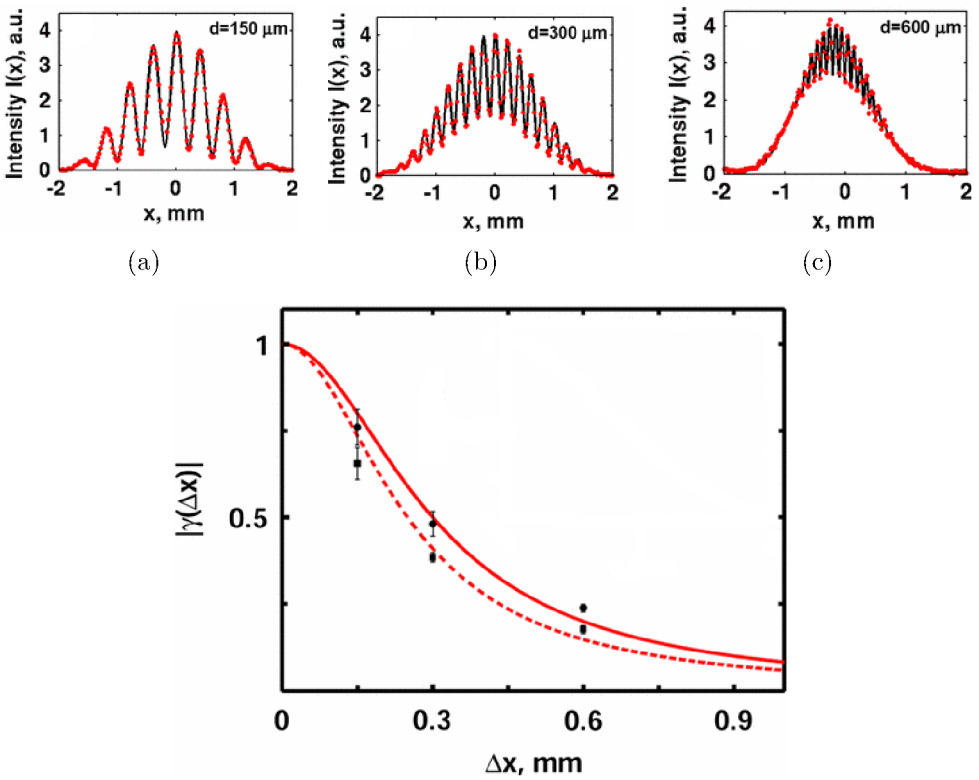

Figure 1.16: SASE transversal coherence before saturation at 13.5 nm, measured through a Young's double-slit experiment located 20 m downstream of the undulator exit. Fitted data of interference patterns from slits with 150 µm (a), 300 µm (b) and 600 µm (c) separation in the horizontal plane are shown. Figure (d) shows the degree of transversal coherence in the vertical (squares and dashed line) and horizontal (circles and continuous line) plane as a function of the slit separation. The points indicate experimental data, while the lines show a Lorentzian fit. Contrast decreases with increasing slit separation, indicating that transversal coherence of saturated SASE pulses is limited. Reprinted figure with permission from [25].

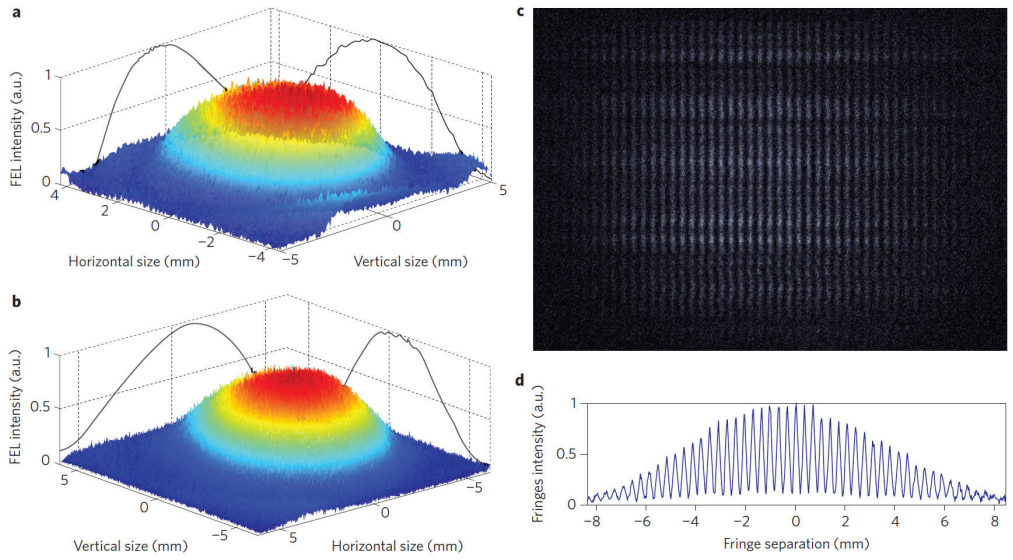

Figure 1.17: HGHG beam profile and transversal coherence. The beam profile 52.4 m (a) and 72.5 m (b) after the end of the radiator is Gaussian. The double-slit interference pattern (c,d) has been measured positioning two 20 µm slits, separated by 0.8 mm, about 8.5 m before the 72.5 m screen. The diffraction pattern shows high contrast. Figure reprinted by permission from Springer Nature: [26].

comparable to the cooperation length, with many modes at slightly different wavelengths being present. The number of modes depends on electron beam characteristics and FEL wavelength (see Fig. 1.12). A high degree of longitudinal coherence in seeded HGHG pulses has been shown at FERMI, by means of a longitudinal interferogram. Twin FEL pulses were generated by having two seed laser replica interact with separate portions of the electron bunch. The two pulses superposition produced clear interference fringes, showing a high degree of phase stability [2]. The results are shown in Fig. 1.18.

1.3 FLASH Seeding Infrastructure

FLASH is an XUV and soft x-ray facility located at DESY in Hamburg. It started under the name of **T**ESLA **T**est **F**acility (**TTF**) as an UV FEL with first lasing at about 100 nm central wavelength in 2001 [30]. It underwent several updates, the last one taking place in 2014. FLASH comprises of a single linac that accelerates electrons for two SASE FELs, FLASH1

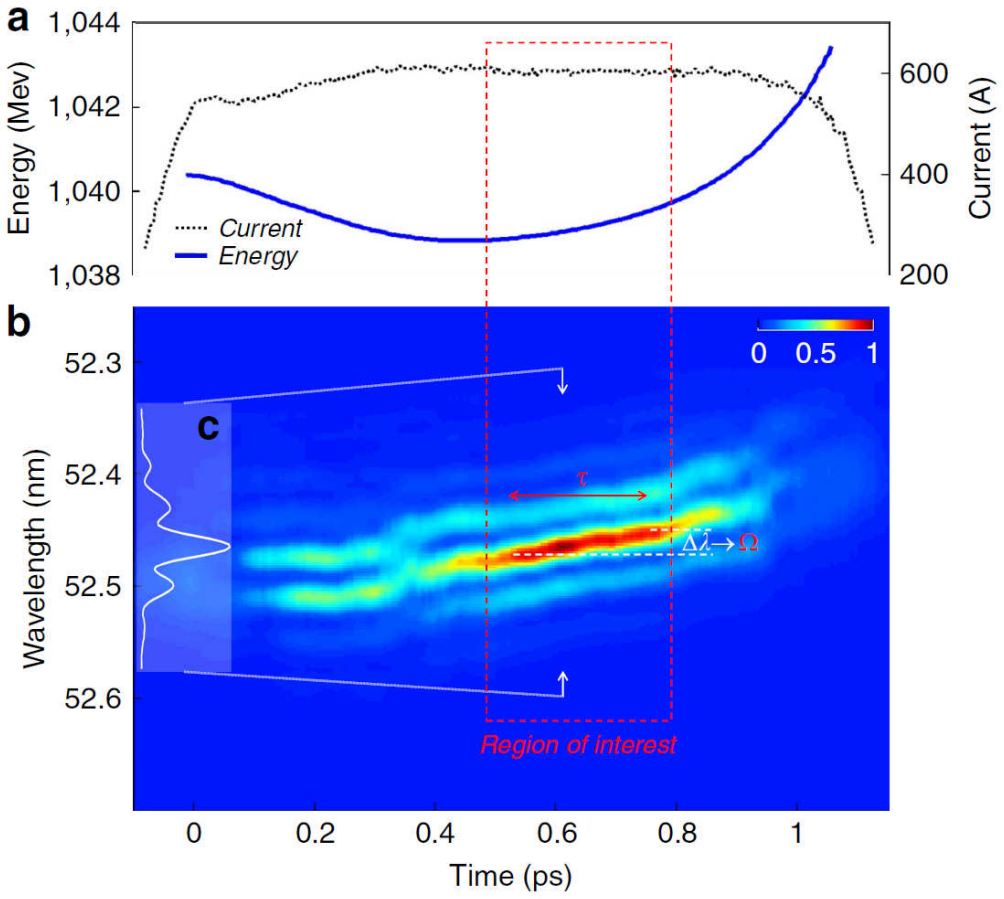

Figure 1.18: Longitudinal interferogram of an HGHG pulse at FERMI. The electron bunch current and mean energy (a) are compared to the seeded FEL pulse (b). The head of the bunch and of the FEL pulse are on the left. From the interferogram it is possible to measure the time duration τ and bandwidth $\Delta\lambda$ (in terms of wavelength) or Ω (in terms of angular frequency) of the FEL pulse. The high contrast of the fringes, as shown by a projection of the central section of the interferogram (c) indicates an high degree of longitudinal coherence in the pulse. Figure reprinted under the Creative Commons Attribution 4.0 International License from [2].

and FLASH2, and a seeded FEL called sFLASH. The three FELs can be operated simultaneously [31]. The FLASH layout is depicted in Fig. 1.19. FLASH1 features fixed gap undulators and provides SASE pulses between 51 nm and 4.2 nm to users in the FLASH1 Experimental Hall. FLASH2 is the latest addition to FLASH. It comprises of variable-gap undulators,

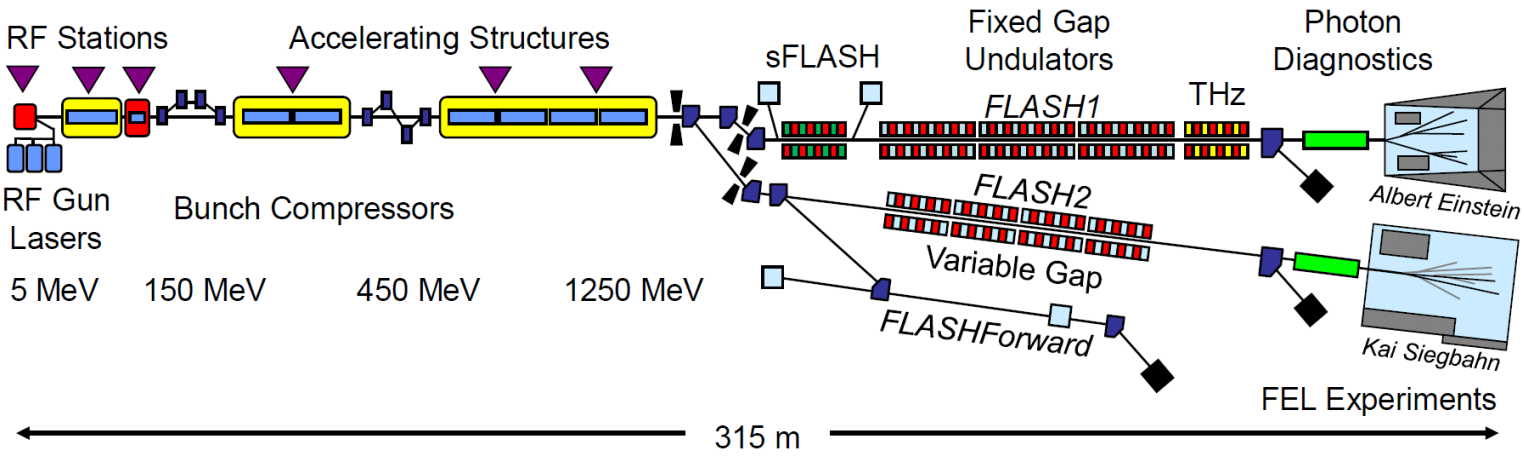

Figure 1.19: Sketch of FLASH layout. A photoelectron RF gun (far left) is used to generate the electron bunches. The electrons are then accelerated in the linac, made of 8 RF superconducting accelerating cavities and two magnetic chicanes to compress the bunch (left). At the linac exit a kicker and septum magnets switch the beam between the FLASH1/sFLASH and FLASH2 beamlines. The FEL radiation produced by FLASH1 and FLASH2 is delivered to photon experiments in two separate experimental halls, while sFLASH radiation is guided to an experimental hutch for FEL research. Figure courtesy of Siegfried Schreiber.

allowing its output wavelength to be tuned without changing the electron energy and independently from FLASH1. It is currently operated as a SASE FEL, providing light between 90 nm and 4 nm for users in the FLASH2 Experimental Hall.
sFLASH was started in 2010 to study possible seeding schemes for FLASH 2. It is used for FEL research and development. The light pulses generated are sent to an experimental hutch, where they are characterized and used to demonstrate novel opportunities of seeded FEL light applications. A prominent example is the development of an XUV pulse shaper that is the main subject of the present thesis. In the following sections the FLASH hardware components that are used for sFLASH operation are discussed.

1.3.1 Ultraviolet seed pulse generation and injection

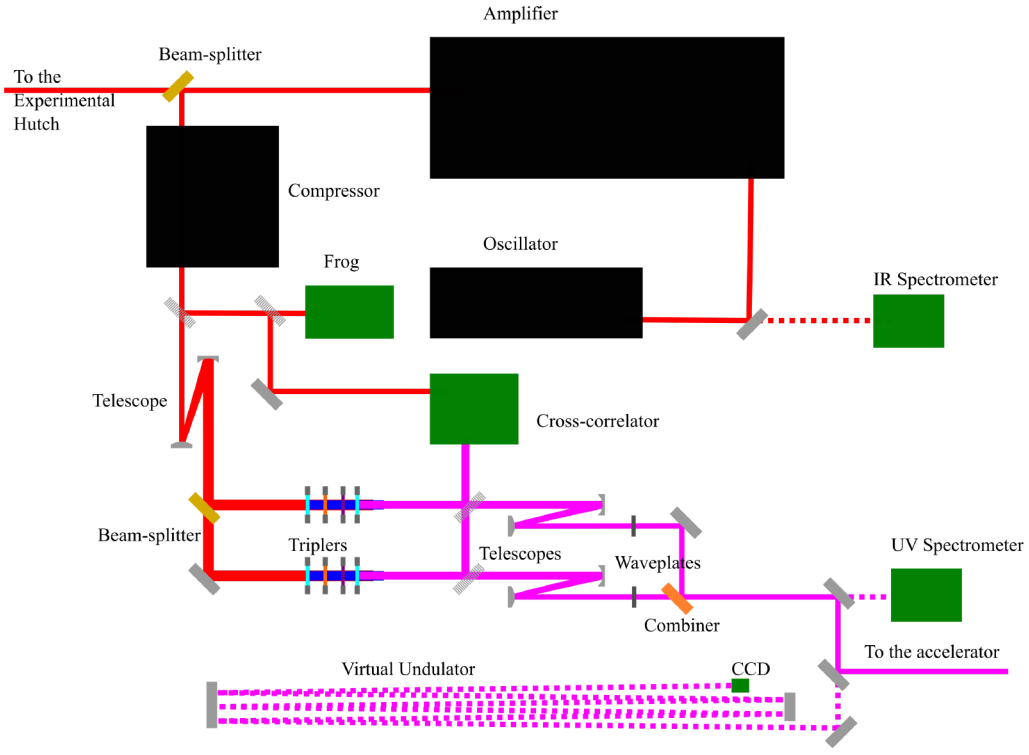

Figure 1.20: Seed laser setup. The diagnostic devices shown in the figure are discussed in Section 1.4.2.

The sFLASH seed laser is a solid state, **Ti**tanium-**Sa**pphire (**Ti-Sa**) commercial system based on the **c**hirped **p**ulse **a**mplification (**CPA**) technique. The laser and diagnostic setup is shown in Figure 1.20. The os-

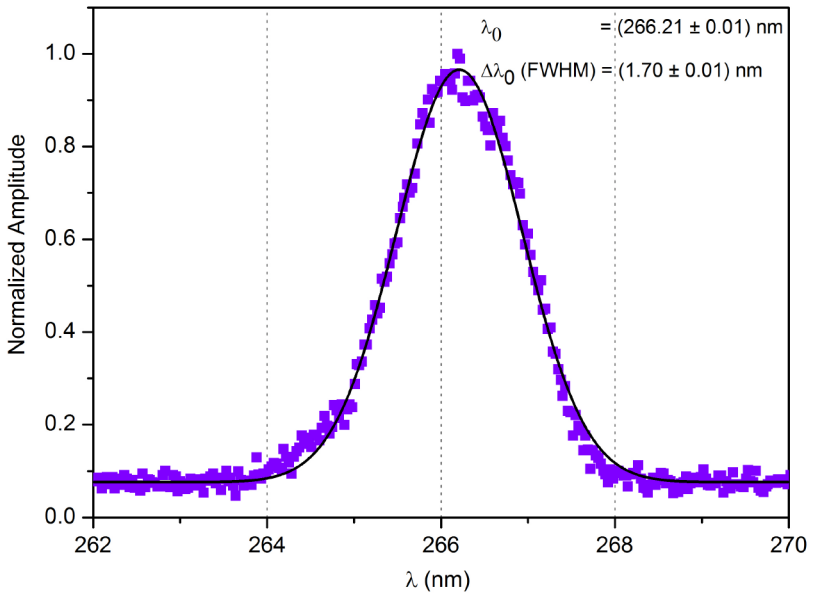

Figure 1.21: Seed laser spectrum. The experimental data has been fitted with a Gaussian distribution. Figure courtesy of Nagitha Ekanayake.

cillator generates 800 nm pulses, with approximately 5% bandwidth rms at 108.3 MHz and it is synchronized with FLASH **m**aster **l**aser **o**scillator (**MLO**). The MLO is the source of the synchronization signal for all FLASH components, including the photoinjector laser, **r**adio-**f**requency (**RF**) cavities and diagnostics. Two synchronization options are available to the sFLASH oscillator: an optical link with less than 30 fs jitter rms with respect to the MLO, and a more robust but less precise radio-frequency link with 50 fs jitter rms. The pulses from the oscillator are fed into a HIDRA two-stage amplifier (a regenerative amplifier followed by a multipass) based on the CPA technique [32]. The system runs at the accelerator's pulse-train repetition rate of 10 Hz. The amplifier is powered by flash lamps, that allow for an average pulse energy in excess of 50 mJ, at the price of lower energy stability and pointing stability compared to diode laser amplifiers. At the exit of the amplifier the pulses are split into two by a beam splitter: 15 mJ is used for seeding, while 35 mJ is sent to the experimental hutch for other uses (more on the topic in Section 1.4.3 and in Chapter 4). The 15 mJ pulse is compressed by a grating compressor down to about 30 fs duration fwhm. Pulse energy after compression is approximately 14 mJ, with ±2%

rms stability.
At the compressor exit the 800 nm beam is split into two pulses of equal energy. These two replicas are sent into two triplers (only one of which is used for HGHG, while both are used for EEHG), which are sets of non-linear crystals that generate the third harmonic of 800 nm, i.e. 266 nm, as detailed below. To keep the B-integral[4] below 1, and therefore avoid any risk of degradation of the Gaussian beam intensity distribution, the beam diameter before the triplers is expanded from about 7 mm to about 14 mm fwhm. The frequency up-conversion is generated using two β-**B**arium **bo**rate (**BBO**) crystals, one α-BBO[5] crystal and a zero-order waveplate. The first β-BBO crystal converts 800 nm to the second harmonic (400 nm), then the α-BBO crystal delays the 800 nm pulse, in order to temporally overlap it with the second harmonic. The zero-order waveplate rotates the polarization of the second harmonic by 90°, in order to make it parallel to the 800 nm polarization. Finally, the second β-BBO crystal combines them to produce the third harmonic of 800 nm (266 nm). The polarization of the UV beam is adjusted using quartz waveplates. The 266 nm pulses generated have a duration of about 150 fs, and energy in excess of 500 µJ. The bandwidth is in the order of 0.6% (see Fig. 1.21). At the exit of each tripler a waveplate is used to rotate the beam polarization, and each beam focus can be independently set using two telescopes.
The two UV pulses are then sent colinearly in the injection beamline. The injection beamline is made of 3 bandpass multilayer mirrors and a 4th multi-wavelength mirror for 800 nm, 400 nm and 266 nm. The 4th mirror is located inside the accelerator tunnel vacuum, where substitution of parts is problematic, therefore a multi-wavelength mirror has been chosen to allow for wavelength flexibility.

1.3.2 Relativistic electron bunches as gain medium

The FLASH photoinjector consists of a photocathode made of Cs_2Te positioned at the back plane of a 1.6-cell RF copper cavity. Three independent laser systems are employed to generate electron bunches from the photocathode. Two are used for standard operation: they are identical and

[4]The B-integral is a quantity used in Laser Physics to measure the accumulation of non-linear effects on the relative phases of the laser spectral components. Such phase variations can create beating patterns, that in high peak-power lasers can locally lead to high enough intensity to induce distortions in the pulse profile and damage of the optics [33].

[5] α-BBO and β-BBO differ in the position of the barium atoms in the reticule. This results in different birefringent properties. See [34].

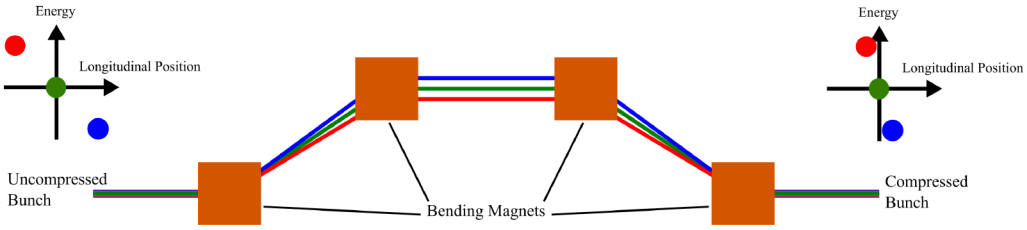

Figure 1.22: Schematic representation of a bunching chicane, or magnetic bunch compressor. High energy electrons at the end of the electron bunch (red) move along a shorter path compared to low energy electron at the head of the bunch (blue). This results in a reduction of the electron bunch length if the dispersive strength of the chicane and the induced electron energy chirp are tuned properly.

produce UV pulses of fixed pulse duration 6.5±0.1 ps rms. The third photocathode laser is used for the production of short, variable length electron bunches. It delivers pulses of 0.7-1.7 ps duration. Each one of them allows FLASH to be operated with 10 Hz bunch-trains of up to 800 bunches per train and 1 µs intra-bunch separation (1 MHz). With the seed laser repetition rate of 10 Hz one bunch out of each train can be seeded. Lasers suitable for 1 MHz seeding operation are currently in development.

The RF cavity in the photocatode is needed to quickly accelerate electrons to relativistic speeds, minimizing the beam emittance increase due to Coulomb repulsion between electrons. The longitudinal electric field in the RF cavity, generated by a 1.3 GHz wave, typically has a peak value of about 50 MV m^{-1}. It accelerates the electron bunch to an energy of about 5 MV at the photoinjector exit.

The main components of the FLASH linac are 8 superconducting RF modules and two bunch compressors. All the superconducting modules but the second accelerate the electrons using RF at 1.3 GHz. In order to lase the electron beam needs to have high peak current (around 500 A for HGHG and up to several kA for SASE), much more than the peak current of an uncompressed electron bunch from the photocatode (10-50 A). Therefore, the electron beam isn't accelerated on the crest of the radio waves, but on the falling edge. The resulting acceleration is slightly smaller, but it induces a nearly linear energy chirp in the electron bunch that is necessary for dispersive compression. The length of the uncompressed electron bunch is not negligible compared to that of the 1.3 GHz RF period, therefore the induced energy chirp is only approximately linear. To correct for this effect, the second RF module operates at the third harmonic of 1.3 GHz, i.e.

3.9 GHz, and is used to linearize the energy chirp of the bunch. The electron energy after the first module is 150 MeV.
The first bunch compressor is located behind the 3.9 GHz RF module. Bunch compressors consist of a magnetic chicane, where electrons with higher kinetic energy at the end of the bunch travel a shorter path compared to low energy electrons at the head. With proper tuning of the dispersive strength of the chicane the electron beam length can be decreased by more than one order of magnitude in a single chicane. The compression process is illustrated in Fig. 1.22. Due to Liouville's theorem[6], a side effect of the beam's longitudinal compression is the increase in its energy spread.
The first bunch compressor is followed by 2 further RF modules operating at 1.3 GHz. They accelerate the electron beam up to 450 MeV, and feed it into the second bunch compressor. The electron beam is then accelerated by 4 further RF modules, each operating at 1.3 GHz, up to a maximum energy of 1.2 GeV. The usual electron energy for sFLASH operation is about 700 MeV.
The linac is followed by a kicker and septum, which are two magnets needed to switch electron bunches to a different beamline within a few µs. They are used to send bunches to the FLASH2 undulator line, allowing FLASH2 to operate routinely in parallel with FLASH1 or sFLASH. The operation of three FEL lines in parallel is not performed on a regular basis.
The layout of the sFLASH and FLASH1 machine section is shown in Fig. 1.23. At its entrance two transverse collimators are located. They block electrons straying far away from the beam axis, due to Coulomb replusion, preventing them from hitting the undulators and damaging their permanent magnets. Afterwards the electrons enter a section called 'dogleg'. It is delimited by two dipoles and has a twofold purpose: electron energy collimation and seed laser injection. The first dogleg dipole disperses the electrons to different angles according to their energy, followed by energy collimators blocking electrons whose energy is far from the nominal one. The second dipole closes the electron dispersion, while allowing for the injection of the seed laser coaxially to the electron beam. It is followed by the **ORS** section (from **o**ptical-**r**eplica **s**ynthesizer, a diagnostic device for which this section and its two modulators were originally built [35, 36]). This section contains two electromagnetic modulators, the first with a horizontal electron wiggling plane, the second with a vertical wiggling plane. Both modulators have only 5 periods with $\lambda_u = 200\,\text{mm}$ and $K_{max} = 10.8$.

[6]Liouville's theorem states that the phase-space volume of a statistical distribution is conserved during its transformations. Therefore, the product between the volumes occupied by a statistical ensemble in space and in momentum is conserved.

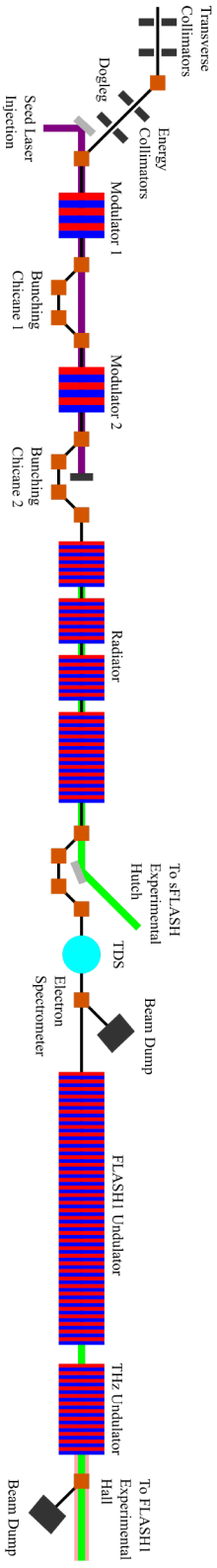

Figure 1.23: Sketch of the sFLASH and FLASH 1 beamline layout.

Each modulator is followed by a magnetic chicane.
The sFLASH main radiator is located downstream of the second magnetic chicane. It consists of 4 variable-gap permanent-magnet undulator modules. The first three are 2 m long, with $\lambda_u = 31.4\,\text{mm}$ and $K_{max} = 2.72$. The last module is 4 m long, with $\lambda_u = 33.0\,\text{mm}$ and $K_{max} = 3.03$. The undulators are separated by 0.7 m long sections, where an electromagnetic phase shifter[7], a quadrupole magnet for electron beam focusing and a movable diagnostic screen are located. Further screens are located in the magnetic bunching chicane and after the fourth module. The diagnostic screens are used to check the seed laser beam profile and focus position, as well as to align the electron beam and seed laser on a common straight trajectory along the ORS section.
The sFLASH radiator is followed by a further magnetic chicane, used to bend the electron path around the extraction mirror. After the chicane a **t**ransverse **d**eflecting **s**tructure (**TDS**) and an electron energy spectrometer allow for the characterization of the longitudinal phase-space distribution of the electron beam, i.e. the longitudinal electron density and energy distribution. The TDS setup is described in detail in Section 1.4.1.

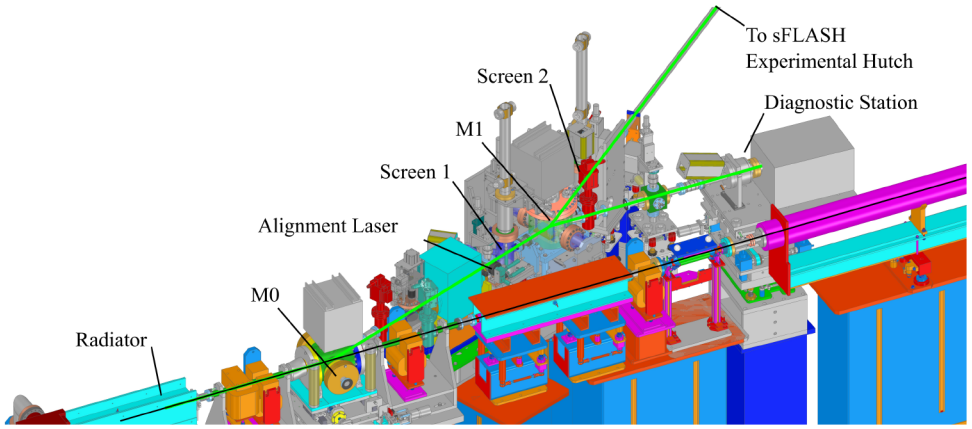

Figure 1.24: CAD model rendering of the first section of sFLASH extraction beamline, including the tunnel diagnostic station. Due to a magnetic chicane the electron beam bypasses the extraction mirror (effect on the electrons not shown in the picture).

[7]Phase shifters are electromagnets made of a pair of dipoles with alternating polarity. Their field can be varied in order to change the delay between electron bunch and FEL radiation, in order to inject radiation and micro-bunches in phase in the following undulator module.

1.3.3 Extraction beamline for amplified XUV pulses

The sFLASH extraction beamline transports the FEL pulses from the exit of the radiator to the tunnel photon diagnostic station and to the sFLASH experimental hutch. A CAD model of the extraction beamline is shown in Fig. 1.24.
A magnetic chicane displaces the electron beam vertically, allowing for the insertion of an extraction mirror (M0). The extraction mirror is made of a triplet of mirrors, each hit by the FEL radiation at 3.3° grazing angle, for a total deflection of 20° from the nominal electron orbit. The mirrors are coated with amorphous carbon, which has a reflectivity of approximately 90% down to about 9 nm, giving a total transmission for the three mirrors of about 70%. A narrow stripe at the top of the mirrors, 2.5 mm wide, is coated with nickel, to reflect light below 9 nm. Nickel reflectivity is above 70% at 3.3° down to about 2 nm radiation, leading to a combined transmission of approximately 35% for the three mirrors. The surface roughness of the mirror has been characterized to be in the order of 0.5 nm rms.
Next in the beamline is the alignment laser (a class 2 solid state laser) insertion point. A mirror can be moved into the beamline to deflect the pilot laser beam coaxially to the FEL radiation. Further down, a Ce:YAG screen can be inserted into the beamline. It is the first screen where seeded FEL pulse profiles can be imaged after the last radiator module. Behind the screen a switching mirror (M1) sends the FEL radiation either to the tunnel diagnostic station, comprising of an intensity monitor and a broadband spectrometer, or to the experimental hutch. Further details on the dignostic tools to characterize the seeded FEL radiation will be given in Section 1.4.3. The switching mirror is made of two mirror pairs, that can be inserted alternatively into the beamline. All mirrors are coated with amorphous carbon and nickel like the extraction mirror elements. The surface roughness of the mirrors is again 0.5 nm rms.
Between the switching mirror and the experimental hutch light travels through a 20 m-long beampipe. Two more Ce:YAG screens are used for the alignment. At the beampipe exit a further switching mirror (M2, not shown if Fig. 1.24, see Fig. 3.21) is located. It is coated like the previous mirrors in the beamline, and has the same surface roughness of 0.5 nm rms. It can be rotated to switch the FEL between the two main beamlines in the experimental hutch. The first one transports the FEL to a THz streaking setup (Sec. 1.4.3), the second one to the **X**UV and Soft **X**-ray **P**ulse **S**haper (**XXPS**).

1.4 Electron and Photon Beam Diagnostics

In a HGHG FEL the interaction between the seed laser, the electron beam and FEL components, including electron beam dynamics in the machine, determine the characteristics of the generated light pulses. Control over these parameters allows for tailoring the FEL output pulses. Therefore, accurate and as complete as possible diagnostics of electron beam, seed and FEL pulses are crucial.
In this section sFLASH diagnostics and tailoring options are discussed. First the electron beam components most important for seeding are presented. Next, capabilities of the seed laser diagnostics are discussed. Finally amplified FEL pulse diagnostics and tailoring options are the focus of interest.

1.4.1 Analysis and control of electron beam parameters

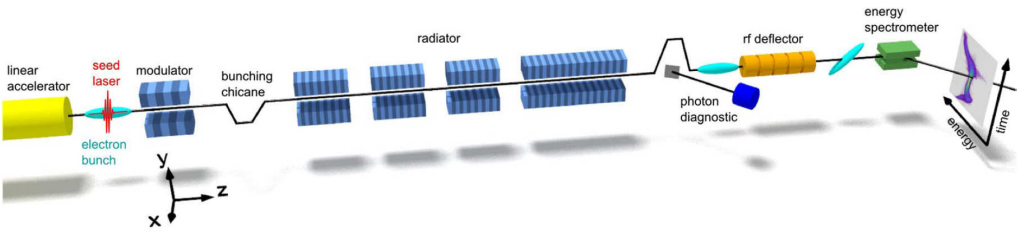

Figure 1.25: TDS and electron spectrometer location in the sFLASH setup. The electrons in the beam (light blue in the figure) are mapped vertically by the TDS according to their longitudinal position. The following dipole magnet disperses the electrons horizontally depending on their energy. This way the longitudinal phase-space distribution is mapped to the transverse planes and can be observed on a subsequent fluorescent screen. Figure reprinted under the Creative Commons Attribution 4.0 International License from [37].

Several parameters of the electron beam are crucial for a HGHG FEL: the electron mean energy, the beam orbit, the beam profile and the longitudinal phase-space distribution. The longitudinal phase-space distribution of a relativistic electron bunch is a plot of electron energy vs longitudinal coordinate in the bunch. It allows retrieval of important parameters such as energy spread and peak current.
The electron mean energy is estimated in two different ways. One estimate

is obtained by using the voltages and phases of the RF cavities to calculate the energy transferred to the electrons. The second estimate is obtained by using the bending radius of the electron beam due to the first dipole in the dogleg. The two estimates return similar results, typically within less than 1% difference.
The electron beam orbit is determined using Ce:YAG screens and **b**eam **p**osition **m**onitors (**BPM**s). BPM measurements are non-destructive and are used in real time by an orbit feedback software to keep the orbit constant in the beamline during FEL operation. It sustains the electron orbit by changing the magnetic field in several correction dipoles. This software compensates automatically for the effect of small beam parameter changes or drifts. The Ce:YAG screens are useful to overlap the electron beam with the seed laser.
The electron beam profile is defined by the emittance of the electron beam multiplied by the evolution of its beta function in the beamline. The detailed discussion of these concepts can be found in Particle Accelerator Physics books like [38] and [39] and is beyond the scope of this thesis. The emittance is determined by the injector, while the beta function changes along the beamline due to the magnetic optics (quadrupoles, solenoids and to a smaller extent undulators and dipoles). The beam profile can be measured in several positions along the beamline using **o**ptical **t**ransition **r**adiation (**OTR**) screens, allowing reconstruction of projected emittance and beta function.
The analysis of the electron longitudinal phase space is performed using a **t**ransverse **d**eflecting RF **s**tructure (**TDS**) and an electron spectrometer (see Fig. 1.25). The TDS consists of an RF cavity with the RF electric (and magnetic) field perpendicular to the electron beam direction of motion, instead of coaxial geometry like in RF cavities in a linac. The electrons in the beam receive different transversal acceleration depending on the longitudinal position in the beam. The RF cavity is followed by an electron spectrometer, consisting of a magnetic dipole that disperses the electrons according to their energy in the plane perpendicular to the one in which the TDS acts. The electrons are detected on a fluorescent screen, where electron energy as a function of the bunch longitudinal coordinate is measured with 10 fs resolution [37, 40].

For optimal HGHG performances the electron beam trajectory from the modulator entrance to the radiator exit should ideally be a straight line. Strong kicks in the electron bunch trajectory deteriorate the alignment between the microbunches and the undulator magnetic field and should be kept below 1 µrad per magnet, according to experience. Operation experience at sFLASH has shown that with bigger bends in the trajectory FEL

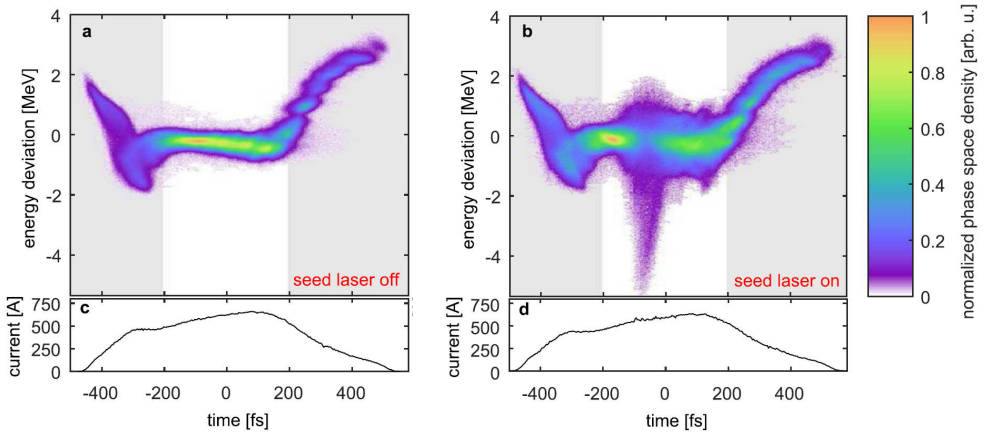

(a) (b)

Figure 1.26: Typical measurement of the longitudinal phase space distribution of an electron beam used for seeding with the seed laser off (a) and on (b). Figure reprinted under the Creative Commons Attribution 4.0 International License from [37].

lasing is poor or absent.
To maximize the FEL power output the electron beam profile must be kept as small as possible in the radiator. Several approaches are in use, from the periodic FODO transport (see [38] and [39]), to a ballistic transport (where no focusing magnets are used in the undulator, to avoid unwanted kicks due to the magnet slight misalignment), to irregular empirically-optimized transport [41]. The ballistic transport is used in sFLASH to minimize orbit kicks. The energy spread can be tailored to slightly increase or decrease the FEL bandwidth, but usually it is kept as low as possible, in order to maximize the FEL power output. The energy chirp in the seeded part of the beam can be tuned: while no energy chirp is usually preferred, a linear energy chirp can be introduced to generate chirped FEL pulses with increased bandwidth.
Optimal bunch compression is also crucial for HGHG operation. The beam current must be high in order to increase the FEL output pulse energy, but not so high that collective effects in the electron bunch due to Coulomb repulsion spoil the microbunching in the bunching chicane before the radiator. In addition the area of the electron bunch with high current and desired energy spread and energy chirp must be longer than the seed laser pulse length, to minimize the effect of seed and electron timing jitter on FEL output.

The seed laser defines a straight line on the Ce:YAg screens throughout the machine, which is used as reference for a straight electron orbit. While the electron beam profile is measured using the OTR screens, all remaining electron beam parameters, as well as the intensity and longitudinal position of the seed laser modulation, are characterized using the TDS and the electron spectrometer. Typical measurements of the longitudinal phase space distribution of the electron beam used for seeding, with and without seed laser modulation, can be seen in Fig. 1.26. The two extremities of the bunch are off-resonance and have bad emittance, therefore even if hit by the seed laser they will not lase. Most of the charge is concentrated in the middle of the bunch, which has a flat energy profile. When the seed laser is on, the electron bunch is energy and density modulated, respectively. The induced modulation is symmetrical with respect to the energy axis, but these measurements were taken after the radiator during FEL operation. As expected, the seeded electrons lost energy to the FEL radiation.

1.4.2 Experimental tools to diagnose the ultraviolet seed beam

The diagnostic devices used for monitoring the seed laser parameters are shown in Figure 1.20. A commercial GRENOUILLE setup is used to characterize the 800 nm pulses that enter the tripler for frequency upconversion. It is a variation of a **f**requency-**r**esolved **o**ptical **g**ating (**FROG**) providing full temporal and spectral diagnostic of the near-infrared laser pulses in real time. The 266 nm seed pulses are diagnosed using a spectrometer to determine the spectrum and a cross-correlator to measure time duration and time profile. The cross-correlator is described in detail in Chapter 3.
The transverse overlap of seed laser and electron beam in the modulator is achieved by aligning the two beams on Ce:YAG screens right before and after each modulator. These screens considerably overestimate the electron beam size (OTR screens must be used for accurate measurements), but the electron beam center can be determined with sufficient accuracy. The overlap is optimized in the end by maximizing the electron beam modulation signal on the TDS.
Though seed photon beamline diagnostics are sufficient to establish laser-electron overlap, there is in principle no diagnostic at the interaction point that can determine the transverse profile of the focused seed laser, i.e. the exact seed power density interacting with the relativistic electrons. To circumvent this limit, a 'virtual undulator' has been set up. It is an optical

beam line in the seed laser lab that transports the leakage of the UV beam through one of the mirrors in the injection beamline up to a CCD camera whose distance from the tripler is the same of the modulator center. This setup is used for real time monitoring of the seed laser focus.
The 800 nm compression is usually optimized either for maximum UV output power or for minimum seed duration. The power and polarization of the seed pulses can be tuned using a pair of waveplates and polarisers. They are used to optimize the modulation of the electron beam.
The only flexible tailoring option available for the seed is a pair of glass wedges, that can be used to change the seed pulse duration by changing the amount of energy chirp in the seed laser. In order to increase the control on the seed laser a UV pulse shaper is being developed. More information on pulse shaping can be found in Chapter 2.

1.4.3 Characterization of amplified XUV FEL pulses

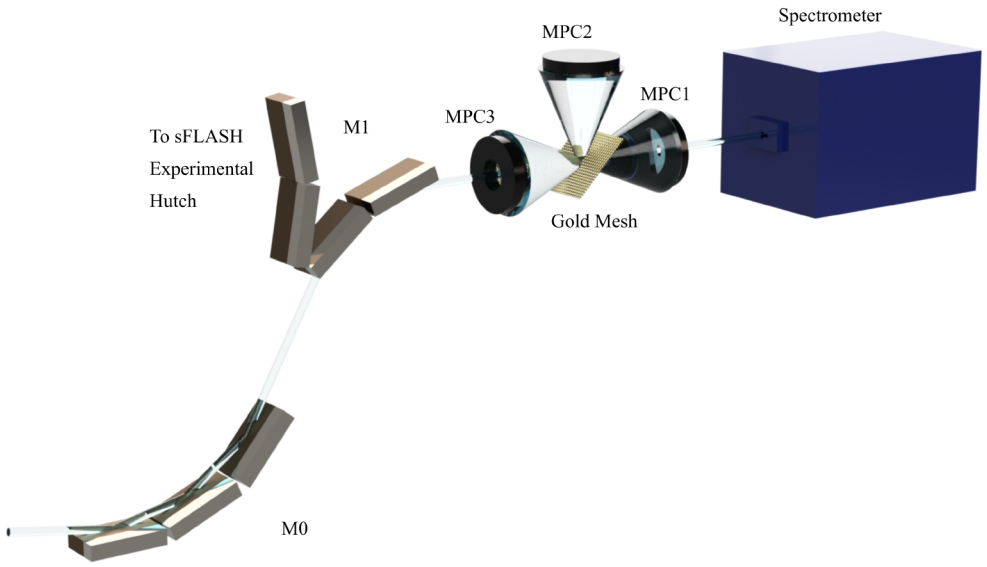

Figure 1.27: sFLASH diagnostic station. The FEL pulses at the radiator exit are reflected from the three-element extraction mirror, and then sent by the two-element switch mirror to the tunnel diagnostic station. They pass through a golden mesh that reflects some of the photons to three MCPs for pulse intensity measurement, while most of the beam reaches the slit of a broadband spectrometer.

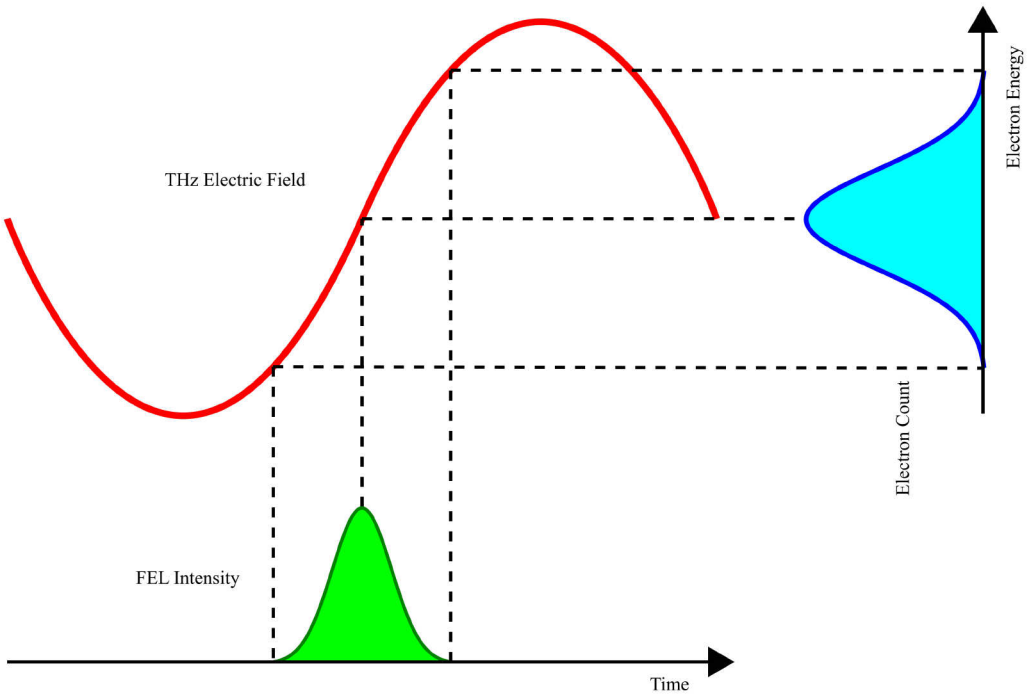

Figure 1.28: THz streaking principle. The XUV or soft x-ray fs pulse overlaps with the central part of the rising or falling edge of the THz pulse, which are much longer than the fs pulse. Atoms in the gas jet are ionized at a rate proportional to the fs pulse intensity, and the emitted electrons are accelerated by the THz electric field by a variable amount proportional to the emission time. It follows that the electron spectrogram is proportional to the fs pulse envelope.

Some FEL light diagnostics are already installed in a diagnostic station in the FEL tunnel, about a meter downstream of the extraction mirror M0. Additional diagnostic devices are installed in the experimental hutch.
The tunnel diagnostic station contains an FEL intensity monitor and a broadband spectrometer that can be operated simultaneously. A gold mesh is used to scatter part of the light for the intensity measurement, while the reminder reaches the spectrometer slit (Fig. 1.27).
The intensity monitor is able to measure pulse energies ranging from hundreds of pJ of spontaneous undulator radiation to hundreds of µJ of saturated HGHG pulses. High dynamic range is achieved using **m**icro-**c**hannel **p**lates (**MCP**s) operated at different high-voltage settings and located at three different positions with respect to the gold mesh. One MCP is located at 90° to the electron beam axis, while two MCPs have a hole in the center

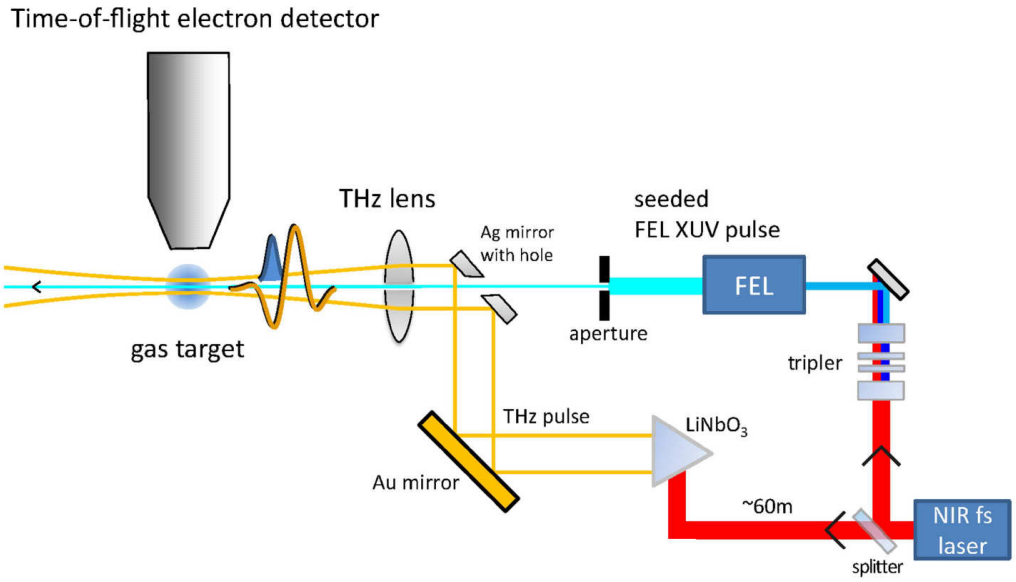

Figure 1.29: THz streaking setup at sFLASH. Part of the seed laser energy is used to generate THz pulses, intrinsically synchronized with the FEL output. The THz pulses are focused on a gas jet, where it overlaps with the FEL light coming through a slit. Figure reprinted under the Creative Commons Attribution 3.0 License from [42].

and are coaxial to the beam. MCP 1 detects photons scattered at small angles from the golden mesh ($>$ 50% gold reflectivity for angles smaller than 30° and wavelength $>$ 8 nm), MCP 2 detects photon reflected at 90° (between 15% reflectivity at 40 nm down to 0.1% at 13 nm) and MCP 3 detects photons back scattered (between 9% reflectivity at 40 nm down to about 0.05% at 13 nm).
The tunnel spectrometer is used to measure the FEL radiation wavelength and bandwidth between 1.7 nm and 39 nm. The rather broad range comes at the expense of resolution, which is according to specs:

$$R = \frac{\lambda}{\Delta\lambda} \approx 642 \tag{1.15}$$

while the actual value has been estimated to be about 400 [43]. The spectrometer is a commercial toroidal grating, flat-field spectrometer from McPherson. The light entering through a variable-width slit is dispersed by a concave gold coated grating and finally detected by a 40 mm MCP perpendicular to the dispersed beam located on the Rowland circle of the

grating. The MCP can be moved along the Rowland circle in order to cover the full spectrometer range.
To achieve higher spectral resolution, a high-resolution XUV spectrometer, a copy of the one described in Chapter 3, will be installed in the experimental hutch.
To estimate time duration and energy-chirp of femtosecond XUV and soft x-ray pulses THz streaking can be used. It is a non-destructive diagnostic technique that has been successfully used to characterize FEL pulses [44]. THz streaking setups have three main elements: a THz pulse, a gas target and a photoelectron spectrometer, e.g. a **t**ime **o**f **f**light (**TOF**) spectrometer. An XUV or soft x-ray fs pulse with a narrow bandwidth interacts with a gas jet in the presence of a strong THz field. The XUV pulse ionizes the gas, generating free electrons with small differences in kinetic energy. The rising and falling edges of the THz field are much longer than the ionizing FEL pulse duration. The zero-crossing of one of these flanks is overlapped with the XUV pulse, so that the emitted electrons receive an acceleration (or deceleration) linearly proportional to their ionization time. Thus, the kinetic energy of the photoelectron depends on its time of emission. This allows mapping of the FEL pulse power profile to the electron energy and spectrum, respectively (see Fig. 1.28). By comparing the electron spectra obtained from the rising edge of the THz field with the ones obtained from the falling edge it is possible to calculate the XUV pulse chirp [42].
In the sFLASH experimental hutch a $LiNbO_3$ nonlinear crystal hit by a 30 mJ 800 nm pulse split from the near-infrared drive laser for seeding is used to generate THz through optical rectification [45]. The layout is shown in Figure 1.29. This arrangement provides intrinsic synchronization with the seeded FEL signal, because both pulses are generated by the same laser source. The THz pulse has (0.5 ± 0.1) THz central frequency and a maximum field strength of $(80\pm10)\,\mathrm{kV\,cm^{-1}}$.
THz streaking can be used as a single-shot photon pulse diagnostic, when three detectors are used for each shot: two provide rising edge and falling edge measurements, while the third one measures ionized electrons unperturbed by the THz field. For a more detailed discussion the reader is referred to the literature, e.g. [46].

1.5 Status of Seeding R&D at FLASH

Seeding research and development at FLASH has started with studying the feasibility of HHG direct seeding schemes for XUV [47]. After an upgrade it was recommissioned as a HGHG FEL, with first lasing in 2015. Currently,

schemes to tailor the seeded radiation for advanced applications are being tested.

sFLASH can generate HGHG seeded pulses at the 7th (38 nm), 8th (33 nm)

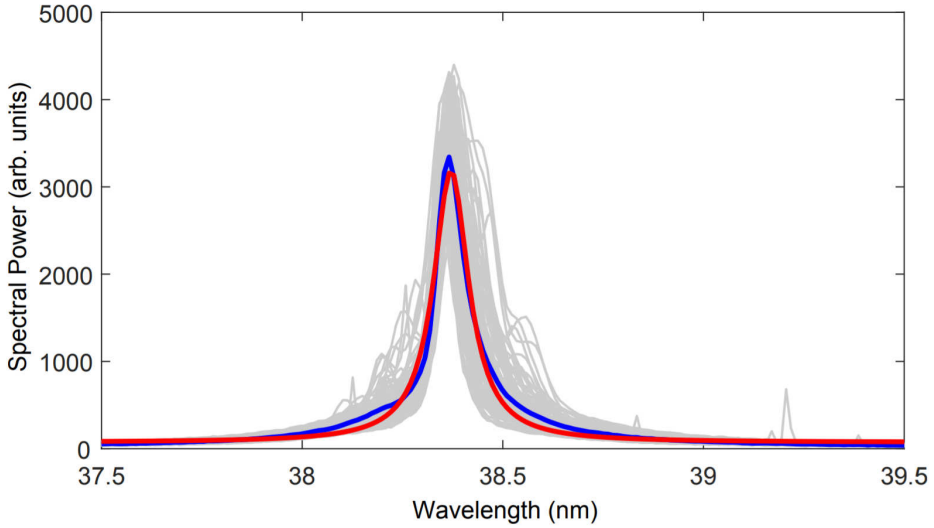

Figure 1.30: sFLASH HGHG spectra at the 7th harmonic. Spectra of 270 consecutive pulses (gray). The average spectrum (blue) is compared to a Lorentzian fit (red). Figure reprinted with permission of the author from [43].

and 9th (29 nm) harmonic of the 266 nm seed laser wavelength [48]. The typical time duration of the seeded pulses is below 100 fs rms. Values of (57±14) fs and (54±8) fs have been derived from TDS and THz streaking measurements at the 8th harmonic, respectively [42]. The shortest pulse duration of (33.0±3.9) fs has been measured for the 7th harmonic [43].

The spectral stability is rather good. However sometimes the pulses show secondary peaks (see Fig. 1.30), of which the origin is not yet understood. Spectral bandwidths between 0.3% and 0.6% have been measured. Fourier limited pulse duration with corresponding bandwidth would be between 9 and 19 fs at 38 nm and between 8 and 16 fs at 33 nm. These values are 2 to 4 times shorter than the characterized sFLASH pulses, indicating that the pulses are not yet at the Fourier limit. Future measurements using a higher-resolution spectrometer will be carried out as a function of seed pulse compression and machine settings in order to optimize the temporal and spectral pulse properties.

Average pulse energies on the order of (35.1±10.4) µJ have been measured for the 7th harmonic and slightly lower for the 8th and the 9th harmonics.

Typical pulse energy fluctuations at sFLASH are on the order of 30%. This can be attributed to the poor pointing and energy stability of the sFLASH seed laser [43].
The sFLASH operation will be further developed in several directions. The seed laser and its beamline are being upgraded to reduce pointing and energy fluctuations, while the addition of an UV pulse shaper is planned to increase tailoring opportunities for the optical seed. Furthermore, the EEHG seeding scheme is currently undergoing commissioning, to make shorter wavelengths available at sFLASH.

Chapter 2

Photon Pulse Shaping

Pulse shaping describes the capability of modifying the polarization, temporal profile or amplitude of coherent electromagnetic waves in a controlled way. Pulse shapers have been widely used in the field of ultrashort laser pulses, due to the high demand for tailored laser beams in nonlinear optics and short pulse spectroscopy.
In this chapter the basics of pulse shaping are described. Section 2.1 summarizes some particularly useful concepts in the field of ultrashort laser pulses, focusing on the time-frequency profiles of the pulses. A general introduction to laser beams can be found e.g. in [33] and [49] and is beyond the scope of this thesis. Section 2.2 introduces the 'Photonics Approach' to pulse shaping at short wavelengths, i.e. pulse shaping by means of optical devices in the XUV and soft x-ray spectral range. The photonics approach has been followed in the present work to develop the XXPS. More detailed information about optical pulse shaping can be found in [50] and [51]. Section 2.3 introduces the 'Machine Approach' to pulse shaping, i.e. pulse shaping of a seeded HGHG FEL pulse by tailoring the electron bunch and UV seed laser parameters. FEL pulse shaping was demonstrated for the first time at FERMI in Trieste, Italy in 2015 [4].
In this chapter the temporal and spectral distribution widths are expressed in terms of fwhm as common in optics, unless otherwise specified.

2.1 Time-Frequency Profile of Ultrashort Laser Pulses

A laser pulse is completely defined by its complex electric field $\mathbf{E}(t)$:

$$\mathbf{E}(t) = \mathbf{A}(t)\, e^{-i\phi(t)} \tag{2.1}$$

where $\mathbf{A}(t)$ is called the real amplitude (or envelope) and $\phi(t)$ is called the carrier phase. The complex Fourier transform of the electric field in the spectral domain $\tilde{\mathbf{E}}(\omega)$ is defined as:

$$\tilde{\mathbf{E}}(\omega) = \int_{-\infty}^{+\infty} \mathbf{E}(t)\, e^{-i\omega t} dt \tag{2.2}$$

It is an equivalent complete description, because $\mathbf{E}(t)$ can be obtained from $\tilde{\mathbf{E}}(\omega)$ using the inverse Fourier transform:

$$\mathbf{E}(t) = \frac{1}{2\pi} \int_{-\infty}^{+\infty} \tilde{\mathbf{E}}(\omega)\, e^{i\omega t} d\omega \tag{2.3}$$

The pulse shape in the spectral domain can be written in a form that is analogous to the electric field in the temporal domain:

$$\tilde{\mathbf{E}}(\omega) = \tilde{\mathbf{A}}(\omega)\, e^{-i\phi(\omega)} \tag{2.4}$$

where $\tilde{\mathbf{A}}(\omega)$ is called the spectral amplitude and $\phi(\omega)$ the spectral phase, with both being real functions.
The phase $\phi(\omega)$ can usually be written as a Taylor expansion (notable exceptions are phase jumps, like the ones that separate adjacent spikes in a SASE FEL pulse, and purely sinusoidal phases). The expansion reads as:

$$\begin{aligned} \phi(\omega) =& \phi(\omega)^{(0)}_{\omega_0} + \phi(\omega)^{(1)}_{\omega_0} (\omega - \omega_0) + \frac{1}{2}\phi(\omega)^{(2)}_{\omega_0} (\omega - \omega_0)^2 + \\ &+ \frac{1}{6}\phi(\omega)^{(3)}_{\omega_0} (\omega - \omega_0)^3 + \frac{1}{24}\phi(\omega)^{(4)}_{\omega_0} (\omega - \omega_0)^4 + \\ &+ ... + \frac{1}{n!}\phi(\omega)^{(n)}_{\omega_0} (\omega - \omega_0)^n \end{aligned} \tag{2.5}$$

where $\phi(\omega)^{(n)}_{\omega_0}$ is the n-th derivative of $\phi(\omega)$ calculated at ω_0. The term $\phi(\omega)^{(0)}_{\omega_0}$ is called absolute phase, or **c**arrier **e**nvelope **p**hase (**CEP**) (see Fig. 2.1). The CEP describes the delay of the carrier phase with respect to the maximum of the electric field envelope. The term $\phi(\omega)^{(1)}_{\omega_0}$ in the expansion indicates the group delay between the pulse and the arbitrary origin of time $t = 0$. The term $\phi(\omega)^{(2)}_{\omega_0}$ is called the quadratic chirp, or energy chirp, of the pulse. It indicates an increased pulse duration compared to the Fourier limit due to a delay of each frequency that linearly increases or decreases through

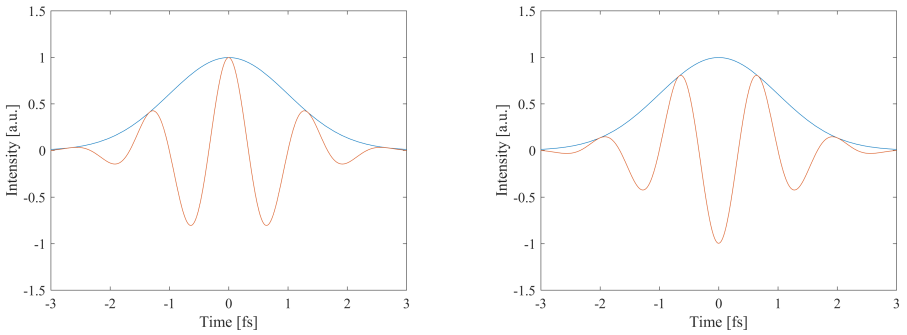

(a) (b)

Figure 2.1: Two pulses with same amplitude but different CEP (red). The picture shows two 400 nm Fourier limited laser pulses with 2 fs length. The pulse envelope (blue) is the same, but a CEP equal to 0 produces a cosine pulse (a) while a CEP equal to π changes the sign of the carrier (b).

the spectrum. The term $\phi(\omega)^{(3)}_{\omega_0}$ is known as the cubic phase. When not equal to 0 it indicates the presence of multiple pre- and post-pulses in the time domain.
The **t**ime-**b**andwidth **p**roduct (**TBP**), is the product of a pulse duration and spectral bandwidth:

$$TBP = \Delta t \cdot \Delta\omega \tag{2.6}$$

The minimum TBP can be obtained mathematically. For a Gaussian pulse one finds:

$$\Delta t \cdot \Delta\omega \geq 0.441 \tag{2.7}$$

A pulse with the minimum TBP product is said to be Fourier limited. For ultra-short pulses, Equation 2.7 can be rewritten more conveniently as:

$$\Delta t[fs] \cdot \Delta E[eV] \geq 1.825 \tag{2.8}$$

When the spectral bandwidth is fixed, the TBP can be used to indicate how close the temporal pulse width is to the Fourier limit.
Another useful parameter to relate the pulse time duration to its Fourier limit is the pulse complexity η. It can be seen as the ratio between the pulse length and the sharpest structure of the pulse in time (Δt and δt respectively) or, equivalently, in the spectral ($\Delta\omega$ and $\delta\omega$) domain (see Fig.

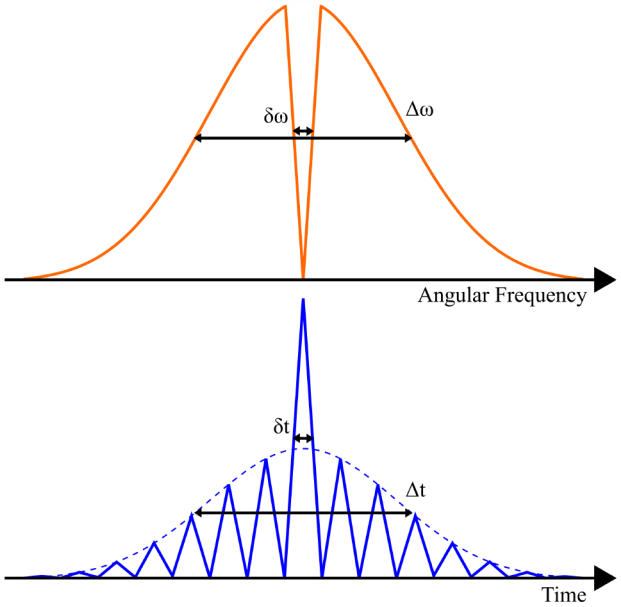

Figure 2.2: Complexity in the spectral and time domain. The complexity of a pulse indicates the ratio between the broadest and sharpest structures in the spectral ($\Delta\omega$ and $\delta\omega$) and time (Δt and δt) domain.

2.2):

$$\eta = \frac{\Delta t}{\delta t} = \frac{\Delta \omega}{\delta \omega} \tag{2.9}$$

For a Fourier limited pulse, $\eta = 1$. Particularly high complexity is achieved in double pulses or pulse trains, where the individual pulse duration is the shortest temporal structure present and η indicates the pulse train length in units of single pulse width.

2.2 Tailoring Amplified Light Fields: the 'Photonics Approach'

Optical devices have been widely used to shape femtosecond laser pulses in the infrared and the visible regime since this manipulation became popular in the early 90s. Many fascinating applications such as coherent control of quantum phenomena by tailoring the time-frequency spectrum of photonic reagents have been published in [52–57] and references therein. This section starts with a general discussion of infrared, visible and UV pulse shapers

(Sec. 2.2.1). Next, the 4f geometry, potentially the most flexible and most widely used pulse shaper setup, is described in detail (Sec. 2.2.2).

2.2.1 Infrared, visible and UV pulse shapers

An electromagnetic wave is fully characterized by its polarization, amplitude and phase. Tailored pulse shapes are generated by manipulating each of these parameters in a controlled way. Waveplates are typically used to change the polarization or intensity of a laser pulse. To modify its time-frequency spectrum, i.e. spectral amplitudes and phases, more complex devices are needed. Basic temporal shape changes, e.g. pulse stretching through the introduction of a linear chirp, can be obtained using relatively simple devices, at the expense of limited controllability. Some of the most common single-purpose pulse shapers are shown in Fig. 2.3.
Arbitrary pulse forms are achieved by manipulating the relative phase delay between different frequency components within laser pulses. Only longitudinally coherent light pulses, i.e. pulses where the phase relation between different frequencies is fixed shot-to-shot can be shaped in a controlled and reproducible way. When FELs are used as a light source, SASE pulses lack the necessary coherence (unless a monochromator is used, but the large reduction in power and high power jitter makes such approach unsuitable for most applications) to be used as a pulse shaping light source. Thus, seeded pulses are a prerequisite for pulse shaping.
Arbitrary pulse shapers can be operated in open loop or closed loop schemes. In open loop, the effect of the pulse shaper on the laser pulse is predicted analytically and the device is programmed accordingly. This approach is approximate and cannot always be used, especially when the characteristics of the incoming laser pulse are not well known. In closed loop operation the action of a particular pulse shape on a sample of interest is evaluated, for instance by recording a time-of-flight ion mass spectrum of the interaction products. Different pulse shapes, i.e. different shaper settings for amplitudes and phases, typically result in different fragmentation patterns. This information is continuously fed back into the data acquisition software. The software uses an algorithm (e.g. a genetic algorithm or an evolutionary algorithm) to tune iteratively the pulse shaper in order to obtain the target fragmentation pattern, i.e. an optimized time-frequency spectrum of the pulse for a particular laser-induced reaction pathway. Such an approach, although somewhat complex, can be regarded as a spectroscopic tool, because the optimized pulse contains all information about the induced dynamics on the ultrafast time scale [58]. It requires, though, some pulse-to-pulse stability of pulse properties.

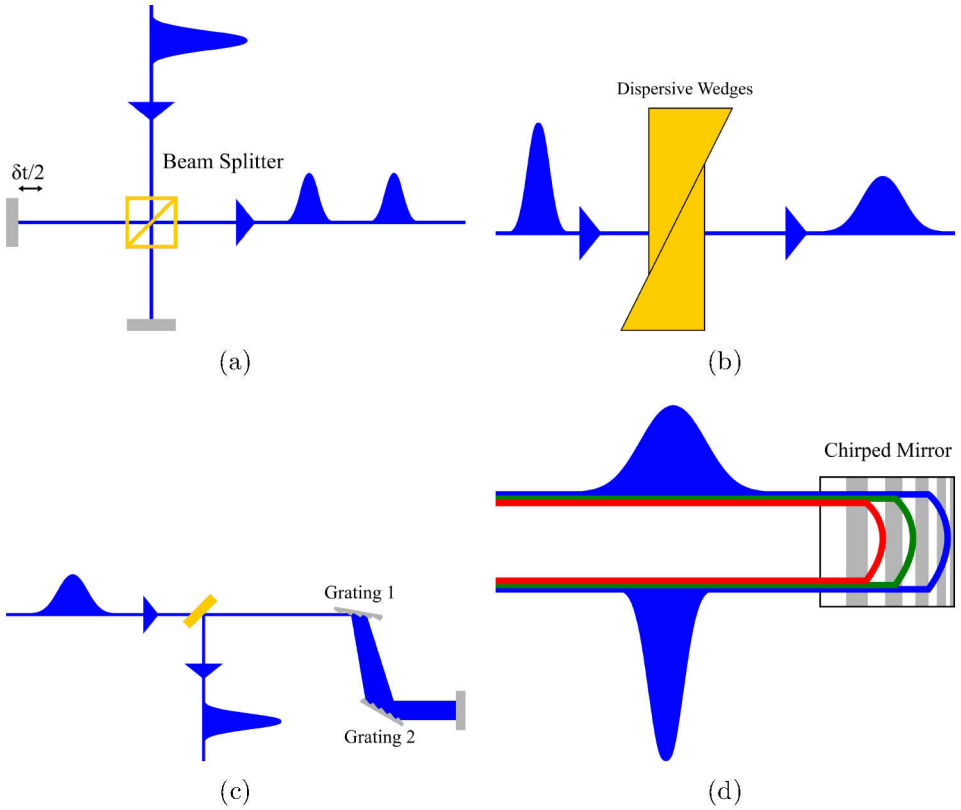

Figure 2.3: Common single-purpose pulse shapers. The Michelson interferometer (a) uses a semi-reflective beam splitter to produce two replicas of the incoming pulse with variable time separation. Propagation though a dispersive medium (b) increases the time duration of a laser pulse. The use of two wedges is a simple way of tailoring the increase in time duration. A grating compressor (c) is a relatively simple device that uses two gratings to compensate for the linear chirp in a pulse, thus making it shorter and increasing the peak power. It can also be used to stretch pulses. The sign of the linear chirp introduced or compensated depends on the orientation of the gratings. A chirped mirror (d) is a mirror where the penetration depth depends on the laser frequency. Thus, different frequencies follow paths of different length. Chirped mirrors can be used effectively to change the phase of a pulse down to the 4th order of the Taylor expansion, but there is no flexibility in their effect on a laser pulse. They are widely used to compress laser beams produced by FELs or other sources, leveraging the fact that such sources produce pulses with reproducible characteristics.

2.2.2 Grating compressor for spatial light modulation

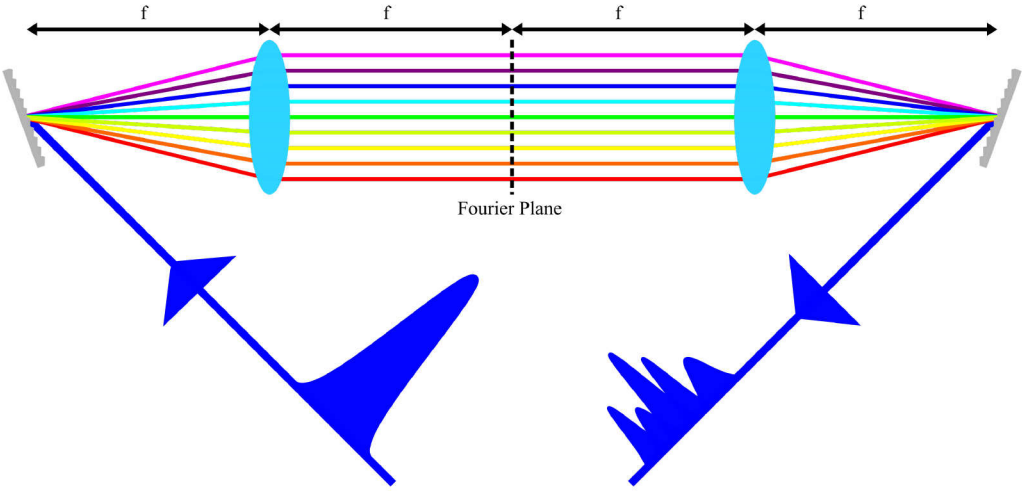

Figure 2.4: Sketch of the 4f geometry. An ultrashort collimated laser pulse is dispersed by the first plane constant-line-spacing grating. The first lens, placed at focal distance f from the grating, focuses each frequency at a different position onto the Fourier plane. The second half of the device is symmetrical to the first: the second lens directs all frequencies to the same position onto the second grating, that compensates the dispersion introduced by the first one. The results is a collimated output pulse identical to the input one, if no phase mask is introduced in the Fourier plane.

The 4f geometry, also known as 'zero dispersion line' or '4f-line', was first proposed in 1983 by Froehly and coworkers [59]. It is an optical device consisting of four elements: two identical gratings and two identical cylindrical lenses or mirrors with focal length f. The four elements are arranged in a symmetric configuration, as shown in Fig. 2.4. The symmetry plane is called Fourier plane, because in such plane the frequencies within the spectral bandwidth of the pulse are separated as in a Fourier transform.
The distance between each optical element and the next, Fourier plane included, is equal to the lenses focal length f (therefore the name '4f'). An ultrashort collimated laser beam is dispersed by the first planar constant-line-spacing grating. When the dispersed beam is focused by the first lens, a two-fold effect takes place. Because each laser frequency is coming at a different angle from the same origin point on the grating, which is located in one of the lens foci, the monochromatic beams are made parallel to each other. However, each monochromatic beam entering the lens is collimated

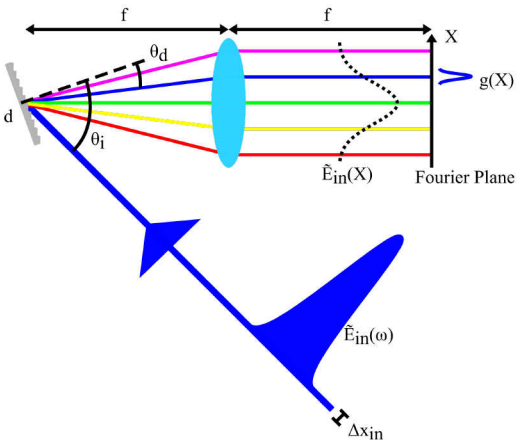

Figure 2.5: Most relevant parameters of a 4f setup. Only the first half of the setup is shown. f is the focusing distance, d is the grating line density, θ_i is the angle of the incoming pulse with respect to the first grating normal, θ_d is the angle of a monochromatic component after diffraction on the grating. $\tilde{E}_{in}(\omega)$ is the spectral intensity of the incoming laser pulse, $\tilde{E}_{in}(X)$ is the spectral intensity on the Fourier plane as a function of the position and $g(X)$ is the spatial intensity of a single wavelength.

and focused at distance f onto the Fourier plane. Because all but the central frequency are not focused in the mirror focal point, small aberrations are introduced. They are compensated by the second lens, therefore no net effect remains in the output pulse, but the aberrations must be considered when simulating the expected performances of optical elements (e.g. phase mask) placed in the Fourier plane. The focus width Δx_0 of each monochromatic component can be derived from Gaussian optics:

$$\Delta x_0 = 2ln(2)\frac{cos\theta_i}{cos\theta_d}\frac{f\lambda_0}{\pi\Delta x_{in}} \tag{2.10}$$

where θ_i is the angle between the incident laser beam and the normal to the grating, θ_d is the angle between the dispersed laser beam and the grating, f is the 4f focusing distance, λ_0 is the wavelength and Δx_{in} is the diameter of the incoming beam (see Fig. 2.5).
The position of each line on the Fourier plane X_k can be obtained from:

$$X_k = \alpha\omega_k \tag{2.11}$$

where ω_k is the frequency and α comes from the 4f geometry:

$$\alpha = \frac{\lambda_0^2 f}{2\pi c d \cos\theta_d} \tag{2.12}$$

where c is the speed of light and d is the grating period (Fig. 2.5). Thus, the resolution can be expressed as:

$$\delta\omega = \frac{\Delta x_0}{\alpha} \tag{2.13}$$

The calculated value $\delta\omega$ represents a lower limit for the spectral resolution of the pulse shaper in 4f geometry. Optics simulation software like Optics Studio/Zemax have been used in the present work to calculate the achievable resolution, taking into account optical aberrations. Usually the actual resolution of a 4f pulse shaper isn't limited by the focus size in the Fourier plane, but by the size of the active optical elements (e.g. liquid crystal pixel size) of the phase mask (see Section 2.2.3). The frequency resolution $\delta\omega$ of a pulse shaper can be Fourier transformed. The resulting time interval determines the temporal window T that can be shaped without distortions:

$$T = \frac{2ln2}{\delta\omega} = \frac{\Delta x_{in}}{\|v\|} \tag{2.14}$$

where v has the dimension of a velocity, and is given by:

$$v = \frac{cd\cos\theta_i}{\lambda_0} \tag{2.15}$$

2.2.3 Phase masks in the Fourier plane

A phase mask is an optical element used to control the spectral phase of individual frequency components within the laser bandwidth. It is placed in the Fourier plane of the 4f pulse shaper, where due to their spatial separation the mask can act on the individual frequencies, introducing variable delays. The most common phase masks for optical and IR pulse shapers are liquid-crystal pixel and acusto-optic modulator masks. Both variants cannot be used for XUV or soft x-ray applications because they are based on transmissive optics: the light passes through a liquid crystal in the first

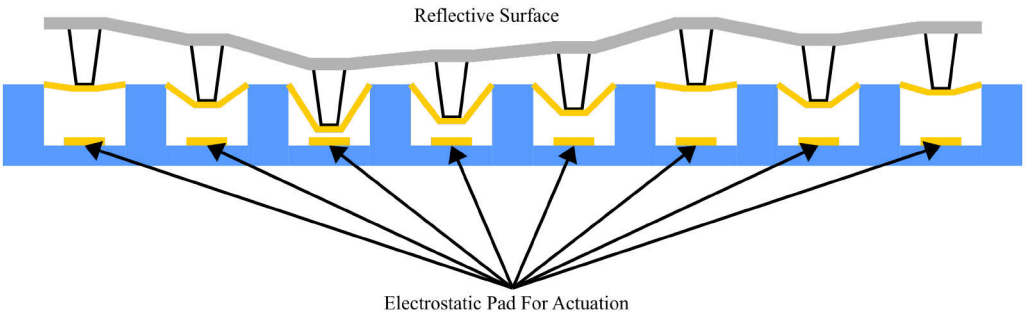

*Figure 2.6: **M**icro-**m**achined **d**eformable **m**irror (MMDM) working principle. An array of piezo actuators bends the mirror surface. Different voltages in the piezos translate to different positions.*

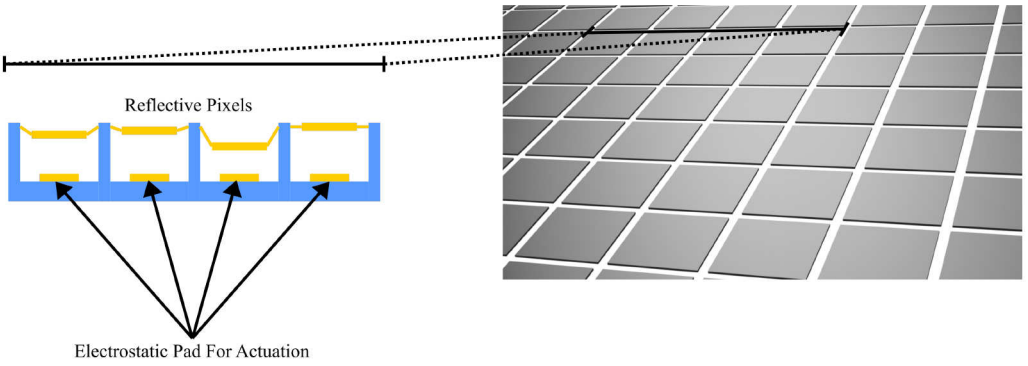

*Figure 2.7: 2D **M**icro **m**irror **a**rray (MMA) working principle. Piezo actuators determine the relative position of the reflective pixels.*

case and glass or a solid crystal in the second. Detailed descriptions of the working principles of these devices can be found in [50].
Several variants of reflective phase masks do exist that might be adapted to XUV and soft x-ray pulse shapers. The most widely used are **m**icro-**m**achined **d**eformable **m**irrors (**MMDM**) and **m**icro-**m**irror **a**rrays (**MMA**). MMDMs are made of a membrane coated with reflective material, as shown in Fig. 2.6. The membrane is moved by electrostatic actuators located behind. They allow for continuous variation of the phase along the Fourier plane, thus preventing the formation of artifacts in the shaped pulse due to pixelation. The drawbacks of this technology, however, are low spectral resolution, due to the mechanical difficulty of inducing small bending-radius curvature in a membrane, and permanent deformation over time.
MMAs, also known as **m**icro-**e**lectro-**m**echanical **m**irror **s**ystems (**MEMMS**), are arrays of miniature mirrors that can be moved independently (see Fig.

2.7). Each micro-mirror is anchored by springs and moved to the desired position through electrostatic forces. MMAs can be produced with high pixel density and custom coatings, resulting in high resolution shaping with high reflectivity. The main drawback of MMAs is the creation of pulse replicas due to the pixelation of the phase changes they introduce and due to the non-reflective gaps between the pixels [50].

2.3 Tailoring Relativistic Electron Bunches: the 'Accelerator Approach'

An alternative to this photonics approach consists in fine tuning the FEL parameters in order to tailor the generated pulses. The capabilities of such an approach were demonstrated at FERMI in 2015 [2–4]. This section starts with a short description of the FERMI FEL (Sec. 2.3.1), followed by a presentation of the 'Machine Approach' to pulse shaping (Sec. 2.3.2). A short comparison between the main advantages and limits of the two technologies is given at the end of this chapter.

2.3.1 Free-electron laser FERMI in a nutshell

FERMI is a HGHG FEL located at the ELETTRA Laboratories in Trieste, Italy. A single linac accelerates electron bunches for two FEL beamlines, called FEL-1 and FEL-2 (see Fig. 2.8). FEL-1 was the first FEL operational at FERMI. It is a single stage HGHG FEL generating UV and XUV radiation in the 20-100 nm wavelength range. It has been providing light pulses for user experiments since 2012. FEL-2 is a two stage cascaded HGHG FEL, pushing the wavelength range towards 4-20 nm [8]. User experiments at FEL-2 started in 2015.
The linac driving FERMI is made of copper, non-superconducting RF cavities. It can accelerate electron bunches up to energy between 1.0 and 1.5 GeV and a peak current between 500 and 700 A with 50 Hz repetition rate. It includes an x-band linearizer RF cavity, to improve the bunch energy profile, and a laser heater, to destroy unwanted microbunching generated by the injector [61, 62].
Two different laser systems are used to seed FERMI. One is a tunable **o**ptical **p**arametric **a**mplifier (**OPA**) system that generates deep-UV pulses in the 230-300 nm wavelength range, while alternatively the third harmonic of a Ti:Sa system can be used to seed at a fixed wavelength of 261 nm. Typical laser parameters are summarized in [62].

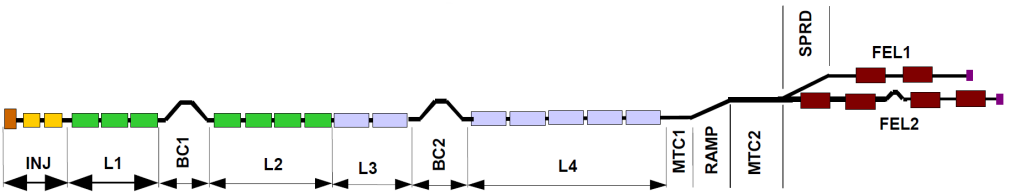

(a) Figure reprinted under the Creative Commons Attribution 3.0 License from [60].

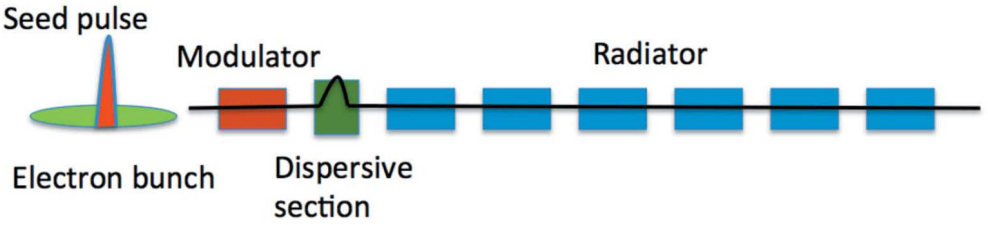

(b) Figure from [8], reproduced with permission of the International Union of Crystallography.

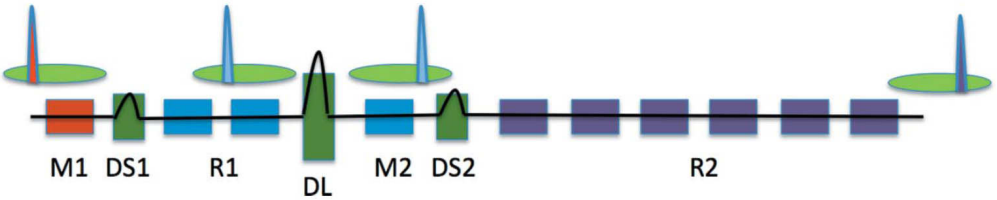

(c) Figure from [8], reproduced with permission of the International Union of Crystallography.

Figure 2.8: Sketch of FERMI layout. (a) Layout of the complete machine, with main section names: INJ - injector section (includes the laser heater), L1-L4 - linac sections, BC1-2 - bunch compressors, MTC1-2 - matching sections (each containing six quadrupoles to tailor the beam focusing properties and transversal size before the undulators), RAMP - transport line, SPRD - beam spreader section (a dispersive section comparable to FLASH dogleg). (b) Layout of FEL-1. The radiator is made of six undulator modules. (c) Layout of FEL-2. The first stage short radiator contains only two modules, identical to the ones used in FEL-1, while six longer elements form the second radiator.

The undulators used in in FEL-1 and FEL-2 are APPLE-II undulators [63]. Their structure allows them to create pulses with arbitrary polarization [64]. The FEL-1 uses six undulators, each 2.34 m long, while FEL-2 uses two 2.34 m-long undulators in the first radiator, and 6 2.40 m-long undulators in the second radiator. These radiators are by design far too short to reach SASE saturation at 700 A peak current or below, which minimizes the SASE background. The modulators are 3 m long, with 30 magnetic periods each. The typical spectral bandwidth of FEL-1 is in the order of 0.05% [64]. Depending on the machine settings FEL pulses close to the Fourier limit have been obtained [2].

2.3.2 Seed pulse, electron bunch and FEL process control

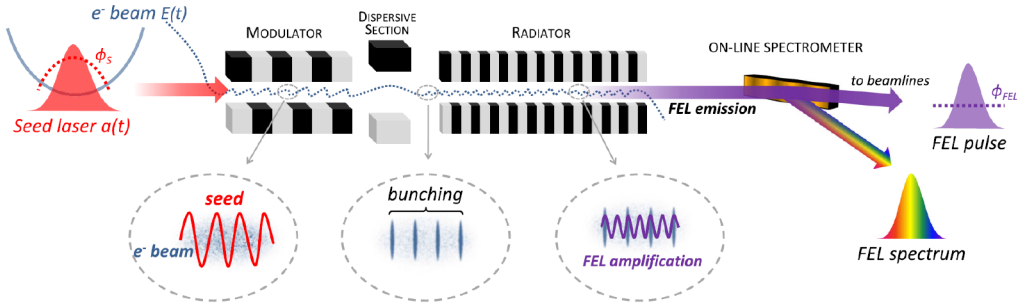

Figure 2.9: Pulse shaping setup at FERMI. The parameters that can be tuned are the seed laser and electron beam longitudinal profiles and the strength of the dispersive section chicane. By tuning these elements the bunching at the radiator entrance can be tailored, therefore determining the radiation characteristics after the FEL amplification process. At the end of the FERMI radiator, a grating is used to obtain real time spectral diagnostic. Reprinted figure with permission from [4].

The temporal profile of the pulses generated in a HGHG FEL is determined by the electron beam characteristics (1), the modulation introduced by the seed laser (2), the bunching chicane strength (3) and the FEL amplification process (4) (see Fig. 2.9).
(1) Important electron beam characteristics are longitudinal charge distribution, electron energy and energy spread. The longitudinal charge distribution acts together with the seed laser induced modulation on the temporal profile of the FEL radiation. The electron energy determines the output

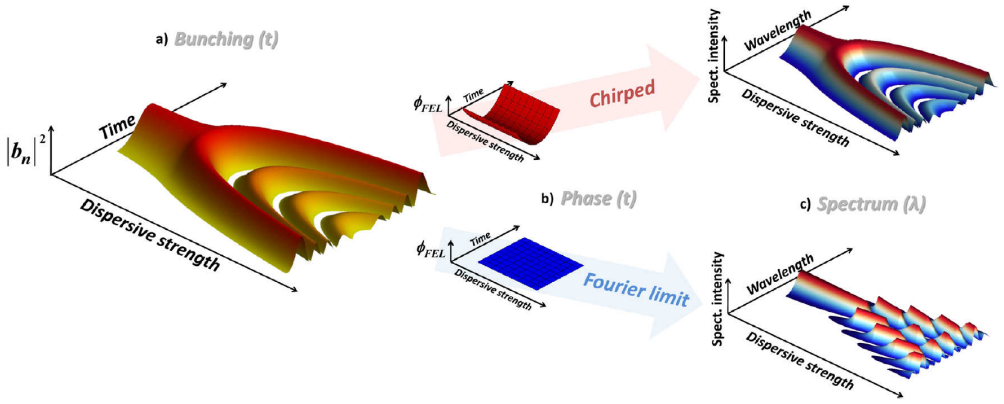

(a) Theoretical values.

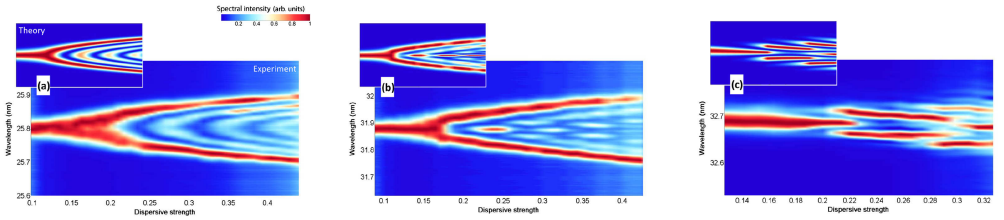

(b) Experimental data.

Figure 2.10: Experimental data showing chirp tailoring down to the Fourier limit at FERMI. (a) Theoretical prediction of the FEL spectrum as a function of the dispersive chicane strength. The chicane strength starts from a setting optimal for HGHG seeding, and is then increased to obtain overcompression. Results for a heavily chirped pulse and a Fourier limited one are shown. (b) Comparison between theoretical predictions and experimental results, in case of an heavily positive chirp of the seed laser (b.a), moderate energy chirp (b.b) or light negative chirp (b.c). In the last case, the spectrometer signature is compatible with Fourier limited pulses. Reprinted figure with permission from [4].

wavelength. An electron energy chirp in the bunch or other non-linearities will be transferred to the FEL pulse. Overall, the electron energy spread influences FEL photon pulse energy and its spectral bandwidth. (2) The seed laser modulation and magnetic chicane strength determine which parts of the electron bunch will radiate and with how much intensity. Up to a certain optimal modulation and chicane transfer matrix element R_{56} (3) the higher the modulation and chicane strength are the higher the bunching factors of the seed harmonics become. Beyond such a level overcompression

starts to take place, reducing the bunching factors. This effect can be used to generate FEL double pulses or pulse trains, by having sections of the electron beam where the laser modulation is far above the optimal value and due to overcompression and energy spread increase the electron beam does not radiate. (4) The FEL amplification process in the exponential regime far from saturation maintains the microbunching temporal profile, but for a small contribution to the phase.
The total HGHG FEL pulse phase can be written [4] as:

$$\phi_{FEL}(t) = n[\phi_s(t) + \phi_e(t)] + \phi_a(t) \tag{2.16}$$

where $\phi_s(t)$ is the phase contribution given by the seeding process, $\phi_e(t)$ is the phase contribution of the electron bunch energy chirp, n is the harmonic at which the radiator is tuned, and $\phi_a(t)$ is the contribution to the phase due to the FEL amplification process.
By means of tight fine tuning of the electron beam temporal profile and of the chicane strength, combined with pulse shaping of the seed laser, the FERMI team managed to produce seeded FEL pulses with a controllable amount of energy chirp [4], down to no energy chirp and the Fourier limit (see Fig. 2.10).
The main drawback of an optical short wavelength pulse shaper is its rather low transmission. The use of two gratings and at least 3 mirrors even in grazing incidence causes high losses (more on the topic in Chapter 3). The machine approach overcomes this problem, but suffers from intrinsic limits in the temporal profiles of the pulses that can be produced. First, due to the slippage of the radiation both in the modulator and in the radiator, neighboring parts of the seeded bunch influence each other preventing extremely small features from being present in the shaped FEL. Second, when multiple laser pulses (e.g. pulse trains) are used to seed the same bunch, their separation in the modulator must be sufficient to avoid cross talking [65].

Chapter 3

Design, Setup and Transmission of an XUV and Soft X-Ray Pulse Shaper

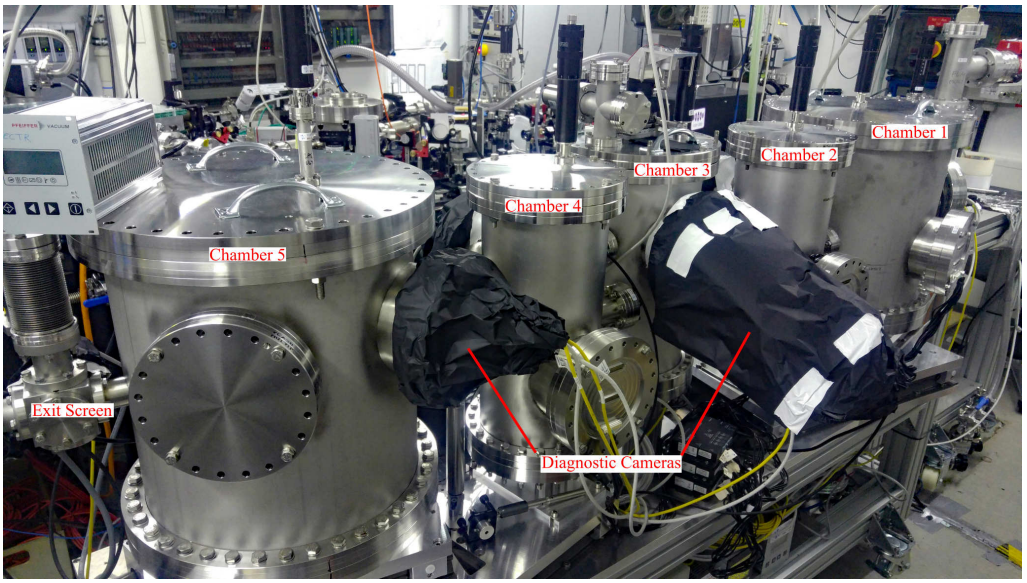

Figure 3.1: The XXPS in the sFLASH experimental hutch. The optical elements are arranged in five vacuum chambers connected by bellows. Due to this configuration the distance between chambers and therefore the focusing distance of the setup can be easily adjusted.

Since their introduction in 1983 [59], pulse shapers based on zero-dispersion compression in 4f-geometry, which have been discussed in Chapter 2, have

been widely used with laser pulses ranging from IR to UV. The transfer of this methodology to shorter wavelengths in the XUV and beyond has been prevented by the lack of suitable intense coherent light sources in these regions. With the advent of seeded FELs the situation has changed. In order to achieve good transmission and spectral resolution, grazing incidence of the light on the optics is mandatory. This results in a total length of about 2 m for the XUV shaper version with tight requirements on optics quality and alignment, keeping in mind that for spectral phase control a precision in the order of $\lambda/8$ is required.
The E**x**treme Ultraviolet and Soft **X**-Ray **P**ulse **S**haper (**XXPS**) is designed to operate between 4 and 40 nm. The device is shown in Figure 3.1. In its current realization it is optimized for XUV operations, between 15 and 40 nm. A different pair of gratings and optics with different coatings and shallower grazing angles will be needed for soft x-ray operation down to 4 nm. Due to the current limits in actuator accuracy also due to the $\lambda/8$ precision requirement, optical pulse shaping below 4 nm isn't possible with current technology. In the XUV realization, blazed custom made gratings will be used. Their line density will be such that all the harmonics of the sFLASH seed laser are dispersed to the same angle, with the n-th harmonic having maximum transmission at the n-th order due to the blaze angle. As a result, the shaper can be operated at different FEL wavelengths without needing realignment. Thus, increased ease of operation and potential for multi-color experiments are achieved. As a side effect even the fundamental can be used for proof-of-principle shaping, as will be demonstrated in the next chapter.
In this chapter the XXPS is described, focusing on how the design challenges have been addressed. In Section 3.1 an overview of the setup is given, while in Section 3.2 the optical components are described in detail. How transmission and resolution have been optimized is also discussed in this section. After a quick description of the mechanical aspects of the XXPS in Section 3.3, in Section 3.4 the built-in diagnostic tools assisting its operation or developed for its commissioning are presented. An FEL photon beamline has been built inside the sFLASH diagnostic hutch that connects the sFLASH beamline with the entrance of the XUV pulse shaper. It is described in Section 3.5. The measured XUV transmission of the XXPS in its current form is presented in Section 3.6.
In this chapter all incidence and dispersion angles are measured with respect to the surface of the reflecting optic. The design of the optical beampath has been done using the ray-tracing software OpticStudio (formerly Zemax), in conjunction with Gaussian optics calculations to determine focus sizes and Rayleigh lengths. The mechanical elements of the XXPS have been

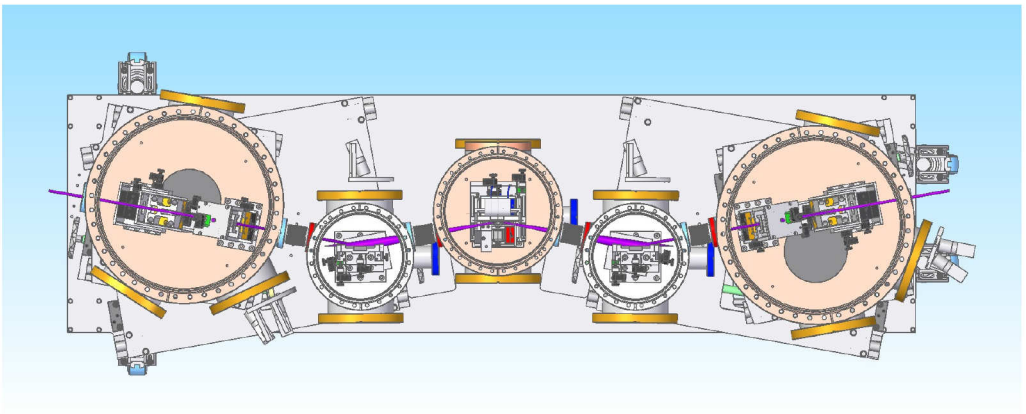

(a)

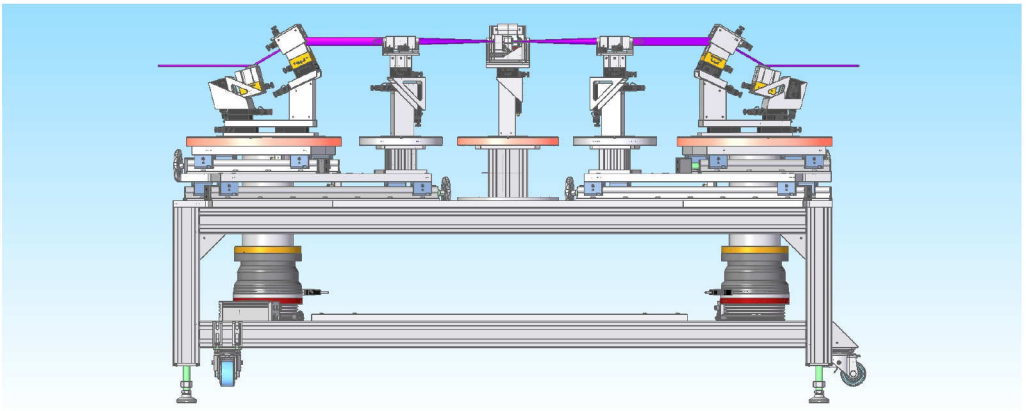

(b)

Figure 3.2: Top (a) and side (b) view of the XXPS CAD model. The top flanges have been removed in figure (a), while the whole vacuum chambers have been removed in figure (b). The beam path is shown in purple.

designed using Siemens Solid Edge CAD software.

3.1 Overview

The XXPS consists of seven main optical components: four focusing cylindrical mirrors, two plane gratings and a reflective phase mask (see Fig. 3.2). Five of them are the standard elements of a zero-dispersion compressor in 4f-geometry (see Chap. 2). The remaining two focusing mirrors have been added at the extremities of the beampath to facilitate alignment and to

decrease the beam footprint on the three optical elements in the center of the XXPS, in particular on the phase mask, in the plane perpendicular to the dispersion direction.
The modular arrangement of the optical components in individual vaccum tanks enables the adjustment of the focal distance f in between them without constraints, e.g. to compensate for divergence in the incoming beam. Furthermore, a future upgrade of the shaper in order to increase the spectral resolution in the Fourier plane or moving towards shorter wavelength is easily possible by replacing the gratings and the mirrors. Increasing the relative distances at shallower grazing incidence results in increased spectral resolution and transmission, respectively. Currently, the relative distance between the optics (focal length f) is 330 mm.
The five vacuum chambers are mounted to a single support frame, in order to minimized relative change in position of the optical components due to vibrations. To minimize those the XXPS support frame rests on passive damping elements, while magnetically levitated turbopumps are used to create and maintain high vacuum in the device. The turbopumps are insulated from the vibrations of the pre-vacuum scroll pump using soft-plastic connection pipes.
The XXPS is equipped with eight Ce:YAG screens to assist during the alignment. The beam position and profile on each screen is investigated using CCD cameras. A **w**hite **l**ight **i**nterferometry (**WLI**) setup is used to monitor the position of the reflective elements of the shaping phase mask on a shot-to-shot basis in real time (see Section 3.4.2).
For shaper commissioning and alignment two spectrometers were developed: one for XUV pulses and one for UV based commissioning using 266 nm radiation generated by frequency upconversion of the sFLASH Ti:Sa femtosecond seed laser.

3.2 XUV Optics

At the heart of the XUV pulse shaper are the seven optical elements. The layout of the XXPS optics is shown in Figure 3.3. Two cylindrical mirrors (SM2 and SM3) focusing along the y-axis and two plane gratings dispersing the FEL pulse in y-direction form the 4f zero-dispersion compressor. Various reflective phasemasks can be placed in the Fourier plane (see Section 3.2.4). Two extra mirrors (SM1 and SM4) are added symmetrically at the extremities of the 4f setup. These mirrors focus the beam along the x-axis perpendicularly to the Fourier plane onto the shaping mask, thus reducing the size of the beam footprint on the mask. The advantage is that the

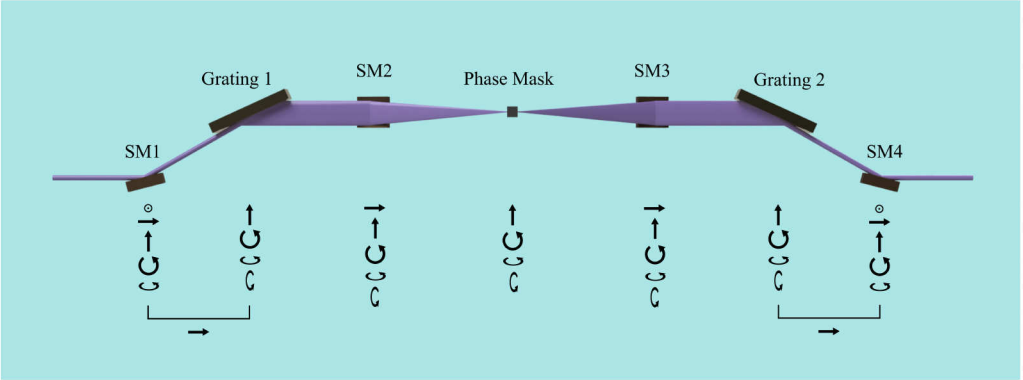

Figure 3.3: CAD representation of the XXPS optics (side view) and their effect on the beam. Under each optic, the adjustable degrees of freedom are shown.

phase mask dimension is reduced which relaxes the planarity (slope error) requirements. Furthermore, these mirrors reduce the size of the footprint on the 4f focusing mirrors minimizing spherical aberrations. Due to the bending of the beam at the entrance and exit of the XXPS, the shaper output is parallel to the ground.
The basic optical elements are described in more detail in Section 3.2.1. Given the space constrains in the experimental hutch of the sFLASH project the optical layout has been optimized for spectral resolution and overall transmission. These two important aspects are discussed in detail in sections 3.2.2 and 3.2.3 respectively. The interleaved lamellar-mirror assembly and the mico-mirror array that are forseen as phase masks are discussed in Section 3.2.4.

3.2.1 Mirrors and gratings

Symmetric mirrors SM1 and SM4 focusing in x-direction

The two mirrors constitute the first and last optics of the XXPS. They are cylindrical mirrors focusing orthogonally to the Fourier plane. The mirror at the pulse shaper entrance focuses the beam onto the phase mask, while the mirror at the exit collimates the beam. By reducing the size of the mask surface illuminated by the beam, it is possible to obtain better surface flatness on the mask reflective components, that can be shorter and therefore more stiff. Slope errors could be minimized on the lamellar double-mirrors as their surface was considerably flatter once the length of the stripes was reduced from 30 mm to 5 mm (see Section 3.2.4).

To maximize XUV transmission, the mirrors are coated with amorphous carbon. For soft x-ray applications close to the carbon K-edge (4.4 nm) nickel coated mirrors will be used. The current specifications can be found in Table 3.1.

SM1 and SM4	
Coating	Amorphous C
Curvature Radius	414.5 mm
Incidence angle	14.9 °
Focusing distance	810 mm
Size (H x W x T)	35 x 10 x 10 mm

Table 3.1: Technical specifications of SM1 and SM4.

Symmetric gratings dispersing in y-direction

As typical for the 4f geometry, the first grating in the pulse shaper disperses the spectrum while the second one recombines the colors in a parallel beam. For the initial commissioning two pairs of off-the-shelves gratings from Richardson Gratings (subsidiary of the Newport Corporation) were used, one optimized for a central wavelength of 266 nm and another for 38 nm. The final pair of gratings covering the XUV spectrum from 15-40 nm will be custom built. All of them will be plane constant line spacing gratings, but they differ in line separation, blaze angle and coating. Their specifications are summarized in Table 3.2.

		266 nm Richardson	**38 nm Richardson**	**Custom**
l/mm		300	2400	333
Dispersion	266 nm	3.8 nm/mm		4.0 nm/mm
	38 nm		0.54 nm/mm	0.53 nm/mm
Angle	Incidence	6°	4.7°	5°
	Dispersion	23.8°	25.1°	24.8°
	Blazing	10.4°	2°	9.9°
Coating		Al & MgF_2	Au	Au

Table 3.2: Gratings specifications.

The pulse shaper commissioning started using 266 nm pulses, the third harmonic of the Ti:Sa femtosecond sFLASH seed lasers. For basic alignment this wavelength has several advantages compared to short wavelength FEL

pulses. Air is transparent to UV light, making direct access to the XXPS during commissioning possible. Beam alignment can be easily checked at any position with the help of a specific laser card or even a piece of paper. Also, due to the much longer wavelength 266 nm pulse shaping requirements in terms of alignment and surface quality are more relaxed, making the first alignment simpler, even if not accurate enough for the following XUV applications.

The pair of gratings used for 266 nm commissioning are ruled gratings with 300 lines/mm operated in the first order. The resulting dispersion in the Fourier plane with $f = 330\,\mathrm{mm}$ is $3.8\,\mathrm{nm\,mm^{-1}}$. The gratings are blazed at 10.4 °. This blaze angle is close to the ideal one, which with a 6 ° incidence angle and a 23.8 ° dispersion angle would be 8.9° (in order to obtain specular reflection of 266 nm light to the first order). The gratings are made of BK-7 glass coated with aluminum. The aluminum coating is protected from oxidation by a thin layer of magnesium fluoride. Such coating has approximately 90% reflectivity at 266 nm. Due to the blaze angle almost all of the reflected light is diffracted to the first order: no other diffraction order was visible during operation.

The second step in the commissioning program made use of 38 nm radiation, the 7th harmonic of the 266 nm seed laser routinely generated by sFLASH using the HGHG seeding scheme. Here, a different set of ruled gratings with 2400 l/mm are operated in the first order. The resulting dispersion in the Fourier plane with $f = 330\,\mathrm{mm}$ is $0.54\,\mathrm{nm\,mm^{-1}}$. The 2 ° blaze angle is far from the ideal 10.2 ° that would be required with a 4.7 ° incidence angle and a 25.1 ° diffraction angle, but it still slightly improves transmission in the first order. This grating is coated with gold.

The final custom-made XUV grating for the shaper will have 333 l/mm, and will be blazed at 9.9 °. With an incidence angle of 5 °, the first order of the 266 nm light will be diffracted at 24.8 °. The grating equation reads:

$$d(\sin\theta_i - \sin\theta_d) = m\lambda \tag{3.1}$$

where d is the line density of the grating, m is the grating order, λ is the incident light wavelength and $\sin\theta_i$ and $\sin\theta_d$ are respectively the incident and diffracted beam angle with respect to the normal to the grating surface. It follows that the n-th harmonic of 266 nm n-th order will be diffracted at the same angle of the first order diffraction of 266 nm. Due to the blazed angle almost all the transmitted light will be diffracted into the desired order. This is of great importance for operating the short-wavelength pulse shaper at seeded FEL machines. Because HGHG and EEHG FELs produce only

harmonics of the wavelength they are seeded with, 266 nm at sFLASH, it follows that the final XXPS XUV grating can be aligned with 266 nm radiation and then operated at any wavelength generated by the FEL without any need of grating alignment change. The gratings will be gold coated, which has a reflectivity of about 50% in the XUV band (see Section 3.2.2).

Symmetric mirrors SM2 and SM3 focusing in y-direction

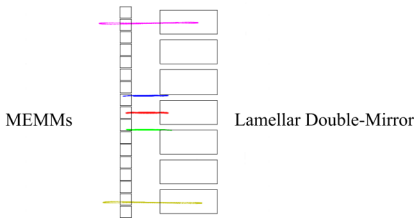

Figure 3.4: XXPS Fourier Plane Focus at 38 nm. The lines shown correspond to 38 nm (central line, red), 2‰ (green and blue) and 1% (magenta and yellow) bandwidth. They are compared to the reflective element size of the two shaping masks we plan to use (see Section 3.2.4).

Two cylindrical mirrors are used as focusing elements in the 4f geometry. Their purpose is to image each wavelength to a narrow line in the Fourier plane with a focusing length of 330 mm. Its width will be mostly determined by geometrical optics contributions. For the central wavelength at 38 nm a line-width of 2.8 µm was obtained by ray tracing simulations, both using the Richardson and the custom-made gratings. The theoretical focus size limit, calculated by means of Gaussian optics, would be only 0.39 nm with a 2 mm entrance beam diameter, and even smaller with a 5 mm diameter. Therefore Gaussian optics effects will be neglected in this section. Spherical aberrations increase the line width of wavelengths far from the central one. Furthermore, the line length in x-direction perpendicular to the Fourier plane is increased and a slight curvature is introduced (as shown in Fig. 3.4). However, both of these effects are negligible, compared to the 50 µm and 125 µm period of the initial phase masks we plan to use (see Section 3.2.4). The spherical aberrations introduced by the first focusing mirror have also negligible effect on the exit beam, as can be seen in Figure 3.5. These mirrors have been also coated with amorphous carbon for the best XUV reflectivity. Their technical specifications are listed in Table 3.3.

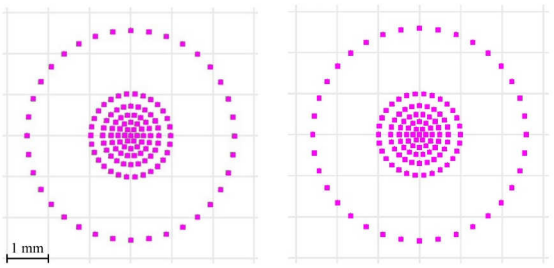

Figure 3.5: Comparison between input (a) and output (b) pulses by means of ray tracing. It can be seen that the frequency components within the spectral bandwidth of seeded FEL pulses are equally well overlapped, as only the last color drawn by the software is visible. No spatial chirp is introduced by the XXPS.

SM2 and SM3	
Coating	45 nm Amorphous C
Curvature Radius	114.6 mm
Incidence angle	10 °
Focusing distance	330 mm
Size (H x W x T)	30 x 30 x 10 mm

Table 3.3: SM1 and SM4 technical specifications.

3.2.2 Transmission through the shaper

Transmissive optical elements cannot be used with XUV and soft x-ray light, due to the lack of appropriate materials. The 90° and 45° reflectivity of single-layer mirrors is extremely low, while multilayer mirrors for XUV pulses have a reflectivity on the order of 40% for broadband mirrors, which can be increased to approximately 60% for narrow-band mirrors. Towards shorter wavelengths in the soft x-ray spectral range reflectivity is even lower. While such values are suitable for applications where one or two mirrors are needed, they are not good enough for the present device requiring seven optical elements. Therefore grazing incidence on coated silicon substrates is used.
The reflectivity data for XUV and soft x-rays is generated using E. Gullikson's tool on the Center for X-ray Optics and Advanced Light Source of the Lawrence Berkeley National Laboratory's website. It utilizes experimental data, supplementing it with interpolation or theoretical predictions when

no data is available [66].

XUV application

For operating the pulse shaper in the XUV 14.8° (SM1, SM4 and gratings) and 10° (SM2, SM3 and phase mask) reflection angles are used. Shallower angles were taken into consideration for the gratings, but 14.8° is a good compromise between reflectivity and dispersion. Note that the incidence angles on SM1 and SM4 and on the grating blazed surfaces are equal, in order to maintain the exit beam in the same horizontal plane of the entrance beam. The incidence angle on the focusing mirrors SM2 and SM3 and on the shaping phase mask is 10°. Shallower angles would have induced shadowing on the micro-mirror array that is planned to be used as a phase mask. The use of incidence angles on SM2 and SM3 different from that on the phase mask was simulated. It would have increased the aberrations in the Fourier plane and therefore it has not been realized.
The 266 nm test gratings as well as the final XUV custom-made gratings allow use of beams with a diameter of up to 5 mm. The 38 nm gratings for testing the device are shorter and can be used only with a pulse with a diameter of up to 2 mm.
All focusing mirrors are made of polished silicon substrates from Pilz Optics with 0.5 nm rms surface roughness and maximum radius of curvature errors 1.5% for SM1 and SM4, 1% for SM2 and SM3. They have been coated with amorphous carbon by Incoatec for maximum XUV reflectivity down to about 10 nm. The reflectivity of carbon at 10° and 14.8° is shown in Figure 3.6. Although amorphous carbon coatings would also be the best choice for the gratings and the shaping mask, we used these components with gold coating so far, because they are commercially available. The transmission for different material configurations, assuming 80% filling factor for the pixel mask and assuming conservatively only 30% transmission to the selected order for the grating is shown in Table 3.4. The 45 nm-thick carbon coating of the cylindrical mirrors has been seen to strongly absorb visible and 266 nm radiation. Reflectivity at 266 nm has been measured to be extremely low, with a combined reflectivity of two cylindrical mirrors, one at 14.8° with s-polarization and one at 10° with p-polarization, of about $2.7 * 10^{-6}$, corresponding to approximately 1.7‰ per mirror. As a result, alignment of the pulse shaper with four or more amorphous carbon coated optics using alignment lasers and UV radiation is challenging. While the low transmission of visible light can be overcome using a more powerful alignment laser and CCD cameras to look at the beam, intense UV radiation can modify the bondings of the carbon atoms, deteriorating

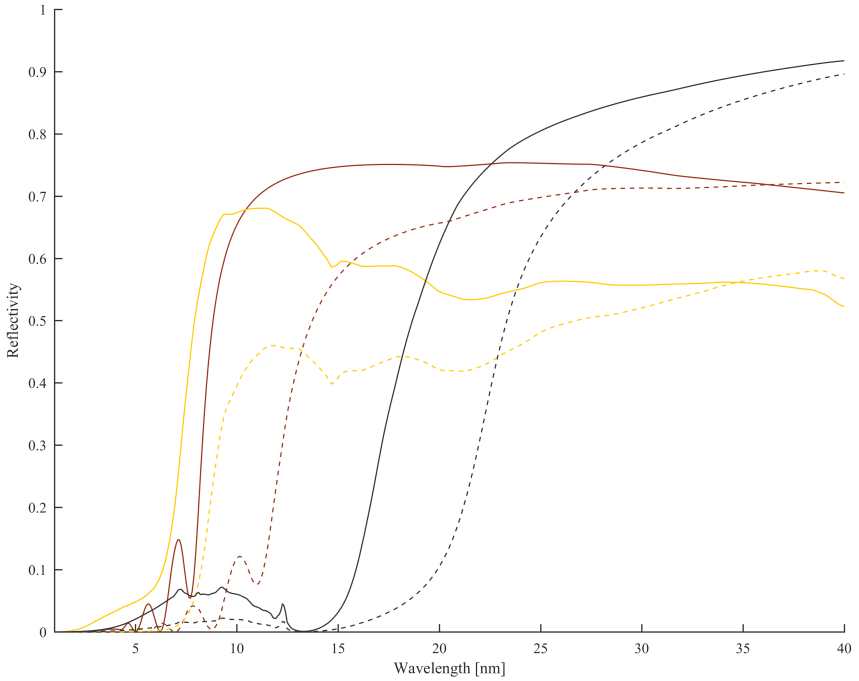

Figure 3.6: Reflectivity curve for carbon (brown), uncoated silicon (grey) and gold (yellow) at 10° grazing incidence for p-polarized light (continuous line) and at 14.8° for s-polarized light (dashed line). The surface roughness rms is assumed to be 1 nm. Data generated using E. Gullikson's tool on the Center for X-ray Optics and Advanced Light Source of the Lawrence Berkeley National Laboratory's website.

the amorphous carbon coating [67]. Therefore the use of high peak-power UV pulses should be avoided.
To circumvent this problem, un-coated silicon substrates can be used for alignment with both, visible alignment laser and 266 nm radiation. Because of the good reflectivity of silicon in the XUV (as shown in Figure 3.6), silicon optics can be used for pulse shaper operation above 20 nm, and replaced only for shorter wavelengths. The total transmission using uncoated silicon mirrors is shown in Table 3.5.

Soft x-ray implementation

High transmission is not achievable for FEL wavelengths below about 15 nm at 14.8° grazing incidence. Shallower angles and different coatings are neces-

XXPS XUV Transmission				
Gratings	**Mask**	38 nm	20 nm	15 nm
Gold	Silicon	0.6%	0.2%	0.1%
	Gold	0.5%	0.2%	0.2%
	Am. C	0.5%	0.2%	0.2%
Amorphous C	Silicon	1.0%	0.5%	0.02%
	Gold	0.8%	0.5%	0.3%
	Amorphous C	0.8%	0.6%	0.3%

Table 3.4: XXPS XUV transmission with various mask and grating coatings. The four mirrors are always assumed to be amorphous-carbon-coated. E. g. the 0.2% transmission of the device at 15 nm while using gold-coated gratings and a carbon-coated mask is obtained assuming 58% reflectivity for SM1 and SM4, 74% for SM2, SM3 and the phase mask, 43% reflectivity and 30% diffraction to the desired order for the gratings and 80% occupancy of the phase mask.

XXPS Transmission With Uncoated Mirrors					
Gratings	**Mask**	266 nm	38 nm	30 nm	20 nm
Gold	Silicon	6.7%	1.3%	0.7%	0.003%

Table 3.5: XXPS transmission with gold-coated gratings and uncoated silicon substrates for the remaining elements.

sary in order to achieve good transmission. Nickel reflectivity is high down to about 3 nm at 5° grazing incidence and down to 2 nm at 3° (as shown in Figure 3.7). Further down in wavelength the reflectivity drops steeply due to the L-I absorption edge at 1.2 nm. Thus, both solutions would allow the carbon K-edge at 4.40 nm to be reached.

However, there are several drawbacks in the use of such configurations. To keep the present resolution in the Fourier plane the focusing distance should be increased to 0.99 m if a 5° grazing incidence is used and to 1.67 m if a 3° grazing incidence is used. In turn, the total XXPS length would increase to 4.7 m and 7.3 m respectively. In addition, the increased FEL footprint on the optics would require longer mirrors and gratings by a factor 3-5 to keep the beam diameter at 5 mm. The overall XXPS transmission in both geometries for different laser wavelength is shown in Table 3.6.

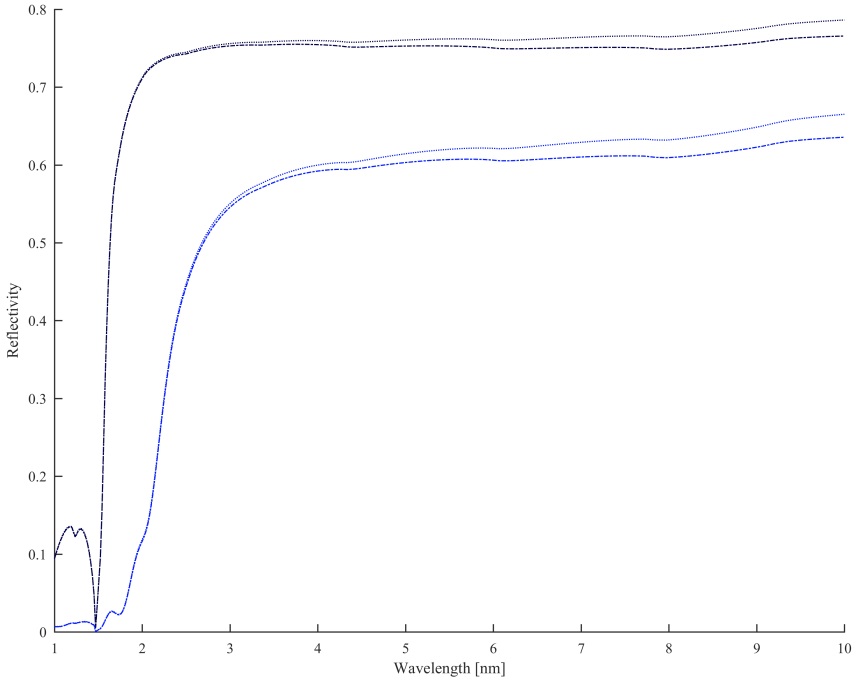

Figure 3.7: Reflectivity curve for a 30 nm nickel coating on a silicon substate at 5° grazing incidence (light blue) and at 3° grazing incidence (dark blue). The results are similar for s- (dotted lines) and p-polarization (dash-dot lines). Data generated using E. Gullikson's tool on the Center for X-ray Optics and Advanced Light Source of the Lawrence Berkeley National Laboratory's website.

3.2.3 Spectral resolution in the Fourier plane

The pulse shaping capabilities of the XXPS are determined by the spectral dispersion of the gratings and the width of the 'monochromatic lines' in the Fourier plane. The dispersion determines how many pixels of the Fourier mask are illuminated within the spectral bandwidth of the pulse and therefore can be used for shaping. The line width determines the minimum separation between frequency components whose spectral phases can be tailored independently.
The spectral dispersion of a pulse shaper is determined by the dispersion angle of the gratings and the focusing distance in the 4f geometry. The former was selected as a compromise between resolution and transmission (see Section 3.2.2). In the XUV realization of the XXPS the custom grat-

XXPS Soft X-Ray Transmission				
Grazing Angle	266 nm	38 nm	10 nm	4 nm
5°	39%	2.1%	0.4%	0.2%
3°	49%	3.4%	1.3%	1.1%

Table 3.6: XXPS transmission with nickel coatings as a function of grazing incidence angle.

ings will operate at a nearly constant dispersion angle of 24.8°, keeping the dispersion approximately constant throughout the XUV spectrum. The focusing distance of 330 mm was given by lab space constraints, i.e. to keep the total XXPS length at 2 m. Thanks to the modular, 5-chamber design of the XXPS, a longer focusing distance can easily be implemented using longer vacuum pipes to connect the chambers and replacing the focusing optics. The separation of the different colors ($\Delta\lambda = 2‰$) in the Fourier plane is given in Table 3.7 for three different pulse shaper configurations: XUV and soft X-ray applications at 5° and 3° grazing incidence, respectively.

The focus width of the monochromatic beams is affected by several ele-

XXPS Dispersion			
	Grating	**f**	**Spatial Color Separation $\Delta\lambda = 2‰$**
		[m]	[µm]
XUV	Custom	0.33	140
		2	840
Soft X-Rays 5°	250 l/mm	0.99	137
Soft X-Rays 3°	90 l/mm	1.65	140

Table 3.7: Dispersion for different shaper geometries.

ments: Gaussian waist size ω_y, geometrical optics effects blurring the image in the dispersion direction by Δy and of course surface quality of the optical elements. The Gaussian waist size is a function of the focusing distance and the wavelength, and it increases with increasing focal length f or wavelength λ. The contribution of geometrical effects can be studied with software like OpticStudio, and must be minimized through careful alignment of the optical elements. Poor surface flatness, slope errors and surface roughness can spoil performances and decrease spectral resolution. In Table 3.8 the contribution of the first two factors is shown for different wavelengths and optical elements. The grating maximum resolution $\frac{\lambda}{\Delta\lambda}$ gives the minimum

XXPS Resolution						
	Grating	**f**	λ	Δy_{min}	ω_y	Δy
		m	nm	µm	µm	µm
XUV	333 l/mm	0.33	266	3.7	1.2	2.8
			38	3.7	0.17	2.8
			15	3.7	0.66	2.8
		2	266	22	7.0	1.0
			38	22	1.0	1.0
			15	22	0.40	1.0
	2400 l/mm	0.33	38	0.51	0.17	2.8
	300 l/mm	0.33	266	4.1	1.2	2.1
Soft X-Rays 5°	250 l/mm	0.99	15	1.6	0.19	1.2
			4	1.6	0.050	1.2
Soft X-Rays 3°	90 l/mm	1.65	15	2.7	0.32	1.1
			4	2.7	0.084	1.1

Table 3.8: Contributions to the focus size in the Fourier plane. The minimum separation on the Fourier plane between two lines that can be resolved given the grating resolution is also listed. All numbers assume that a pulse with 5 mm diameter is used.

separation Δy_{min} of two lines that can be resolved. In the table, the separation of monochromatic beams in the Fourier plane at the resolution limit is shown. It can be seen that for the XUV and soft x-rays the Gaussian waist size is smaller than the effects due to geometrical aberrations, and usually negligible in comparison. The effects of geometrical aberrations are comparable to the theoretical resolution limit given by the grating. Two further aspects must be considered when looking at this data. First of all, the presence of surface imperfections will increase the focus size. Second, the size of the shaping mask elements, when greater than the focus size and separation of resolved lines, is the actual limiting factor to the spectral resolution of a pulse shaper.

3.2.4 Phase masks in the Fourier plane

Several kinds of reflective phase masks can be placed in the Fourier plane. In our experiments so far we have used a single lamellar-mirror. Further experiments with a pair of interleaved lamellar-mirrors are planned. Afterward an MMA will be commissioned to achieve arbitrary pulse shaping capabilities. The interleaved lamellar-mirrors we have developed and the MMA we plan to use are discussed in the following sections.

Interleaved lamellar-mirrors

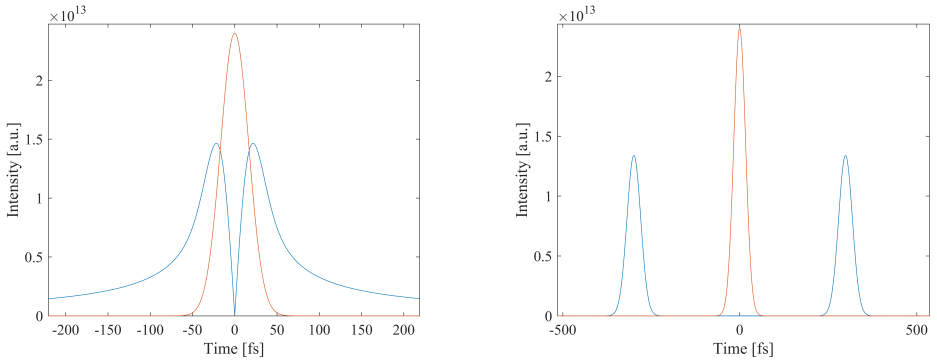

Figure 3.8: Comparison of the temporal shape of a double pulse generated with a split-mirror (a) and pair of interleaved lamellar-mirrors (b). The same unshaped pulse (orange) was used in both simulations. Details about the simulation code used can be found in Chapter 4.

A pair of interleaved lamellar-mirrors can be used in a pulse shaper to generate a double pulse, by introducing a periodic phase delay π along the Fourier plane. The resulting temporal separation is determined by the stripe period. The replicas separation is much increased compared to the use of a split-mirror design, as shown in Fig. 3.8.
In the current version of our interleaved mirrors, reflective stripes of 5 mm-long, 100 µm-wide polished silicon are separated by 150 µm-wide gaps. In the interleaved combination of two lamellar-mirrors, as shown in Figure 3.9, the top mirror is 1 mm thick, while the bottom mirror is 2.25 mm thick, with 1.25 mm-deep cuts between the stripes. The two mirrors have been machined using a diamond rotary saw by the group of Prof. Kip from the Helmut Schmidt University in Hamburg. Mirrors with smaller periodicity are under development. These would allow increased separation between the replicas. The shapes of the two mirrors fit together, with all stripes surfaces parallel on the same plane, maximizing the support for the stripes, in order to maximize the surface rigidity.
The flatness of the two 'twin' mirrors is crucial in order to introduce constant phase delays to the pulse spectral components along the footprint in the Fourier plane. The mechanical polishing procedure needed to produce surfaces with roughness below the nm level induces a permanent bend in the 1 mm-thick substrate of the top mirror. The current version of our mask

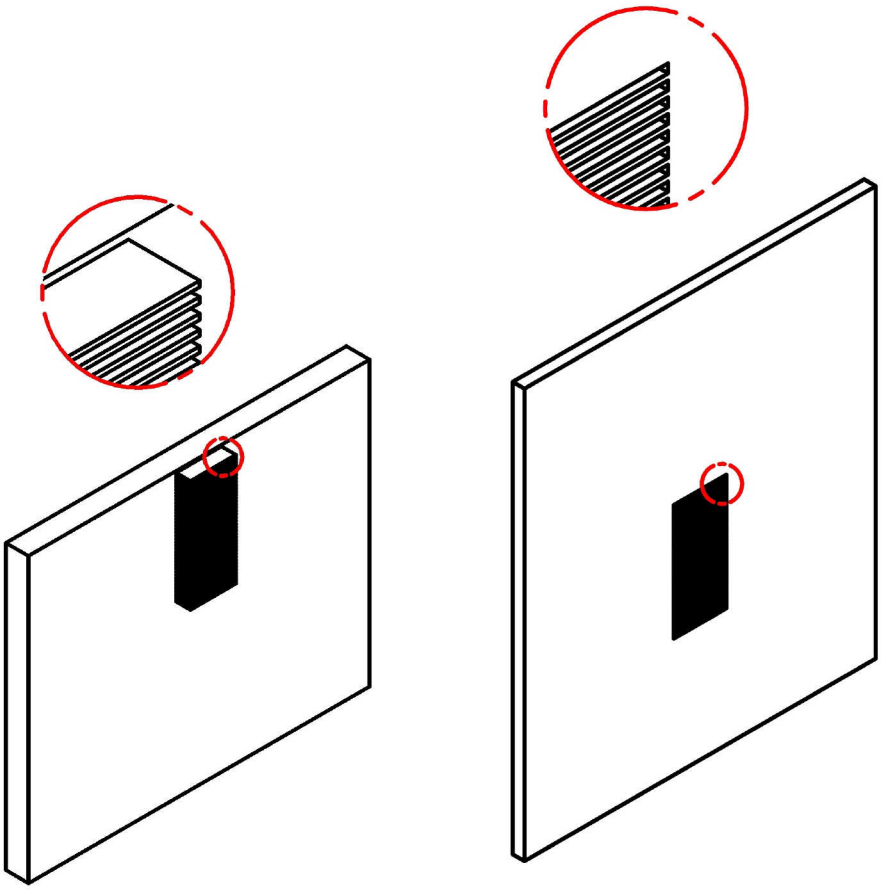

(a) (b)

Figure 3.9: Bottom (a) and top (b) interleaved lamellar-mirrors. The top mirror is made of about 5.2 mm-long reflective stripes connected at the sides to a frame. The bottom mirror is made of 5 mm-long stripes connected at the back to a support. The two mirrors fit one into the other, so that all the stripes can be on the same plane.

has shown sufficient surface flatness to measure fringe-resolved interferometric autocorrelation traces [68, 69]. However, the contrast that has been achieved yet is on a sub-10% level, due to surface bending. To improve its performances a thicker top mirror is currently under development.
A frame of Ce:YAG crystals, 0.2 mm thick has been glued on the frame of the top mirror around the striped part. Such crystals generate fluorescence yellow-green light at 530 nm when illuminated by short-wavelength light

below the UV spectral range due to strong absorption bands [70], making them a perfect candidate for use in the XXPS. Unpolished crystals were used because they scatter visible light, making the screens suitable for use with visible-light alignment lasers too. The Ce:YAG frame has a two-fold purpose: it helps in aligning the mask in the Fourier plane, while preventing part of the laser pulse from being reflected, un-shaped, from the outer frame of the top mirror.
A single lamellar-mirror can be effectively used in conjunction with a spectrometer as an alignment tool for the XXPS. It imprints a periodic structure on the wavelength spectrum by cutting away certain parts, while the effect can be diagnosed on the spectrometer. Thus, the phase mask position in the Fourier plane can be optimized resulting in the sharpest possible spectral structures.

Micro-Mirror Array

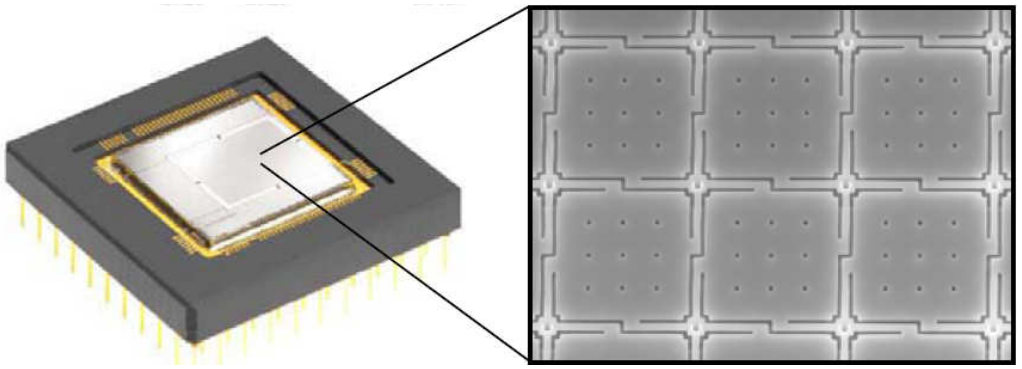

Figure 3.10: MMA from Fraunhofer Institute ISIT.

The use of an MMA is necessary to achieve arbitrary pulse shaping in the XXPS with high spectral and temporal resolution, respectively. It allows going beyond purely periodic spectral phase modulation towards full flexibility of the generated time-frequency spectrum. In addition, a 2D MMA allows tailoring of the spectral amplitudes. The mirrors on a row reflecting the same wavelengths can be delayed with respect to each other, in order to induce destructive interference between the reflected light. Thus, the intensity of the spectral components can also be modulated.
The MMA that we plan to use has 45 x 45 µm mirrors and 5 µm separation between them, with a surface of 192 x 128 pixels. It is a commercial device from the Fraunhofer Institute ISIT (see Fig. 3.10). The micro-mirrors are

made of aluminum, which has a reflectivity curve similar to that of silicon. Coating will be needed in order to cover the full XUV spectral range.

3.3 Optics Alignment

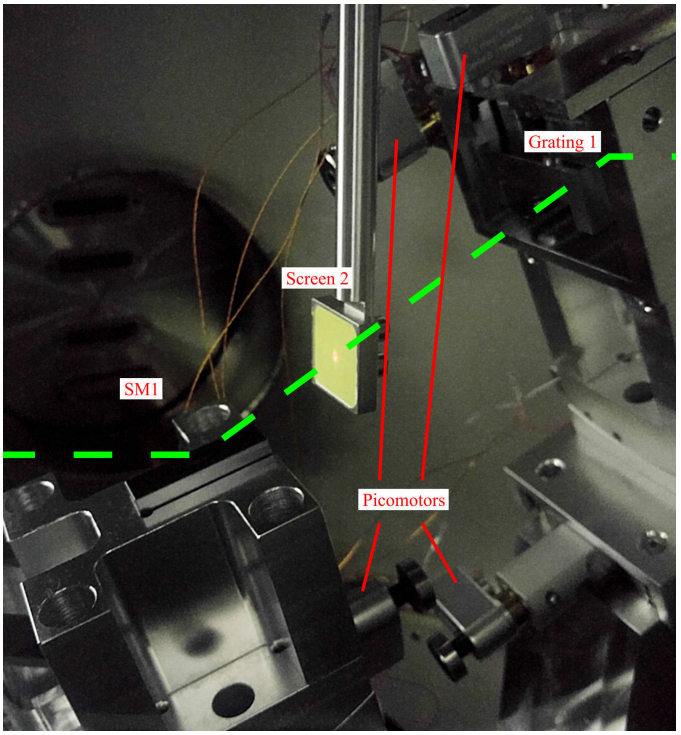

Figure 3.11: View of the inside of the first vacuum chamber of the XXPS. On the left the mirror SM1 is present, while on the right the first grating support is shown. A few of the picomotors that allow for in-vacuum alignment of the two optical components can be seen.

The precise positioning of the seven optical elements in the XXPS is crucial, in order to avoid introducing aberrations that would compromise the shaping performance. The parameter that needs to be adjusted over a long range is the focusing distance of the 4f geometry. It can be scanned to focus the pulse spectral components in the Fourier plane. To this purpose the distance between the five chambers of the XXPS can be adjusted coarsely using manual stages.
Detailed simulations making use of OpticStudio have been carried out in order to pinpoint critical degrees of freedom that needed to be remote-controlled using high-vacuum linear or goniometer stages equipped with

picomotors. The same applies to the fine alignment of the focusing distances. Most degrees of freedom are adjusted using commercially available stages, but several rotational degrees of the optical elements make use of custom stages, in order to combine compactness and high resolution. Picomotors from Newport with step size below 30 nm have been used. Currently 34 degrees of freedom are motorized, allowing for online in-vacuum adjustment (see Fig. 3.11).
The commissioning of the XXPS involves two pairs of commissioning stages, for a total of four stages. The first pair require optimizing the position of a single lamellar mirror using an high resolution spectrometer to investigate the cut bands. The second pair consists in using the two interleaved lamellar-mirrors to generate double pulses, then investigated with temporal diagnostics. The first and third stage make use exclusively of 266 nm fs pulses from the sFLASH seed laser, limiting the need of FEL pulses only to the second and fourth stages.
The XXPS alignment procedure is covered in detail in Appendix A.

3.4 Diagnostics

Four kinds of diagnostics have been developed to assist the beam alignment. Ce:YAG screens and CCD cameras are used to image the beam profile at various positions along the beam path through the shaper. An in-vacuum **w**hite **l**ight **i**nterferometry (**WLI**) setup has been developed to measure the introduced relative phase delay, i.e. beampath difference originating for the two interleaved lamellar-mirrors. Two spectrometers have been built to optimize the shaping mask position in the Fourier plane, one for 266 nm radiation and one for the XUV spectral range. Finally, a cross-correlator has been realized to characterize the temporal structure of the 266 nm seed pulses, while the THz streaking setup in the sFLASH experimental hutch developed by Azima et al. [42] will be used to characterize XUV pulses.

3.4.1 Ce:YAG screens

Eight retractable screens are present in the XXPS: one in front of each optical element, and one at the pulse shaper exit. The screens are covered with unpolished 0.2 mm-thick Ce:YAG crystals (see Section 3.2.4). In order to detect fluorescence or scattered light even at low intensity CCD cameras are used. The ACEa 1920g48 cameras from Basler in conjunction with CFFL F1.4 f25 mm lenses from Edmund optics have been utilized. The relevant

Ce:YAG Screens CCD Cameras & Lenses		
ACEa 1920g48	Pixel Size	5.86 x 5.86 µm
	Resolution	1920x1200
	Max FPS	42
	Quantum Eff.	70%
	Dark Noise	6.7 e^-
CFFL F1.4 f25 mm	Focal Length	25 mm
	Mag. at 100 mm	0.025 x
	Mag. at 400 mm	0.00625 x

Table 3.9: Ce:YAG screens cameras and lenses technical specifications.

specifications of cameras and lenses are listed in Table 3.9. The combination allows for a spatial resolution of 0.23-0.92 mm. Thus, sufficiently high alignment precision and sensitivity is achieved event at rather low photon numbers.

3.4.2 White light interferometry in vacuum

When shaping masks with two or more reflective surfaces are placed in the Fourier plane, like interleaved lamellar-mirrors or an MMA, the position of the moving elements must be known and set with high precision. The individual spectral phase delay (beampath length difference) that is introduced must be controlled with a precision of at least $\lambda/8$. Therefore, an in-vacuum WLI setup has been implemented to monitor the positions of the reflective elements in the Fourier plane. It is a Michleson interferometer, with a beam splitting cube and a reference mirror situated in vacuum close to the shaping mask, while the white light LED used as light source and the camera used to detect the interference pattern are placed outside of the central vacuum chamber. The reference mirror is mounted on a piezo stage to be moved as needed. The setup is shown in Figure 3.12.
The piezo motors used to position the shaping mask, e.g. the thin lamellar mirrors, are sensitive to vibrations from the environment and they themselves introduce vibrations due to voltage jitter. It follows that a scanned operation of the WLI setup returns only an average position of the elements, while shot-to-shot diagnostics are needed for good accuracy. The two reflecting surfaces of the interleaved lamellar-mirror assembly can be monitored in real time by tilting the two mirrors with respect to the reference surface and monitoring the position of the resulting interference fringes of the two elements. Such an arrangement has been already used success-

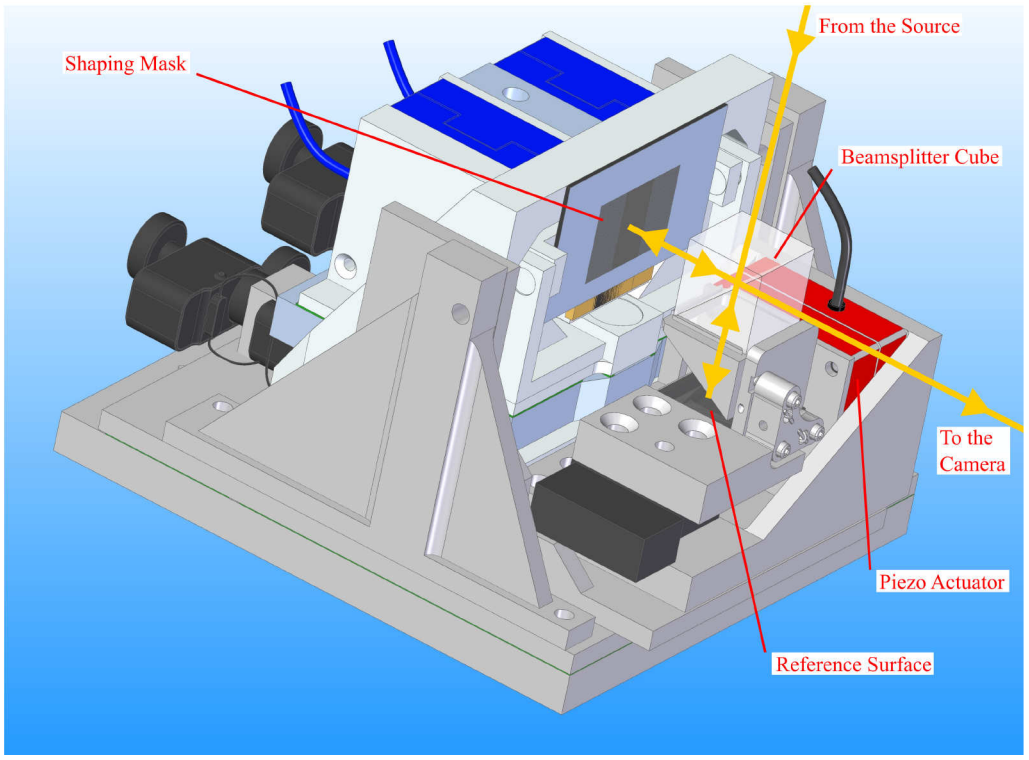

Figure 3.12: WLI setup in the XXPS in front of the interleaved lamellar-mirrors mount. The in-vacuum components of the WLI setup can be seen on the right. The path of the white light is shown in yellow.

fully in other experiments [71].
While such a scheme would work well for a 1D MMA, it cannot be applied in two dimensions. To obtain shot-to-shot position diagnostic on a 2D MMA an RGB CCD must be used in the WLI setup. The different wavelengths of the three colors generate interference patterns with inconstant phase relations between them. Measuring the values of two colors would allow univocal determination of the position of the moving element with respect to the reference surface (see Figure 3.13). The third color can be used to increase the accuracy of the measurement, reducing the probability of false position reconstructions due to noise. For a quantitative evaluation of the performances of the device, prototypes will need to be developed and tested.
Currently, the resolution of the monochromatic WLI setup is about 1 nm, which is sufficient for XUV applications. For the soft x-ray implementation of the XXPS the WLI setup will need to be improved, e.g. by switching to a pellicle beamsplitter, which introduces less distortion to the white light

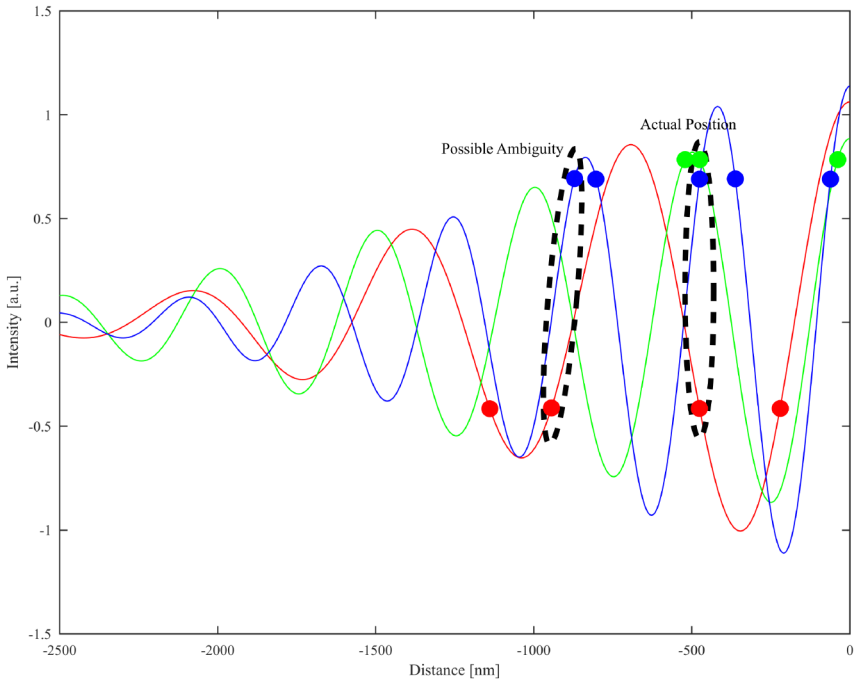

Figure 3.13: The period of red, blue and green components of the white light temporal interference is compared. Knowing the values of two or more of the components the position on the plot can be determined univocally, despite the trace covering several periods of each wavelength. Due to the presence of noise in real-world measurements, the use of only two colors to identify the position, e.g. red and blue, can lead to ambiguities. The use of all three colors constitutes a much more robust approach.

wavefront compared to a beam splitter cube, due to its thinness. More details about the setup and how its performance was characterized can be found in [69].

3.4.3 High-resolution XUV spectrometer

The key component of the spectrometer is a 001-0640 variable line-spacing concave grating from Hitachi. The spectrometer is shown in Fig. 3.14. The grating images the entrance slit of the spectrometer onto the spectral plane, where light in the 11-62 nm wavelength range is dispersed by the variable lines of the grating. The technical details of the grating are listed in Table

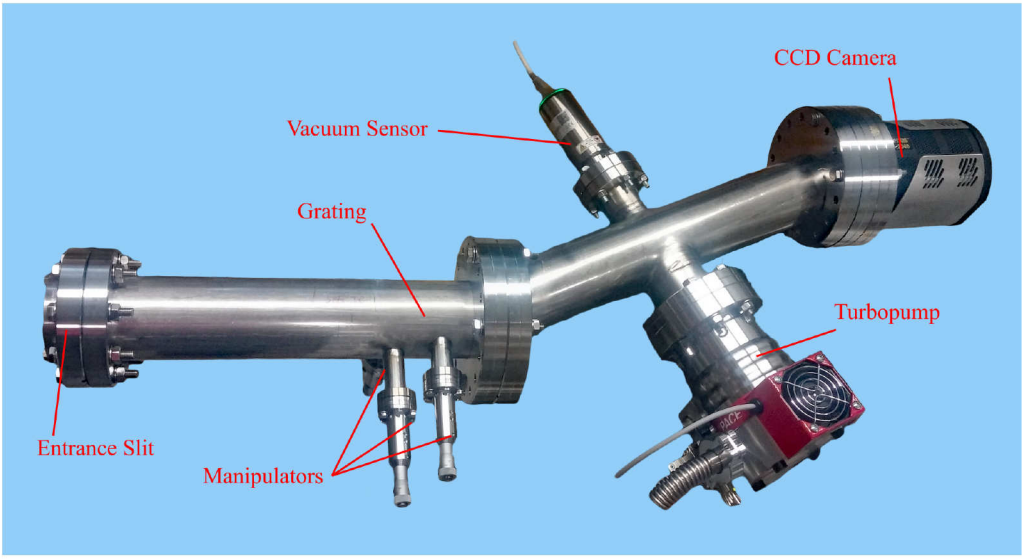

Figure 3.14: Side view of the high-resolution XUV spectrometer. The CF40 flange on the left side is removed to connect it to the vacuum. The optional vacuum cube where the focusing mirror is located is not shown.

Hitachi 001-0640	
Lines/mm	1 200
Curvature Radius	5649 mm
Size H x W x T	30x50x10 mm
Blaze angle	3.7°
Incidence angle	4.7°
Flat-Field Wavelength Range	11-62 nm
Flat-Field Dispersion Angles	10.44-22.74°
Entrance Slit Distance	350 mm
Flat-Field Plane Distance	469 mm
Coating	Au

Table 3.10: Technical specifications of the Hitachi 001-0640 grating used in the XUV spectrometer.

3.10.

The slit width is 12.5 µm and the images are taken with a 2048XO PIXIS camera from Princeton Instruments with 13.5 x13.5 µm pixels. The unprotected CCD sensor of the camera has a quantum efficiency in the XUV of up to 80% and can be cooled down to -70° °C to suppress thermal noise. The relevant technical specifications of the camera are listed in Table 3.11.

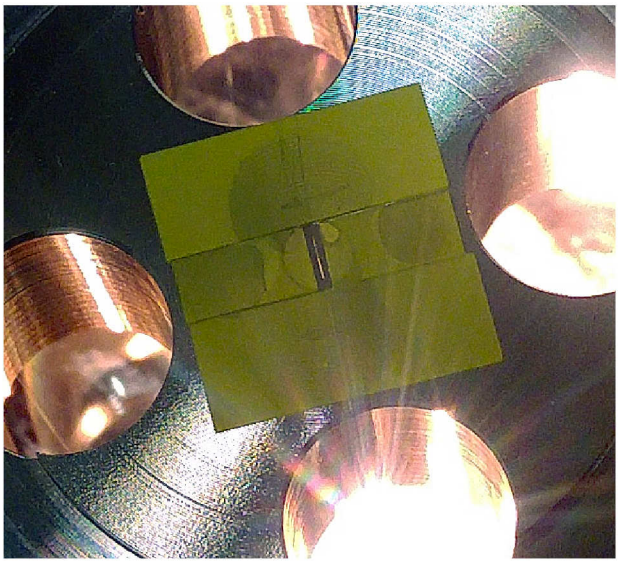

Figure 3.15: Ce:YAG crystals placed around the spectrometer entrance slit for alignment.

2048XO PIXIS	
Pixel Size	13.5 x 13.5 µm
Resolution	2048x2048
Max FPS	10
Quantum Eff. XUV	80%
Dark Noise	0.002 e^- at -60° °C
Min. Cooling Temp.	-70° °C

Table 3.11: Technical specifications of the 2048XO PIXIS camera from Princeton Instruments used in the XUV spectrometer.

The XUV spectrometer has been designed to operate between 28 and 40 nm, covering the spectrum between the 7th (38.1 nm) and the 9th (29.7 nm) harmonics of the 266 nm seed laser at sFLASH (see Chapter 1). Currently, the camera is mounted in fixed position with respect to the grating. However, the addition of a manipulator would allow to access the full flat-field range of the grating between 11 and 62 nm if required in future.
The overall length of the spectrometer is about 1 m. Due to space constrains in the sFLASH laboratory the spectrometer is operated together with a spherical multilayer mirror in front of the entrance slit bending the beam by 90°. The mirror has a curvature radius of 500 mm. It is placed at a distance of 137 mm from the slit. According to simulations of the

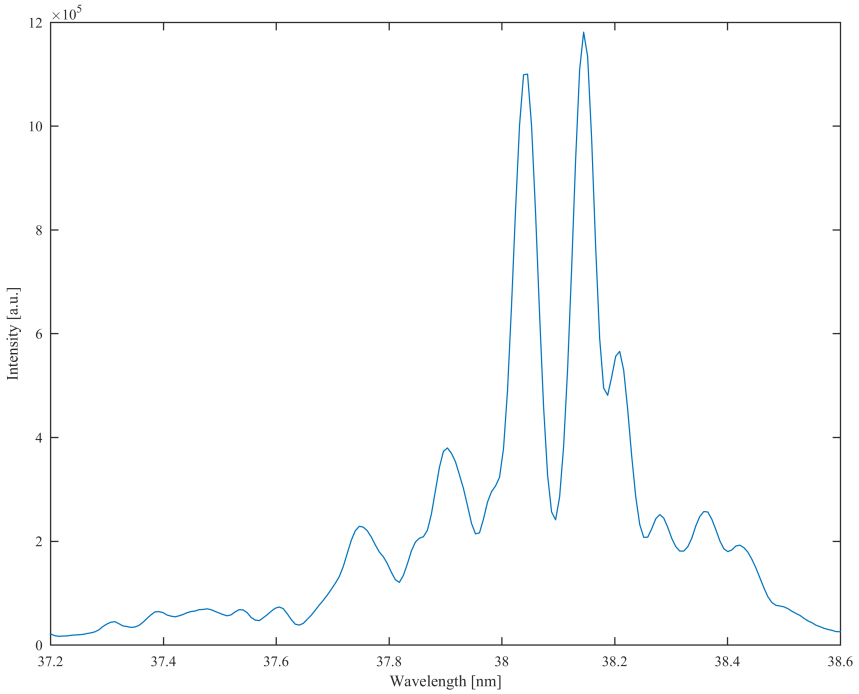

Figure 3.16: Detail of single spikes in a 38.1 µm SASE pulse at sFLASH.

whole spectrometer setup using OpticStudio, the beam should be focused down to a diameter of 6 µm in the entrance slit plane, while being imaged 1:1 onto the spectrometer CCD camera in the orthogonal (non-dispersive) plane. We note in passing that the simulations assume a 2 mm perfectly collinear seeded beam neglecting divergence. The multilayer mirror has a maximum reflectivity of 39% at 37.5 nm, and above 20% in the total 33.5-39.5 nm range. The spectrometer entrance slit is surrounded by Ce:YAG unpolished crystals, with a Basler ACEa 1920g48 looking at it, enabling its alignment (see Figure 3.15).
The grating is mounted on a compact custom-made 3-angle goniometer mount. Micrometer screws with vacuum feedthroughs are used to optimize the grating position during operation and to change the incidence angle on the grating, in order to pre-align the spectrometer using both, the 0th order and a visible pilot laser from the beamline. The design is complemented by a cold cathode ultra-high vacuum sensor and an 80 l turbopump.
The theoretical resolution of the grating in the present setup is $\lambda/\Delta\lambda = 43000$. The actual resolution of the spectrometer is limited by the 13.5 µm

CCD camera pixel size, which is only marginally bigger than the 12.5 µm entrance slit width. The dispersion is 0.0071 nm/pixel at 38 nm, corresponding to a resolution of $\lambda/\Delta\lambda = 5300$. The resolution can be seen in Figure 3.16, where the different lasing modes of a 38.1 nm SASE pulse at sFLASH are shown (seed laser off).
During the first phases of the XUV commissioning of the XXPS the transmission of the spectrometer was characterized. The measured transmission through the slit was only 4.6%, with a beam rms width on the slit of (108 ± 6) µm. While this value is sufficient for our foreseen applications, attempts at improving the focus size and position will be undertaken, in order to improve transmission and avoid blurring due to diffraction from the slit sides (no diffraction pattern was visible on the camera during 0th order tests of the spectrometer). The transmission of the spectrometer components is listed in Table 3.12. The mirror reflectivity and slit transmission have been measured experimentally, while for the grating and camera values provided by the manufacturers have been used.

Element	**Transmission**
Focusing Mirror	35%
Slit	4.6%
Grating	17%
Camera quantum efficiency	70%
Total	0.19%

Table 3.12: Estimated XUV spectrometer detection efficiency, including the optional focusing-mirror.

3.4.4 Compact high-resolution UV spectrometer

The spectrometer, based on the Wadsworth layout [72], is designed to operate between 210 and 350 nm. It has been built for proof-of principle shaping experiments making use of 266 nm seed pulses. The spectrometer mounting is shown in Figure 3.17.
The spectrometer is based on a A374048 grating from Richardson Gratings. It is a concave, constant line-spacing, blazed grating. The relevant technical specifications are listed in Table 3.13.
The laser pulse is aligned into the spectrometer and to the center of the grating with the help of two irises. While the iris closer to the gratings needs to be fully open for operating the spectrometer, the first one can be used to limit the amount of light entering the device. The light is dispersed by the

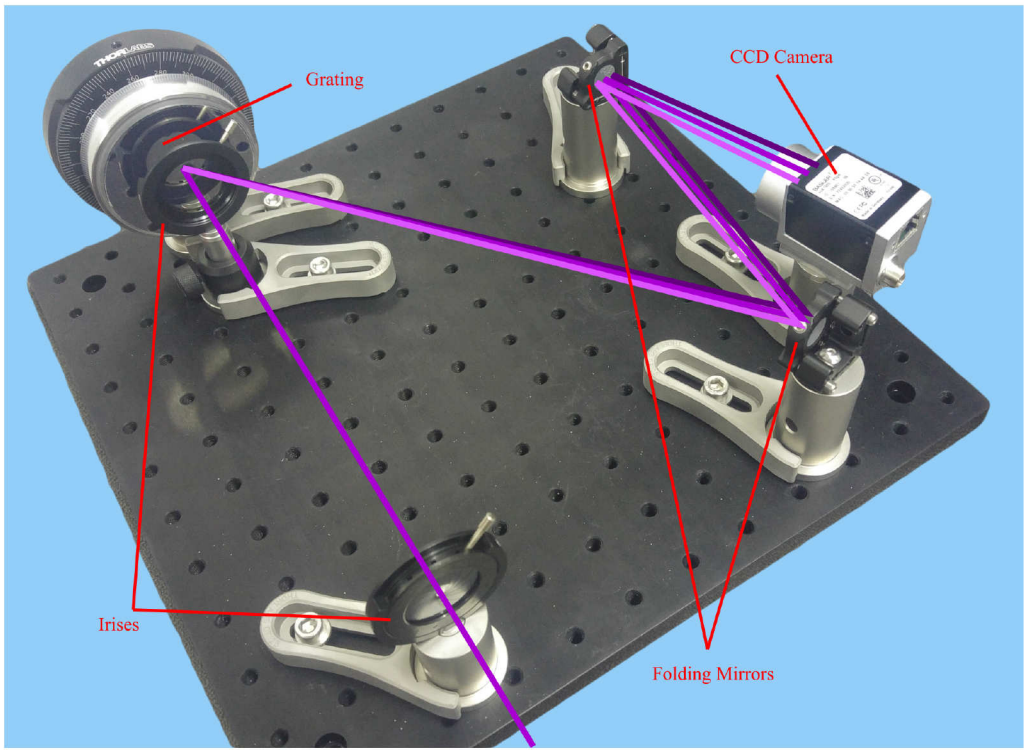

Figure 3.17: Compact high-resolution UV spectrometer layout. The beam-path is shown in purple.

Richardson Gratings A374048	
Lines/mm	2 160
Curvature Radius	998.8 mm
Diameter	63.5 mm
Thickness	12 mm
Wavelength Range	210-350 nm
Coating	Aluminium

Table 3.13: Technical specifications of the A374048 grating from Richardson Gratings used in the UV spectrometer.

grating mainly to one of the first orders, due to the blazing of the grooves. Two flat mirrors with UV-enhanced aluminum coating fold the dispersed beam and help to align it to the Basler camera, identical to the ones used to look at the XXPS screens (technical specifications can be found in Table 3.9). The theoretical resolution of the grating assuming a collinear beam of 5 mm diameter is $\lambda/\Delta\lambda = 10800$. The actual resolution is limited by the

focus size of 13 µm (estimated through an OpticStudio simulation), which is greater than the 5.86 µm pixel size. The dispersion is 0.0046 nm/pixel at 266 nm. A typical spectrum generated by the home-built frequency tripler can be seen in Figure 3.18.

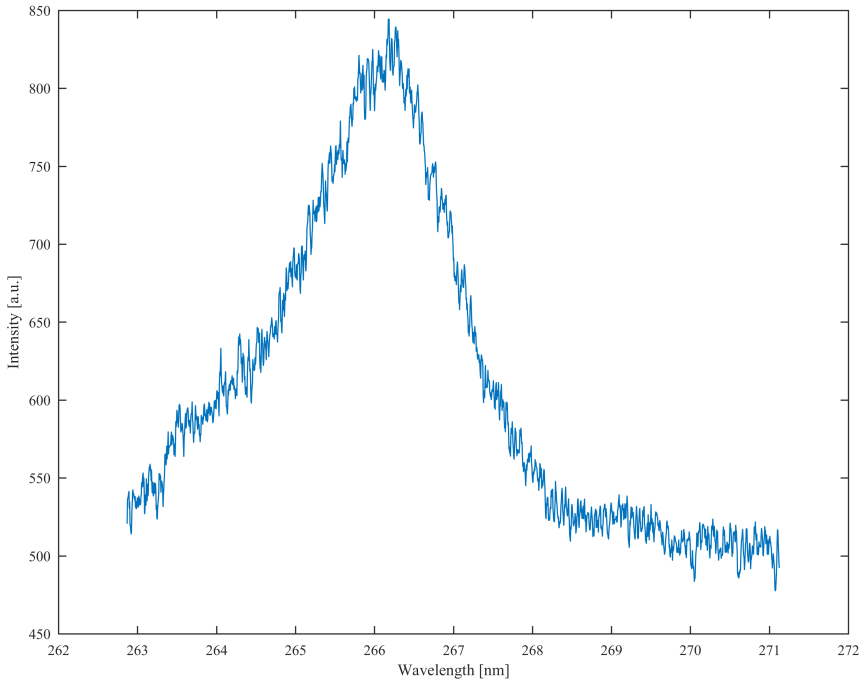

Figure 3.18: Spectrum of the 266 nm light generated by the tripler in the sFLASH experimental hutch.

3.4.5 UV-IR cross-correlator

Second order autocorrelation is a widely used technique for temporal characterization of IR and visible laser pulses. The process most commonly used is second harmonic generation in a nonlinear crystal. The investigated pulse is split into two parts, which are then overlapped in a birefringent crystal. With the correct angle between the replicas and the crystalline reticule, first and second harmonic speeds in the crystal are matched, resulting in energy transfer from the first to the second harmonic mediated by the reticule typically referred to as 'phase matching'. By varying the delay between the two replicas, constructive and destructive interference leads to modu-

lation of the second harmonic intensity. By scanning the delay between the two pulses a second order autocorrelation trace is obtained, containing information about the pulse length and temporal profile. Although such a trace does not allow a full characterization of the pulse, e.g. the sign of the chirp cannot be extracted because the trace is symmetrical, the pulse time duration can be precisely extracted from the trace. An introduction to nonlinear optics can be found in books like e.g. [73] and it is beyond the scope of this thesis.
Second harmonic generation cannot be used to characterize the temporal profile of the 266 nm pulses, because no birefringent crystal transparent at 133 nm exists. Thus, a different second order wave-mixing process must be used. An effective alternative to second-order autocorrelation is cross-correlating the 'unknown' pulse with a reference pulse at longer wavelength. The nonlinear process called **d**ifference **f**requency **g**eneration (**DFG**) provides photons with energy equal to the difference. As 800 nm pulses are readily available, because they are used to generate the 266 nm light, the obvious solution is to use them for the cross-correlation. The result is the generation of 400 nm light, i.e. the second harmonic of 800 nm.
The layout of the cross-correlator developed by the author, together with Bastian Manschwetus and Xeumei Cheng from the DESY laser group (FS-LA), is shown in Figure 3.19. The main components are numbered. The collimated 266 nm beam is aligned into the cross-correlator with the help of two irises (1 and 2). The 800 nm beam can be inserted collinearly to the UV. In this case the 266 nm pulses are separated from the 800 nm beam by a dichroic beamsplitter (3). The UV beam is then sent to an adjustable delay stage (4) and afterwards reflected from two plane alignment mirrors (5 and 6). The IR, if inserted collinerar to the UV, is bent back 180 ° (7), otherwise it is coupled in by a flip mirror (8). In the latter case a beam dump screen is inserted to block light transmitted by the beam splitter. The IR is sent to another plane alignment mirror (9). Finally, both 266 nm and 800 nm beams are focused onto the non-linear β-BBO crystal (11) by a cylindrical mirror (10). The focusing mirror is hit by the two beams at different position along the central axis of curvature, in order to overlap them in the non-linear crystal at 5 ° angle. The 400 nm generated in the DFG process is sent to a CCD camera (12). A second cylindrical mirror (13) can be used to collimate the beam before sending it to the camera.
Due to the difference in angle between the two beams in the β-BBO crystal, different parts of the beam interact with each other at different times. Assuming a uniform wavefront for both beams, the generated second harmonic maps different pulse delays along the horizontal axis of the CCD, resulting in an intensity distribution that is similar to a time-scanned second order

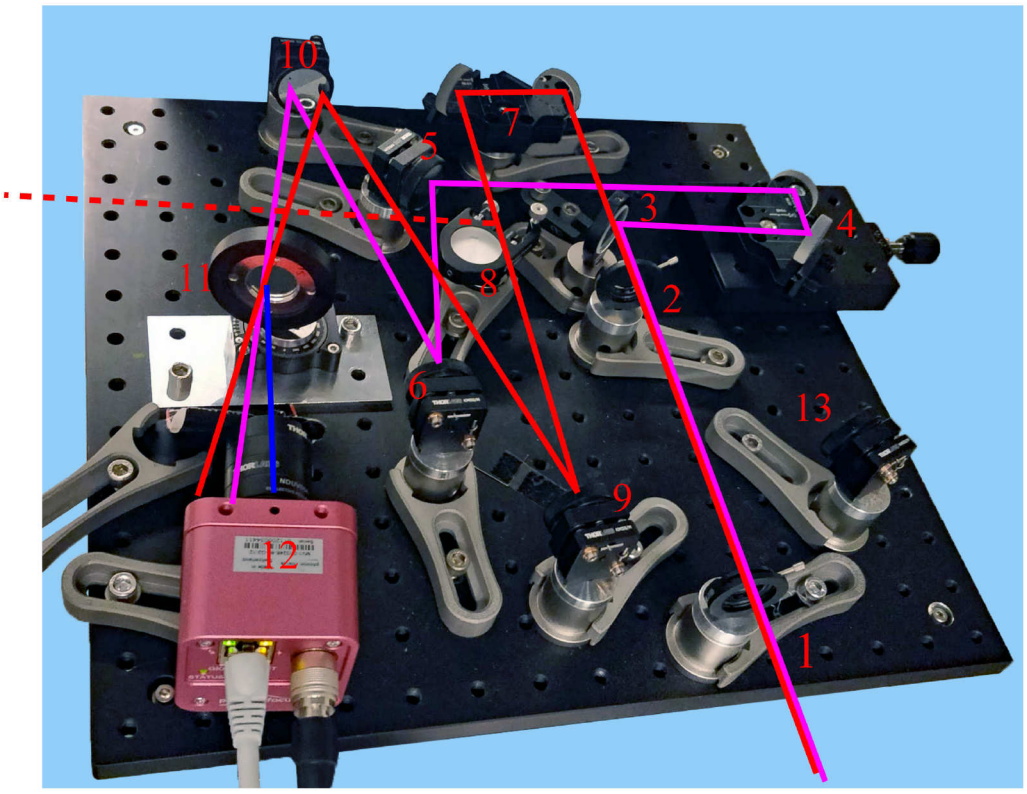

Figure 3.19: Cross-correlator layout.

auto-correlation function. Knowing the time duration Δt_{800} of the reference 800 nm, the time duration of the 266 nm pulse can be derived according to:

$$\Delta t_{267} = \sqrt{(\Delta t_{cross})^2 - (\Delta t_{800})^2} \tag{3.2}$$

where Δt_{cross} is the 400 nm cross-correlation signal.
With the typical 20-30 fs time duration of the reference pulses being much shorter than the expected 130 fs time-duration of the 266 nm pulses generated by the tripler, tailored UV pulse shapes in time domain can be characterized in great detail. Thus, a cross-correlator is an optimal diagnostic tool for double pulses generated by the XXPS in proof-of-principle experiments.
A copy of the cross-correlator has been built to measure the time duration of the UV seed beam at sFLASH. A measured cross-correlator trace of the seed UV beam is shown in Figure 3.20.

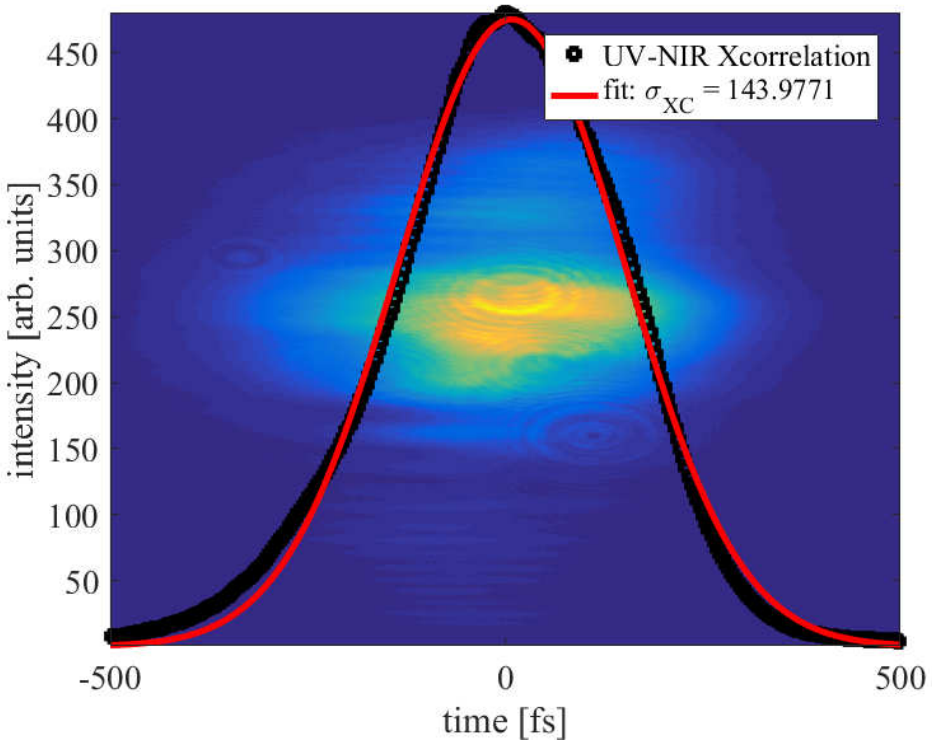

Figure 3.20: Cross-correlation signal from an sFLASH seed pulse probed with a $\sim 28\,fs$ *long 800 nm pulse. The derived duration of the 266 nm pulse is* $\sim 140\,fs$*. Picture courtesy of Xuemei Cheng and Bastian Manschwetus.*

3.5 FEL Transport Beamline

A vacuum beam-transport line has been built to transport the sFLASH FEL pulses from the M2 mirror in the experimental hutch to the XXPS entrance. The transport line has been designed in order to facilitate the alignment and operation of the XXPS.
The layout of the transport line is shown in Figure 3.21. When reflecting light toward the XXPS, the angle of incidence of the FEL radiation on M2 is 2.5° due to the design of the experimental hutch infrastructure. Currently the length of M2 is only 50 mm, resulting in a maximum width of the reflected beam of 2.18 mm. Because of the 25 m distance between the sFLASH radiator exit and the M2 mirror, the diameter fwhm of the FEL beam when hitting the mirror is much larger than 2.18 mm, resulting in power loss. In order to simplify the alignment of the XXPS, after M2 a pair of 2 mm apertures are located. The apertures have two purposes:

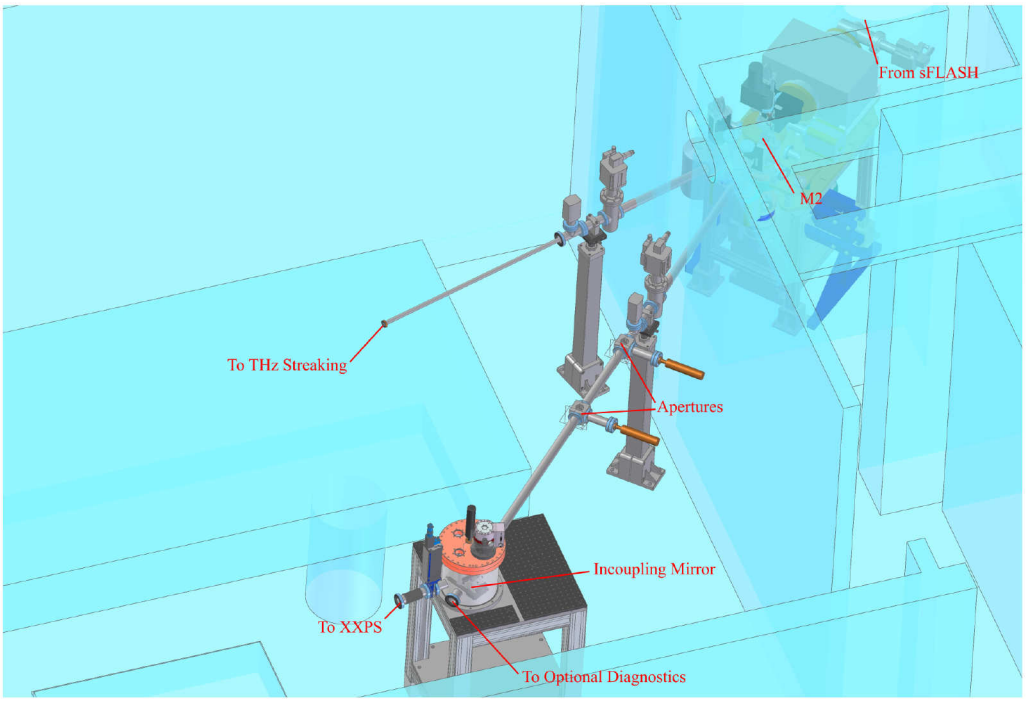

Figure 3.21: FEL transport beamline to the XXPS entrance in the sFLASH experimental hutch.

they provide a fixed reference to which the FEL path can be reproducibly aligned, and they cut a circular 2 mm profile out of the part of the beam that is reflected by M2. The apertures can be removed, allowing for maximum energy transmission once the XXPS alignment is completed (although with the current Richardson Gratings the improvement is limited, due to the 2 mm acceptance along the y-axis). The side of the apertures facing the FEL beam is coated with Ce:YAG powder, allowing operation with both alignment laser and FEL. The two apertures are separated by 0.6 m.
Behind the apertures the beam is aligned into the XXPS by the incoupling mirror. For XUV applications a carbon-coated mirror with 0.5 nm rms surface roughness is used. With 50x20 mm reflecting surface, the mirror is operated at 17.5° grazing incidence. Such an angle has been chosen due to the space constraints in the sFLASH experimental hutch. The incoupling mirror can be operated under vacuum, with two picomotors for angle alignment and a step motor to allow for the reproducible extraction and insertion of the mirror. When in the retracted position, the FEL light reaches an exit flange, where diagnostics instruments like spectrometers can be mounted. Two Ce:YAG screens are located before the incoupling mirror and before

the XXPS entrance respectively, in order to assist during alignment.

3.6 Experimental Characterization of XUV Transmission

Since the first tests with 38 nm the transmission of the off-the-shelf 38 nm gratings from Richardson Gratings has proven to be extremely low. In order to make alignment possible, some upgrades had to be implemented in the XXPS, including the cameras used to see the beam profile on the Ce:YAG screens. SASE pulse trains of up to 346 bunches have been used to increase the amount of light going through the pulse shaper, in order to make alignment easier. While SASE does not reach saturation in the short sFLASH radiator, the high number of pulses compensates for the small yield, generating much higher energy per bunch train. During the last experiment, trains of 346 bunches with (2.7 ± 2.2) µJ energy per pulse were used, corresponding to an average energy per pulse train of 930 µJ, more than ten times higher than the up to (35 ± 10) µJ energy measured for sFLASH seeded pulses [37]. With the current seed laser, trains of seeded pulses are not possible, as discussed in Chapter 1. While due to the phase discontinuities in the SASE pulses no actual pulse shaping can be performed with it, SASE pulse trains can be used to see with the high-resolution XUV spectrometer the spectral bands transmitted by a single lamellar-mirror. The data used in the following paragraphs were all obtained exclusively using SASE pulses.
While the transmission of the mirrors and shaping mask in the XXPS can be calculated using data from literature, the transmission of the gratings can be estimated using the 0th order and 1st order data measured with the spectrometer. For the 0th order, using 10 s exposure time and 1 bunch per bunch train, after background subtraction $(2.36 \pm 0.09) \cdot 10^8$ photons have been detected on average in 20 exposures. For the 1st order, still using a 10 second exposure time, but bunch trains with 346 bunches each, $(5.24 \pm 0.29) \cdot 10^7$ photons have been detected on average in 20 exposures. This corresponds to a decrease in transmission by a factor of 1600. To calculate the transmission of the gratings at the 1st order, it is first necessary to estimate the transmission of the gratings at the 0th order. The effect of the grating lines on transmission can be roughly approximated as an increase in surface roughness, as shown in Figure 3.22. The gratings used are replicas of ruled gratings. The lines of ruled blazed gratings are shaped as right angled triangles, with the 90° angle facing away from the grating

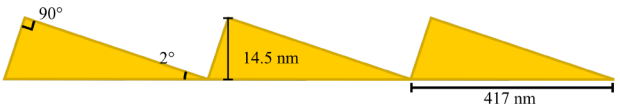

Figure 3.22: Shape of the blazed lines of the XUV grating from Richardson Gratings.

surface and the hypotenuse parallel to it. With 2400 lines/mm and 2° blaze angle, the triangle height with respect to the hypotenuse is 14.5 nm. Due to the triangular shape of the lines, the surface height (neglecting for the moment the surface imperfections) will be uniformly distributed between -7.25 and 7.25 nm from the average, with 4.2 nm standard deviation. Such a value must be added quadratically to the rms roughness of the grating, in order to obtain an estimate of the overall roughness. Richardson Gratings does not provide a value for the surface roughness of their gratings, therefore a reasonable value of 3 nm rms was used, which is an estimate of the surface roughness of the final custom gratings provided by the company that will manufacture them. Adding the two values quadratically, a surface roughness of 5.4 nm rms is obtained. Using the fact that the grating is gold coated, the expected reflectivity at 38 nm calculated as in Section 3.12 is 46% for a single grating. The effect of the surface roughness previously calculated on the grating transmission estimation is limited. Assuming 50% less surface roughness, the reflectivity of the grating would be 59%, while it would be 29% assuming 50% more surface roughness. Assuming equal transmission for the two gratings in the XXPS configuration (where one is operated at the 1st order and the other at the -1st order), the estimated transmission of each grating is approximately 1.1%.
The transmission of the gratings can be compared to the transmission or detection efficiency of the remaining elements of the XXPS during the experiment, in order to determine the main elements reducing light transmission. The estimated values can be further used to calculate the transmission of the sFLASH extraction line when a 2 mm aperture is used. These estimates will help in planning further experiments with the XXPS.
The transmission or detection efficiency of all the optical components in the XXPS, together with the transmission of the incoupling mirror are listed in Table 3.14. The transmission of the incoupling mirror and of all the XXPS elements but for the gratings has been calculated as in Section 3.12. A single lamellar-mirror was placed in the Fourier plane, therefore the mask occupancy was only 40%. Using these values, and the high-resolution spectrometer transmission, the transmission from the FEL to the incoupling

38.1 nm Transmission			
Element	**Transmission**	**Single SASE Pulse Output**	
		Photons	Energy
FEL exit		$5.2 \cdot 10^{11}$	2.7 µJ
Beamline & Apertures	16%	$8.4 \cdot 10^{10}$	440 nJ
Incoupling Mirror	53%	$4.4 \cdot 10^{10}$	230 nJ
SM1	86%		
SM2	90%		
Grating 1	1.1%		
Lamellar Mirror	36%		
Grating 2	1.1%		
SM3	72%		
SM4	75%		
XXPS Total	0.0018%	$8.0 \cdot 10^{6}$	42 pJ

Table 3.14: Transmission of beamline and XXPS components. The total transmission of the XXPS is also listed, together with the amount of energy and photons per pulse that were transmitted by the beamline, incoupling mirror and pulse shaper during the experiment.

mirror can be estimated as 16%. From what has been seen during alignment, most of the power loss is expected to be due to the parts of the FEL beam profiles cut by the M2 mirror size and the 2 mm apertures.
The data in the table shows what the causes of the system low transmission are. The main contributors are the two off-the-shelf gratings and the 2 mm apertures and M2 mirror cutting the FEL profile. The custom gratings are expected to highly improve on the transmission of the predecessors, due to the tailored blaze angle. To make full use of their 5 mm acceptance along the y-axis, 5 mm apertures and a new 120 mm-long M2 mirror will be needed. Such improvements are expected to increase transmission by approximately three orders of magnitude.

Chapter 4

Early Commissioning with Ti:Sa at 266 nm and FEL at 38 nm

The initial study was performed using using 266 nm femtosecond pulses generated by nonlinear frequency up-conversion of the 800 nm pulses provided by the sFLASH seed laser. The light generation setup is described in Section 4.1. A proof-of-principle pulse shaping experiment has been performed placing a single lamellar mirror in the Fourier plane. The spectrum transmitted by the reflecting stripes was characterized using the high-resolution UV spectrometer. The recorded contrast in the spectral distribution allows for the correct alignment of the shaping mask modulating the spectral amplitudes. The results of the measurements are presented and compared to simulations in Section 4.2.
First steps towards tailoring 38.1 nm XUV laser light generated by sFLASH have been carried out. A first FEL pulse shaping experiment within the XUV spectral range and again with a single lamellar mirror placed in the Fourier plane was attempted and the status is reported in Section 4.3.

4.1 Generation of 266 nm fs Pulses

The UV generation process in the sFLASH experimental hutch starts with uncompressed 800 nm pulses, 64 ps-long generated by the Ti:Sa seed laser. A sketch of the light generation setup is shown in Figure 4.1. A 4-pass grating compressor reduces the pulse duration down to the fs range. An IR telescope downstream of the compressor reduces the beam diameter by a factor of 2.66, from 13 mm to about 5 mm fwhm. The beam is then sent into

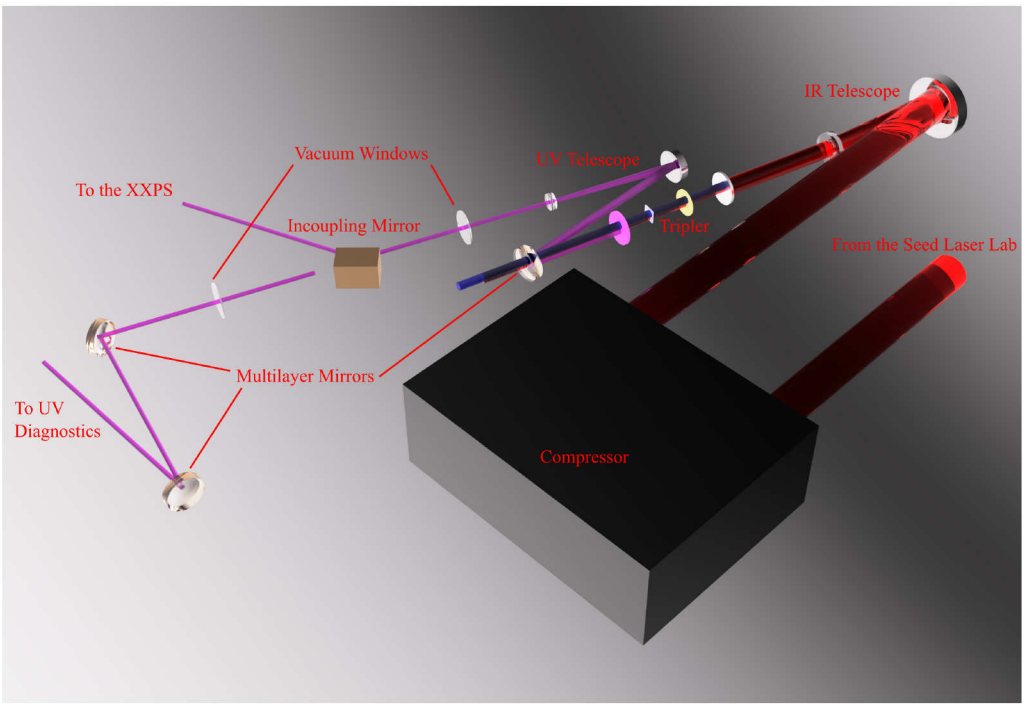

Figure 4.1: UV generation setup in the sFLASH experimental hutch.

a tripler, which generates the third harmonic of the seed laser at 266 nm. Behind the tripler a bandpass mirror filters most of the residual 800 nm and 400 nm radiation, in order to protect the UV optics from damage. We note in passing that the remaining non-UV light is removed by the first grating of the shaper. Behind the mirror a second telescope is used to collimate the UV beam and to demagnify the diameter by a factor of 2, in order to generate a beam diameter well below the 5 mm limit given by the acceptance of the shaper optics. Behind the telescope the UV beam enters into a vacuum chamber through a fused-silica window, where a retractable plane UV-enhanced aluminium-coated mirror is used to deflect the beam towards the entrance of the XXPS. This mirror is placed in the same holder of the incoupling mirror used for FEL applications. The angle of incidence on the mirror is again 17.5°. The setup allows for the insertion of the 266 nm pulses collinearly to the FEL light. The window is removed during FEL operation and the vacuum chamber is connected to the FEL beamline. Alternatively, the incoupling mirror can be retracted, allowing the UV light to exit the vacuum chamber through a second fused silica window. The beam is then reflected by a further pair of UV bandpass mirrors, in order to filter out remaining 800 nm and 400 nm contributions before power or spectral char-

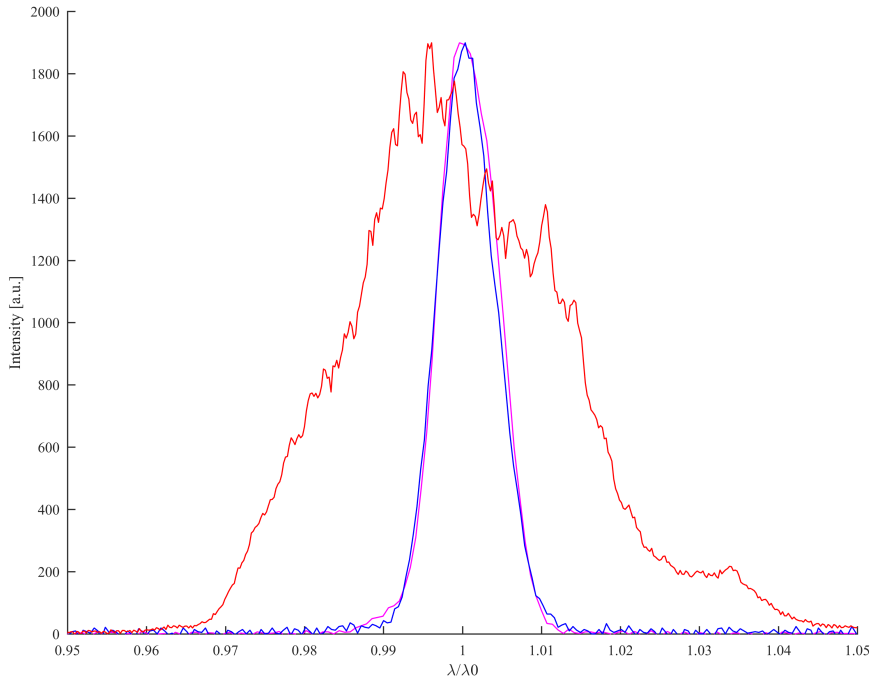

Figure 4.2: Spectra of 266 nm (purple), 400 nm (blue) and 800 nm (red) pulses after two 262-267 nm bandpass mirrors during the early stages of the tripler commissioning.

acterization of the unshaped femtosecond UV pulse.
The two telescopes in the setup are built using a Galilean layout, in order to avoid focusing the intense pulses in air, thus destroying the beam profile due to self-focusing[1]. The telescopes consist of a focusing mirror and a de-focusing lens. Such a layout is used to keep the UV generation setup as compact as possible. The mirrors are spherical and reflect the beam at nearly normal incidence. No aberrations introduced by this arrangement have been detected. The mirror used in the IR telescope is coated with protected silver while the one in the 266 nm telescope is coated with UV-enhanced aluminum. The telescope lenses are plano-concave spherical lenses, made of BK-7 (IR) and fused silica (UV) and coated with anti-

[1]Self-focusing is a non-linear process, where a refractive index gradient is thermally induced by an high power laser in a medium. This results in focusing of the central part of the laser wavefront, degrading the laser profile and possibly damaging the medium due to the increased peak power.

reflective coatings.
The frequency up-conversion setup for UV generation is based on a kit of crystals for 800 nm third harmonic generation from Eksma Optics. In the kit a calcite crystal is used to delay the IR pulse with respect to the 400 nm radiation after the first β-BBO, instead of the α-BBO crystal used in sFLASH triplers (see Chapter 1). It is designed to generate pulses of about 130 fs length fwhm, with a first β-BBO crystal of 0.5 mm thickness, and a second of 0.15 mm. The diameter of the BBO crystals is 6 mm. During tripler commissioning and the UV pulse shaping experiments the IR beam had an energy of (1.74 ± 0.13) mJ, which is about a factor of two below the damage threshold of the tripler waveplate. The spectra of the 266 nm, 400 nm and 800 nm pulses after removing the last of the bandpass mirrors are shown in Figure 4.2. The measurement has been performed using a SPM-00X spectrometer from Photon Control Inc., with an 2 m-long UV incoupling fiber from Thorlabs with a diameter of 200 µm. The measured bandwidths are (3.5 ± 0.4)% fwhm for the IR, at (796 ± 2) nm central wavelength, (1.1 ± 0.4)% for the 400 nm at (397 ± 1) nm central wavelength and (1.0 ± 1.1)% for the 266 nm pulse at (266 ± 2) nm central wavelength. In a second set of measurements bandwidths between $(0.64 \pm 0.02\%)$ and $(1.30 \pm 0.02\%)$ have been recorded for the UV pulses using the home-built high-resolution spectrometer.
With this setup the maximum conversion efficiency achieved for the second harmonic has been 12%, instead of the 25% specified by the company. Consequently, the output power of (14 ± 3) µJ in the third harmonic gives less than 1% conversion efficiency, which is significantly below the 10% achieved in the frequency up-conversion process generating the sFLASH seed pulses. Currently, the thickness and diameter of the nonlinear crystals, in particular for the first β-BBO, are not optimized in order to increase the UV output. The crystal bandwidth is much smaller than that of the IR pulses, therefore only a part of the 800 nm spectrum contributes to the harmonic generation. This results in 400 nm and 266 nm pulses with limited energy and much smaller bandwidths than the IR pulses, as can be seen in Figure 4.2. However, the resulting UV pulse energy in the present setup is sufficient for the first proof-of-principle experiments tailoring femtosecond UV pulses by means of the developed all-reflective 4f device.
For the sake of completeness we note that the band-pass mirrors present in the UV generation setup are multilayer mirrors from Thorlabs, designed for high transmission at nearly normal incidence between 262 and 267 nm. Their reflectivity in that band is about 99% for incident angles between 0 and 45°. Their fused silica substrate is transparent to 800 nm and 400 nm light, allowing dumping of the IR and visible pulses on a screen without

risking damage to the mirror coating.

4.2 Tailoring the Time-Frequency Spectrum in the UV by Spectral Amplitude Modulation

A single lamellar mirror has been placed in the Fourier plane of the pulse shaper acting as an amplitude mask that imprints a modulation of the spectral amplitudes. This is due to the 100 µm-wide reflective stripes (uncoated silicon surface) and 150 µm gaps resulting in a 250 µm period, as described in Chapter 3. For the pilot UV experiment the corresponding 266 nm Richardson gratings have been mounted in the pulse shaper. While uncoated silicon substrates have been used for the mirrors SM1 and SM2 (see Chapter 3 and Figure 3.3), carbon coated versions were used for the remaining two cylindrical mirrors in the XXPS. The UV transmission through the pulse shaper during the experiment has been estimated to be on the order of 10^{-5}. Taking into account published UV reflectivity and transmission values of the optics [74, 75] it turns out that this is mainly limited by the low reflectivity of the amorphous carbon coated mirrors. One derives an average 0.7% reflectivity for each of the SM3 and SM4 mirrors by using the given specifications summarized in Table 4.1 together with measuring the pulse energy at the entrance of the XXPS and on the spectrometer camera.

266 nm Transmission	
Fused Silica Window	88%
Incoupling Mirror	98%
Si SM1	44%
Si SM2	95%
Interleaved Lamellar-Mirrors	76%
UV Gratings	70%
Spectrometer UV Grating	60%
Folding Mirrors	90%

Table 4.1: Transmission of the optical components in the transport line, XXPS and UV high-resolution spectrometer situated between the UV telescope and home-built spectrometer camera.

The home-built spectrometer characterizing the spectral distribution at the

pulse shaper exit was not absolutely calibrated before the experiment, therefore the central wavelength of the pulses has been cross-calibrated with the commercial SPM-00X spectrometer. The modulated spectrum is shown in Figure 4.3. Here, the accumulated spectra of 251 pulses are compared to simulations that describe mathematically the effects of the amplitude shaping mask acting on a Gaussian beam passing the 4f pulse-shaper setup. The equations on which the code is based have been developed by Thurston et al. in [51]. They leverage the fact that the shaped pulse can be written in Fourier transform as [76]:

$$\tilde{E}_{out}(\omega) = M(\omega)\,\tilde{E}_{in}(\omega) \tag{4.1}$$

where $\tilde{E}_{in}(\omega)$ is the Fourier transform of the input pulse electric field and $M(\omega)$ is a complex function describing the effects of the pulse shaper on the pulse. The inverse Fourier transform of the product is then used to obtain the temporal profile of the shaped pulse. The form of the function developed by Thurston et al. accounts for the mask shape, grating dispersion in the pulse shaper, finite focus size of each monochromatic spectral component and diffraction from the edges of the mask elements. They have been modified by the author of this thesis by replacing the linear approximation of the grating dispersion with the exact non-linear form:

$$y = f \cdot \left(\tan\left(\frac{\pi}{2} - \theta_{out}(\lambda)\right) - \tan\left(\frac{\pi}{2} - \theta_{out}(\lambda_0)\right)\right) \tag{4.2}$$

where y is the position along the dispersion axis on the Fourier Plane, with $y = 0$ being the center of the shaping mask, f is the focus length of the XXPS, θ_{out} is the grating diffraction angle and λ_0 is the central wavelength of the pulse. The diffraction angles are calculated using the grating equation.

We note that the experimental data from the spectrometer is compared to the simulated spectrum right behind the striped mirror in the pulse shaper although the spectral modulation was experimentally characterized at the shaper exit. The effects of the spectrometer response function and of misalignment in the second half of the XXPS have not been simulated.

A linearly chirped pulse with a Gaussian spectrum with the experimentally determined UV spectral bandwidth fwhm is taken as input for the simulation. Such a spectrum only approximately fits the measured data, which shows an asymmetric spectrum. The starting pulse used in the simulation is positively chirped and has 130 fs pulse duration fwhm. The time duration used is the expected one according to the specifications of the nonlinear

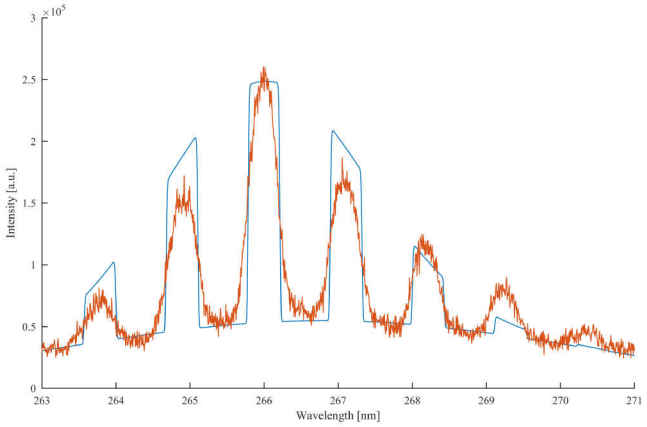

(a)

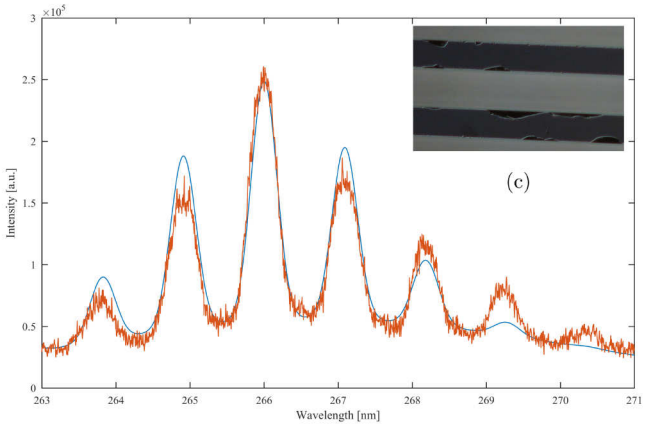

(b)

Figure 4.3: Comparison between the measured pulse spectrum at the XXPS exit (orange) and the simulated spectral distribution (blue). A waist size in the Fourier plane of 5 µm (a) and 75 µm (b) has been assumed. A portion of the surface of a top lamellar mirror is also shown (c).

crystals used in the frequency up-conversion setup. In Figure 4.3 (a) the simulated spectral distribution is calculated assuming a finite beam waist of 5 µm for a monochromatic line in the Fourier plane. This value would only account for geometrical aberrations affecting an ideal Gaussian beam as derived in the optical simulation described in Chapter 3. A Gaussian pedestal is added to the simulation result to fit the incoherent background. While the spectral position of the transmitted light agrees well with the measured data, the shape of the individual peaks as well as the overall spectral envelope are much different. A significantly better simulated spectrum resembling the measured data can be obtained assuming a waist size of 75 µm fwhm for the bundle of rays of a single color, as shown in Figure 4.3 (b). There could be several reasons explaining an increased beam waist: (1) Slight misalignment of the complex pulse shaper optics cannot be excluded completely. (2) The profile of the UV beam might be partially spoiled due to diffraction of the IR pulses at crystal edges in the tripler. With an 800 nm beam diameter of $\sim$ 5 mm, which is comparable to the crystal diameter of 6 mm, diffraction could increase its 'apparent' beam waist in the Fourier plane. Furthermore, (3) the UV spectrometer resolution and (4) imperfections of the striped mirror particularly due to damaged reflecting edges are not accounted for. Distortions introduced by the spectrometer are expected to be small, according to previous tests, but the grating resolution must be taken into account. Considering that the beam size at the XXPS exit is in the order of 3 mm, the spectrometer maximum resolution is on the order of 5 pixels, corresponding to about 0.025 nm. Such an effect is negligible with respect to the width of the peaks in Figure 4.3.

It has not been taken into account that the reflecting stripes are, by far, not perfect rectangles. Due to the mechanical processing by means of a rotary diamond saw, surface damage is present close to the edge of the reflecting stripes, with sections of the surface up to tens of µm in width missing. This phenomenon is known as chipping. The extent of the damage on the mirror stripes is shown in Figure 4.3 (c). The surface damage, progressively increasing in quantity close to the edge of the stripes, smooths the edges of the transmitted spectral bands and increases stray light adding up incoherently.

The temporal profile of the shaped pulse has been derived using the same aforementioned simulation code developed by Thurston et al.. In Figure 4.4 the envelope of unshaped pulses Fourier-limited (33 fs fwhm), 60 fs-, 100 fs- and 130 fs-long fwhm at the XXPS entrance are compared to the respective shaped pulses assuming 5 µm and 75 µm focus size in the Fourier plane. When the unshaped pulse time duration is small compared to the peak separation (33 fs and 60 fs with respect to 213 fs peak separation) the

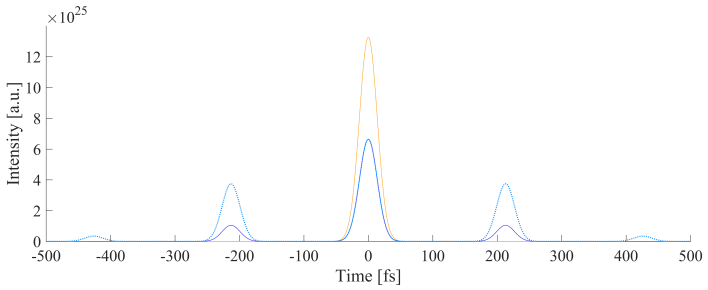

(a)

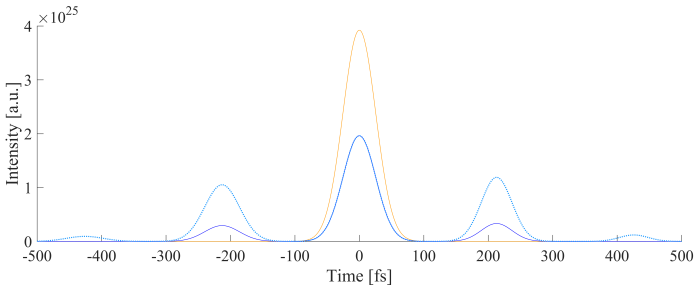

(b)

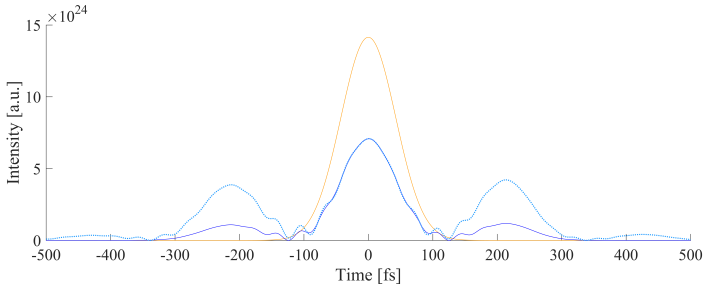

(c)

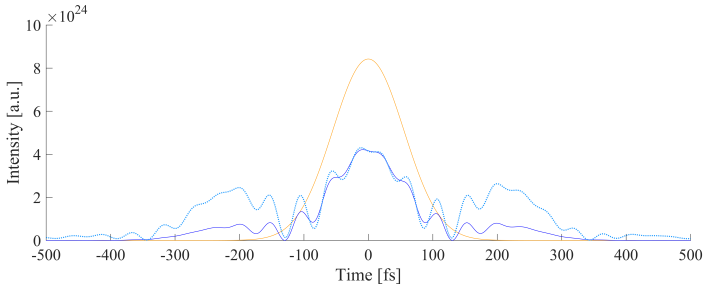

(d)

Figure 4.4: Simulated temporal profile of the shaped pulse with 75 µm (blue) and 5 µm (light blue) focus size in the Fourier plane, compared to the unshaped pulse (orange). Fourier limited (a), 60 fs (b), 100 fs (c) and 130 fs (d) long chirped pulses are used as shaper input.

replicas have a Gaussian shape like the input pulses. When the original time duration is comparable to the peak separation, an interference pattern is generated.
Independently from the initial pulse duration, when the waist of the simulated monochromatic bundle of rays is comparable to the 150 µm spacing between the reflective stripes, the tails of different spectral components centered on the gaps are reflected. The lack of spectral bands completely cut from the pulse spectrum, i.e. the reduced modulation depth, reduces the intensity of pulse replicas in the temporal profile. It results in a triple pulse with faint further lobes beyond the three main peaks.
There is a slight difference in height and width of the side lobes when the pulses are not Fourier limited: it is due to the energy chirp in the unshaped pulse. The well-defined pulse sequence is interesting for dynamic studies on small quantum systems, because the parametrization and tailoring of its time-frequency spectrum is rather simple. It opens up a window of opportunities for coherent control experiments which will become clear in the following.
Some characteristics of the time profile of the shaped pulse can be understood through the use of a simplified analytical model. Under the approximations of linear dispersion in the Fourier plane, perfect spectral resolution and neglectable focus size in the Fourier plane, perfectly flat reflective elements in the Fourier mask and no space between them, the electric field of the shaped pulse can be calculated analytically to be [76]:

$$E_{out}(t) = exp\left(-\pi^2 \delta_g \nu^2 t^2\right) sinc(\pi \delta \nu t) \sum_{n=-N/2}^{N/2-1} A_n B_n exp\left[i\left(\omega_n t + \phi_n\right)\right] \quad (4.3)$$

Here $\delta\nu$ is the dispersion per mask pixel in the Fourier plane, $\delta_g\nu$ is the grating resolution, N is the total number of pixels in the phase mask, A_n and ϕ_n are respectively the amplitude and phase change introduced by the n-th pixel and B_n is the spectral amplitude of the unshaped pulse at the n-th pixel. While such an expression allows for rough estimates on the output pulse temporal properties, the approximations mentioned above limit its usefulness for actual calculation of the expected characteristics, making numerical methods, e.g. the aforementioned one by Thurston et al., mandatory.
The sum in Equation 4.3 is a Fourier series, therefore having the properties that it repeats itself with a period given by the reciprocal of the frequency increment. It follows that it repeats infinitely in time with period $1/\delta\nu$. In practice, due to the non-linear dispersion of the grating the actual period

is given by $1/\delta\bar{\nu}$, where $\delta\bar{\nu}$ is approximately the average of the grating dispersion of the pulse frequencies [76]. In our case the separation between two successive peaks obtained from the simulation is 213 fs, while using the value $\delta\nu$ obtained from Optic Studio software for the central period of the phase mask in the XXPS a value of 248 fs is obtained.
The Gaussian cardinal-sine (*sinc*) window suppresses the pre- and post-pulses far from the central one. Therefore the further the peaks are from the central one, the less intense they are.
The replicas in the shaped pulse have a slightly different time duration compared to the central peak. This effect is due to a different phase modulation induced by the phase mask [76]. The phase change induced by each pixel of the mask on a replica of order R can be calculated analytically, as done by Vaughan et al. in [76]. The most apparent result is a chirp being introduced in the replicas, proportional to the replica order and positive in the pre-pulses, negative in the post-pulses. Due to the interference fringes, this effect is difficult to see on the 130 fs- and 100 fs-long pulses, while it is clear in the 60 fs case. Because a positively chirped pulse has been assumed, this results in a left lobe $R = 1$ with 63.8 fs fwhm time duration and a right lobe $R = -1$ with 56.2 fs time duration.
In a second stage of the experiment, the lamellar mirror has been moved into the Fourier plane along the dispersion axis y. The movement translates to a shift of the position of the reflective elements with respect to the dispersed spectrum of the unshaped pulse. Such experiments have been first performed by Wollenhaupt et al. [77]. The effect can be detected with the UV spectrometer by looking at the changing position of the transmitted bands with respect to the spectrum envelope maximum. The spectrum of twenty pulses taken with $\pi/10$ phase-shift steps is shown in Figure 4.5.
A Gaussian fit of the envelope of the pulses, together with lines indicating the position of the center and 1σ points of the distribution are shown for comparison. The intensity profile and position of the spectra varies slightly due to spectral jitter in the tripler output. The spectra have been filtered through a 5-point moving average filter, in order to reduce the effect of the camera thermal noise on the contour.
In the time domain this manipulation results in the introduction of a phase jump between the central lobe and the side lobes, with a phase increase in the right-lobe equal to the phase decrease in the left-lobe [58], showing coherent control on the shaped pulse characteristics. On the other hand, the change of the shaping mask position has no effect on the intensity or duration of the three main lobes.
The simulated time-profiles of four shaped pulses, with $\pi/2$ phase-shift steps and assuming 60 fs time duration for the unshaped pulse are shown in Figure

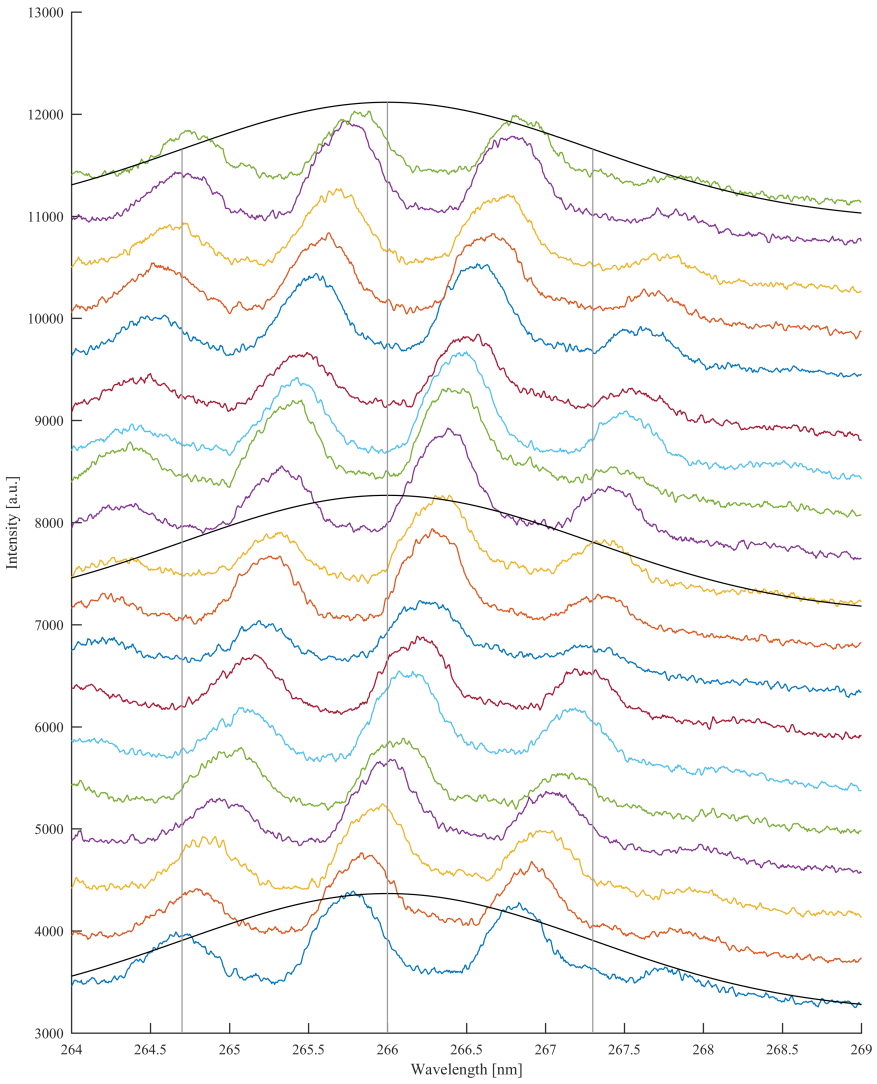

Figure 4.5: Single-shot spectra of the shaped pulses at 20 different lamellar-mirror positions (different spectral amplitude masks), with $1/20$ *of the stripe period separation in the dispersion plane. It can be seen that the spectral modulation shifts together with the mirror position, while the spectral envelope and central wavelength remains constant shot-to-shot but for minor variations due to jitter in the tripler output.*

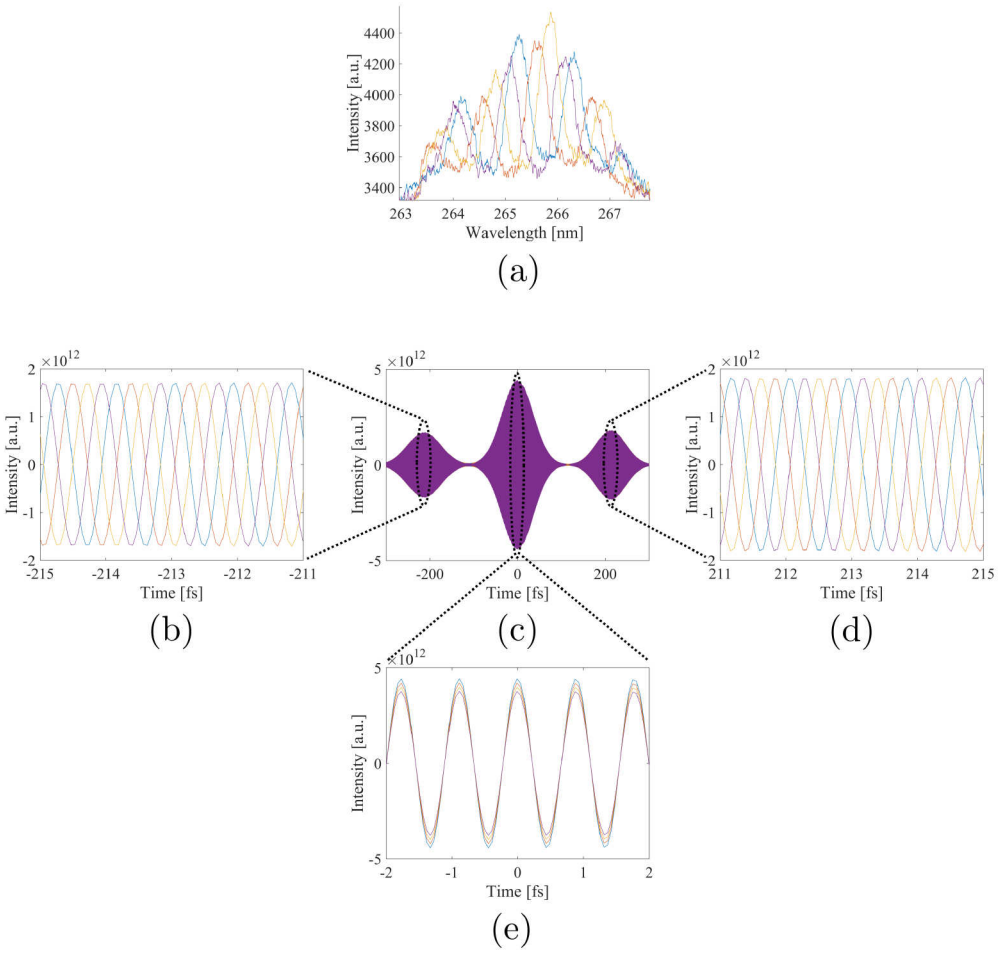

Figure 4.6: Shaping the time-frequency distribution of 60 fs-long UV pulses. Four different shaped pulses, each generated by a quarter stripe-period difference in the shaping mask position (a), have the same temporal electric field envelope (c), but they have different relative phases of the first and last lobe with respect to the central one. While each of the carrier waves are in phase at the peak of the central pulse (e) (the intensity has been scaled in this sub-figure in order for the four waves not to perfectly overlap), in the left (b) and right (d) pulse the phase advance or delay of the carrier is equal to the phase difference in the position of the striped mirror. The spectra shown in (a) are measured single-shot spectra, while the remaining graphs show simulated data.

4.6. The result is different when interference is present due to the relatively small time separation of the replicas. The fringes due to the interference between neighboring lobes move accordingly to the phase change in the side lobes, as can be seen in Figure 4.7.

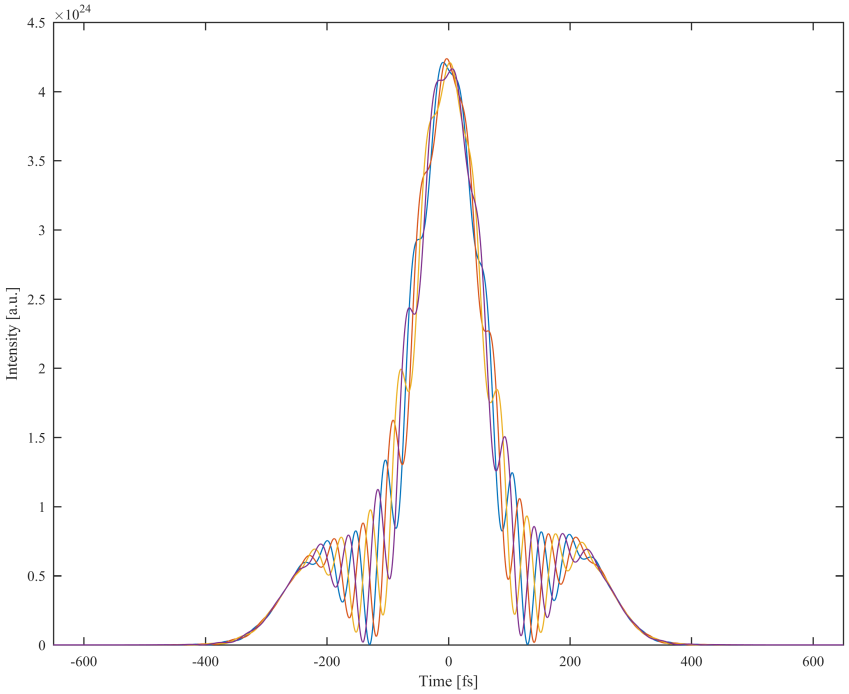

Figure 4.7: Shift in the interference pattern position of 130 fs-long shaped pulses, simulated data. The phase advance is equal to the phase change in the side peaks. The four pulses shown are the same of Figure 4.6.

4.3 First Steps Towards Shaped XUV Pulses

38.1 nm SASE pulse trains of 346 bunches and (2.7 ± 2.2) µJ energy per photon pulse were used during the initial XUV pulse shaper commissioning. This corresponds to an average energy per pulse train of ~ 930 µJ, which is more than ten times higher than the energy measured for single seeded pulses [37]. It is clear that no actual pulse shaping experiments can be performed with SASE pulse trains due to the lack of longitudinal

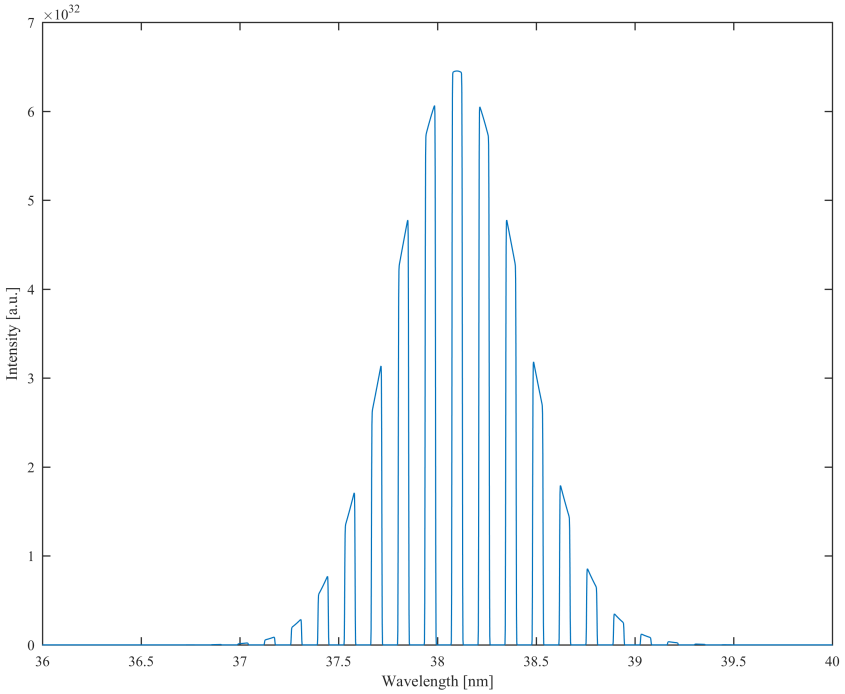

Figure 4.8: Expected accumulated SASE spectrum at the XXPS exit.

coherence and pulse-to-pulse fluctuations of the spectral phases. However, even SASE pulse trains can be used to observe the modulation of the spectral amplitudes induced by the lamellar grating in the Fourier plane. The spatial FEL frequency distribution in the Fourier plane due to dispersion and focusing should not depend on the spectral phases, i.e. the degree of longitudinal coherence. Thus, averaging the spectra from many pulse trains should allow observation of the modulation with the high-resolution XUV spectrometer. Along these lines an analogue experiment to the 266 nm shaping study has been carried out.

The transmission of the current XUV pulse shaper setup including the current status of the beamline has been discussed in Section 3.6. Although the transmission is in the 10^{-5} range, due to the limits of the current off-the-shelves gratings, the first steps with XUV FEL pulses have been taken. Based on the measured XUV spectral bandwidth of $\sim 2\%$, simulations have been carried out to pinpoint the effect of the lamellar grating placed in the Fourier plane of the pulse shaper. Fig. 4.8 shows the expected modulated spectral distribution of the SASE pulses. So far, we have not succeeded in

recording such an amplitude shaped FEL pulse. Diffraction, stray light as well as the current low transmission limits us.
In future, the preliminary commercial XUV Richardson gratings in the 4f setup will be replace by custom-made blazed gratings with a blaze angle tailored to the XXPS operating angle. The increased length of the gratings will also allow for the use of the full 5 mm diameter beam in the pulse shaper. Therefore, the M2 mirror needs to be replaced by a 120 mm-long mirror. These two changes will be important to increase the XXPS output when using sFLASH pulses. It may even allow characterization of the shaped seeded pulses directly in time domain, e.g. by THz streaking. THz streaking of unshaped reference pulses has been already achieved with support by the author of the present thesis [42].

Chapter 5

Conclusions and Outlook

This project had three initial objectives:

1. feasibility study of an **X**UV and soft **x**-ray **p**ulse **s**haper (XXPS) relying on grazing incidence optics within the limits of current technology,

2. designing of the XXPS apparatus,

3. shaped pulse diagnostic development and commissioning strategy.

All three objectives have been successfully achieved. After the initial feasibility study the XXPS has been designed. While a 2 m long compact version of the device has been built, optimized for XUV use down to 15 nm, a longer version with shallower grazing angles and different optics coating will be needed for operation between 15 nm and 4 nm. Both versions are expected to have transmission on the order of 1% in the respective wavelength range, suitable for most experiments at brilliant FEL facilities. The line density and blaze angle of the gratings has been tailored, in order to allow operation of the XXPS at each harmonic of a 266 nm seed laser without realignment. Furthermore, this smart approach enables simultaneous shaping of harmonics of the same fundamental wavelength, enabling e.g. fundamental-third harmonic coherent control experiments like the ones pioneered by Chan, Brumer and Shapiro [78]. The shaper modular design allows for the arbitrary increase of the focus distance in the 4f-geometry by simple means of replacing the focusing optics.
A four-step commissioning strategy has been developed for the shaper, with the first two steps requiring only spectral diagnostics to optimize the alignment of all components, and the last two using diagnostics in the time domain. The author has developed (two high-resolution spectrometers) or contributed to the development (a UV-IR cross-correlator and a THz

streaking setup) of all the necessary hardware. He also contributed to commissioning the sFLASH HGHG seeding scheme, generating longitudinally coherent photon pulses suitable for pulse shaping applications. The XUV version of the XXPS has been built and first 266 nm pulse shaping experiments have been performed using this device. Here, tailored time-frequency spectra have been characterized making use of a home-built high-resolution UV spectrometer achieving coherent control of the pulse temporal profile. The second step of the commissioning phase, focusing on the same kind of experiments performed with 38.1 nm SASE FEL light and an XUV high-resolution spectrometer, has not been successful, yet. The reasons behind the failure will need further investigation, but the culprit seems to be the insufficient spectral and intensity stability of the SASE pulse trains used during the experiment to overcome the low transmission of the temporary off-the-shelves gratings.

Future XUV pulse shaping experiments will make use of the final custom-

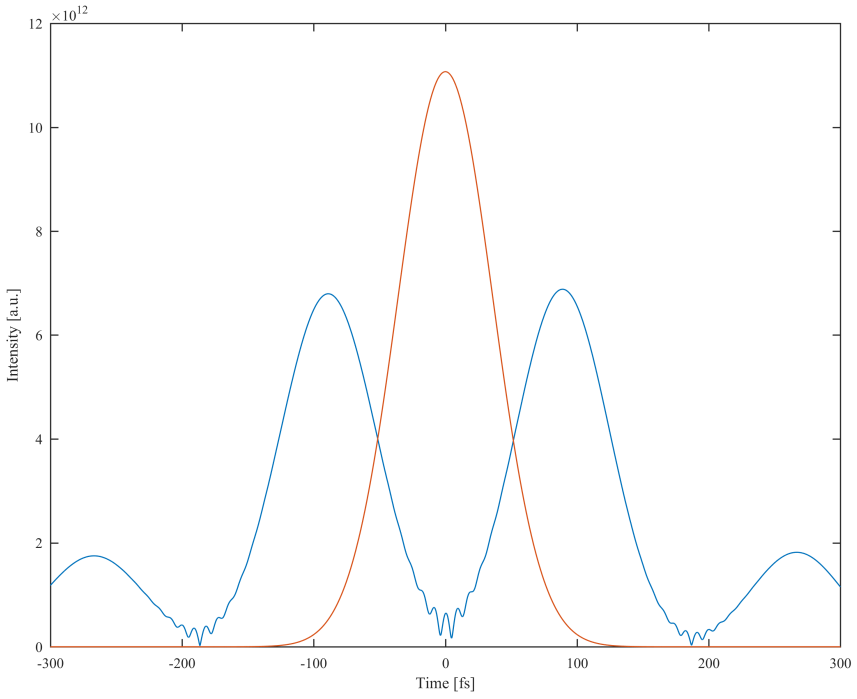

Figure 5.1: Simulated time profile of a double pulse generated using the MEMs mask and a 70 fs-long, 38.1 nm FEL pulse with typical sFLASH characteristics.

designed blazed gratings, in order to have sufficient transmission through the XXPS to perform single-shot experiments with the seeded sFLASH pulses. Finally, a fully-operational XUV optical pulse shaper will be available, generating tailored pulse sequences like those shown in Figure 5.1 and enabling new spectral-phase-sensitive ways of investigating and controlling matter that further extend the photon science capabilities at FELs.

Acknowledgments

This PhD thesis would have never come to be without the many people who supported me in the process. First of all I want to thank my supervisors Tim Laarmann, who came up with the idea of the XUV and soft x-ray pulse shaper and supported my work in countless ways, and Prof. Jörg Rossbach, who brought me to DESY and Universität Hamburg.
My deepest thanks go to the colleagues that during the years worked with me in Tim Laarmann's group at DESY: to Andreas Przystawik, for his constant advice, his help finding flaws in my designs and his support during the shaping experiments, Sergey Usenko, for sharing his ample experience with me and giving me an hand when I needed one, Markus Jakob, for the precious input on laser technology and non-linear crystals, Lena Worbs, for her suggestions concerning how to commission the tripler and Florian Jacobs, for studying the effects of vibrations from the labs on vacuum chambers and how to effectively reduce them.
Furthermore I'd like to thank the many colleagues I had in the sFLASH group, in particular: Jörn Bödewadt, for sharing his vast FEL and sFLASH knowledge and for his guidance during his years as responsible of the sFLASH group, Christoph Lechner, for the constant support during the years with regard to both the theoretical and the experimental side of things, Tim Plath, for aiding me in a variety of matters both FEL-related and not, Sven Akerman, for his teachings on FLASH, Theophilos Maltezopoulos, for sharing with me many good and bad times in the control room and in the laser lab and Prof. Wolfgang Hillert, for supporting the sFLASH group in the past two years.
I also would like to thank the people that helped me in laser-related matters: Armin Azima and Nagitha Ekanayake, for sharing their knowledge on femtosecond lasers with me, Mehdi Mohammad Kazemi, for helping me out countless times with the seed laser and related issues, Bastian Manschwetus and Xuemei Cheng, for coming up with the idea of building an UV-IR cross-correlator and involving me in the development of the device.
Moreover my thanks go to the several students that under my supervi-

sion worked on parts of this project: to Ali Raza, for helping me in the design phase, especially determining the optimal grating characteristics, Jakob Soltau, for helping me studying the relation between seed laser, electron beam parameters and FEL bandwidth, Jan Christoph Thiele, for its contribution to the characterization of the WLI performances, Tobias Abel, for contributing to the writing of the shaping simulation code and Roman Kamyshinskii, for taking part to the assembly and alignment of the XXPS.
In addition I want to thank all the people that built or modified parts of my machines in the DESY mechanical and electrical workshops, the IT division and countless employes from the more than 30 companies that realized components for my experimental devices: while their contribution goes often unmentioned, no experiment would be possible without their help and expertise.
Regarding this written work, I am indebted to Tim Plath, Andreas Przystawik, Sergey Usenko and Markus Jakob for reviewing its chapters. A special thank goes to Sam Hartwell, for carefully reading through its entirety and greatly improving the English side of it.
Last but not least, I want to thank my family and friend, especially my brother and the two Andreas: we came a long way together, I hope different career choices and Brexit will not draw us apart.

Appendix A

XXPS Alignment Procedure

Due to the seven optical elements present and the short wavelengths involved, the alignment of the XXPS is not a trivial task. To achieve good shaping performances, the shaping masks must be positioned precisely in the Fourier plane, with its optical elements parallel to tightly focused, aberration-free monochromatic lines. Downstream of the shaping mask, the shaped spectral components need to be recombined into a beam homogeneously shaped and with a flat wavefront.
Several steps are necessary to align the XXPS. Each of these steps has been studied with the help of an OpticStudio virtual model of the pulse shaper optical elements and of its diagnostics, in order to identify which degrees of freedom have visible effects at each step.
The starting point of the XXPS alignment procedure consists in carefully placing each optical element and degree of freedom at the nominal position. In this configuration each element should be within a few millimeters and one or two degrees of rotation from the optimal position.
The next step consists in aligning all the optical elements with a visible alignment laser and gratings in the 0th order. A single lamellar-mirror should be placed in the Fourier plane for this and the following steps. Such alignments can be better performed without vacuum, checking with a piece of paper where each optic is hit by the beam. The shape of the beam on each screen in the XXPS can be compared with the virtual model. If deemed necessary, the flatness of the beam wavefront at the exit of the XXPS can be inspected with the help of a shear-plate interferometer [79]. While 0th order alignment with an alignment laser is essential for correcting for aberrations, it allows us to find the Fourier plane only approximately, due to the longer wavelength and small beam footprint on the focusing mirrors (see Table A.1).
The third alignment step is performed with pulsed light. Ideally the longest

XXPS Focus size				
Wavelength	**Grat. Order**	**Beam Diam.** (mm)	Focus (µm)	Rayleigh L. (mm)
638 nm (Al. Laser)	0	2	34	5.5
	0	5	13	0.88
266 nm	0	2	14	2.3
	0	5	5.6	0.37
	1	2	2.9	0.10
	1	5	1.2	0.016
38 nm	0	2	2.0	0.3
	0	5	0.80	0.053
	1	2	0.39	0.012
	7	5	0.17	0.0023

Table A.1: Comparison between Focus size and Rayleigh length of the beam in the Fourier plane for different wavelengths and input beam diameters. For 266 nm results are given for the test grating, with the final custom gratings they will be within a few % from the given values. For 38 nm the 2 mm beam result is given for the test beam, the 5 mm one for the final grating.

wavelength that can be shaped with the grating-coating configuration in use should be utilized first. The light is aligned still in the 0th order through the XXPS to the reference points on the screens individuated with the alignment laser. The light at the XXPS exit is sent to a high resolution spectrometer, in order to check for the absence of disturbing effects in the spectrum reading and to get a reference spectrum.
The fourth step consists in rotating the two grating to the working dispersion order, aligning them so that the dispersed beam is still going through the same path of the alignment laser. According to the virtual pulse shaper simulations, the right alignment of the dispersion lines in the Fourier plane can be checked at this point with good precision with the help of the screens. The resulting alignment is sufficient to make the effects of the remaining aberrations in the Fourier plane neglectable for pulse shaping performances.
The fifth step consists in using the spectrometer to align the lamellar mirror in the Fourier plane, optimizing the contrast between transmitted bands and cut bands. Such an alignment allows us to precisely determine the position of the Fourier plane.
The sixth and final step consists in placing the final shaping mask in place of the mirror, and use the spectrometer to optimize the alignment as in the previous step by maximizing the contrast of the spectral components

partially cut by the small gaps between the reflective elements of the mask. After this step, the XXPS is fully aligned and the actual pulse shaping can be performed.

List of Figures

List of Tables

Bibliography

[1] C. Brif, R. Chakrabarti, and H. Rabitz, "Control of quantum phenomena: past, present and future," *New Journal of Physics*, vol. 12, p. 075008, 2010.

[2] G. De Ninno, D. Gauthier, B. Mahieu, P. c. v. R. Ribič, E. Allaria, P. Cinquegrana, M. B. Danailov, A. Demidovich, E. Ferrari, L. Giannessi, G. Penco, P. Sigalotti, and M. Stupar, "Single-shot spectro-temporal characterization of XUV pulses from a seeded free-electron laser," *Nature Communications*, vol. 6, p. 8075, 2015.

[3] E. Ferrari, E. Allaria, J. Buck, G. De Ninno, B. Diviacco, D. Gauthier, L. Giannessi, L. Glaser, Z. Huang, M. Ilchen, G. Lambert, A. A. Lutman, B. Mahieu, G. Penco, C. Spezzani, and J. Viefhaus, "Single shot polarization characterization of XUV FEL pulses from crossed polarized undulators," *Scientific Reports*, vol. 5, p. 13531, 2015.

[4] D. Gauthier, P. c. v. R. Ribič, G. De Ninno, E. Allaria, P. Cinquegrana, M. B. Danailov, A. Demidovich, E. Ferrari, L. Giannessi, B. Mahieu, and G. Penco, "Spectrotemporal shaping of seeded free-electron laser pulses," *Phys. Rev. Lett.*, vol. 115, p. 114801, 2015.

[5] F. Bencivenga, R. Cucini, F. Capotondi, A. Battistoni, R. Mincigrucci, E. Giangrisostomi, A. Gessini, M. Manfredda, I. P. Nikolov, E. Pedersoli, E. Principi, C. Svetina, P. Parisse, F. Casolari, M. B. Danailov, M. Kiskinova, and C. Masciovecchio, "Four-wave mixing experiments with extreme ultraviolet transient gratings," *Nature*, vol. 520, pp. 205–208, 2015.

[6] P. Schmüser, M. Dohlus, and J. Rossbach, *Ultraviolet and Soft X-Ray Free-Electron Lasers: Introduction to Physical Principles, Experimental Results, Technological Challenges*. American Physical Society, 2008.

[7] J. D. Jackson, *Classical Electrodynamics*. Wiley, 3rd ed., 1998.

[8] E. Allaria, L. Badano, S. Bassanese, F. Capotondi, D. Castronovo, P. Cinquegrana, M. B. Danailov, G. D'Auria, A. Demidovich, R. De Monte, G. De Ninno, S. Di Mitri, B. Diviacco, W. M. Fawley, M. Ferianis, E. Ferrari, G. Gaio, D. Gauthier, L. Giannessi, F. Iazzourene, G. Kurdi, N. Mahne, I. Nikolov, F. Parmigiani, G. Penco, L. Raimondi, P. Rebernik, F. Rossi, E. Roussel, C. Scafuri, C. Serpico, P. Sigalotti, C. Spezzani, M. Svandrlik, C. Svetina, M. Trovó, M. Veronese, D. Zangrando, and M. Zangrando, "The FERMI free-electron lasers," *Journal of Synchrotron Radiation*, vol. 22, no. 3, pp. 485–491, 2015.

[9] T. J. Orzechowski, B. R. Anderson, J. C. Clark, W. M. Fawley, A. C. Paul, D. Prosnitz, E. T. Scharlemann, S. M. Yarema, D. B. Hopkins, A. M. Sessler, and J. S. Wurtele, "High-efficiency extraction of microwave radiation from a tapered-wiggler free-electron laser," *Phys. Rev. Lett.*, vol. 57, pp. 2172–2175, 1986.

[10] "The european x-ray free-electron laser technical design report," tech. rep., DESY XFEL Project Group, 2007.

[11] I. Ben-Zvi, L. Di Mauro, S. Krinsky, M. White, and L. Yu, "Proposed UV FEL user facility at BNL," *Nuclear Instruments and Methods in Physics Research A*, vol. 304, no. 1-3, pp. 181–186, 1991.

[12] L.-H. Yu, M. Babzien, I. Ben-Zvi, L. F. DiMauro, A. Doyuran, W. Graves, E. Johnson, S. Krinsky, R. Malone, I. Pogorelsky, J. Skaritka, G. Rakowsky, L. Solomon, X. J. Wang, M. Woodle, V. Yakimenko, S. G. Biedron, J. N. Galayda, E. Gluskin, J. Jagger, V. Sajaev, and V. I., "High-gain harmonic-generation free-electron laser," *Science*, vol. 289, no. 5481, pp. 932–934, 2000.

[13] G. Stupakov, "Using the beam-echo effect for generation of short-wavelength radiation," *Phys. Rev. Lett.*, vol. 102, p. 074801, 2009.

[14] Z. T. Zhao, D. Wang, J. H. Chen, Z. H. Chen, H. X. Deng, J. G. Ding, C. Feng, Q. Gu, M. M. Huang, T. H. Lan, Y. B. Leng, D. G. Li, G. Q. Lin, B. Liu, E. Prat, X. T. Wang, Z. S. Wang, K. R. Ye, L. Y. Yu, H. O. Zhang, J. Q. Zhang, M. Zhang, M. Zhang, T. Zhang, S. P. Zhong, and Q. G. Zhou, "First lasing of an echo-enabled harmonic generation free-electron laser," *Nature Photonics*, vol. 6, p. 360, 2012.

[15] L. Yu and I. Ben-Zvi, "High-gain harmonic generation of soft x-rays with the 'fresh bunch' technique," *Nuclear Instruments and Methods in Physics Research A*, vol. 393, no. 1-3, pp. 96–99, 1997.

[16] E. Allaria, D. Castronovo, P. Cinquegrana, P. Craievich, M. Dal Forno, M. B. Danailov, G. D'Auria, A. Demidovich, G. De Ninno, S. Di Mitri, B. Diviacco, W. M. Fawley, M. Ferianis, E. Ferrari, L. Froehlich, G. Gaio, D. Gauthier, L. Giannessi, R. Ivanov, B. Mahieu, N. Mahne, I. Nikolov, F. Parmigiani, G. Penco, L. Raimondi, C. Scafuri, C. Serpico, P. Sigalotti, S. Spampinati, C. Spezzani, M. Svandrlik, C. Svetina, M. Trovo, M. Veronese, D. Zangrando, and M. Zangrando, "Two-stage seeded soft-x-ray free-electron laser," *Nature Photonics*, vol. 7, pp. 913–918, 2013.

[17] E. L. Saldin, E. A. Schneidmiller, and M. V. Yurkov, "Study of a noise degradation of amplification process in a multistage HGHG FEL," *Optics Communications*, vol. 202, no. 1, pp. 169–187, 2002.

[18] P. Finetti, H. Höppner, E. Allaria, C. Callegari, F. Capotondi, P. Cinquegrana, M. Coreno, R. Cucini, M. B. Danailov, A. Demidovich, G. De Ninno, M. Di Fraia, R. Feifel, E. Ferrari, L. Fröhlich, D. Gauthier, T. Golz, C. Grazioli, Y. Kai, G. Kurdi, N. Mahne, M. Manfredda, N. Medvedev, I. P. Nikolov, E. Pedersoli, G. Penco, O. Plekan, M. J. Prandolini, K. C. Prince, L. Raimondi, P. Rebernik, R. Riedel, E. Roussel, P. Sigalotti, R. Squibb, N. Stojanovic, S. Stranges, C. Svetina, T. Tanikawa, U. Teubner, V. Tkachenko, S. Toleikis, M. Zangrando, B. Ziaja, F. Tavella, and L. Giannessi, "Pulse duration of seeded free-electron lasers," *Phys. Rev. X*, vol. 7, p. 021043, 2017.

[19] S. Reiche, *Numerical studies for a single pass high gain free electron laser*. PhD thesis, Universität Hamburg, 2000.

[20] D. Xiang, E. Colby, M. Dunning, S. Gilevich, C. Hast, K. Jobe, D. McCormick, J. Nelson, T. O. Raubenheimer, K. Soong, G. Stupakov, Z. Szalata, D. Walz, S. Weathersby, M. Woodley, and P.-L. Pernet, "Demonstration of the echo-enabled harmonic generation technique for short-wavelength seeded free electron lasers," *Phys. Rev. Lett.*, vol. 105, p. 114801, 2010.

[21] L. T. Campbell and B. W. J. McNeil, "Echoes of photons past," *Nature Photonics*, vol. 10, p. 501, 2016.

[22] V. Ayvazyan, N. Baboi, I. Bohnet, R. Brinkmann, M. Castellano, P. Castro, L. Catani, S. Choroba, A. Cianchi, M. Dohlus, H. T. Edwards, B. Faatz, A. A. Fateev, J. Feldhaus, K. Flöttmann, A. Gamp, T. Garvey, H. Genz, C. Gerth, V. Gretchko, B. Grigoryan, U. Hahn,

C. Hessler, K. Honkavaara, M. Hüning, R. Ischebeck, M. Jablonka, T. Kamps, M. Körfer, M. Krassilnikov, J. Krzywinski, M. Liepe, A. Liero, T. Limberg, H. Loos, M. Luong, C. Magne, J. Menzel, P. Michelato, M. Minty, U.-C. Müller, D. Nölle, A. Novokhatski, C. Pagani, F. Peters, J. Pflüger, P. Piot, L. Plucinski, K. Rehlich, I. Reyzl, A. Richter, J. Rossbach, E. L. Saldin, W. Sandner, H. Schlarb, G. Schmidt, P. Schmüser, J. R. Schneider, E. A. Schneidmiller, H.-J. Schreiber, S. Schreiber, D. Sertore, S. Setzer, S. Simrock, R. Sobierajski, B. Sonntag, B. Steeg, F. Stephan, K. P. Sytchev, K. Tiedtke, M. Tonutti, R. Treusch, D. Trines, D. Türke, V. Verzilov, R. Wanzenberg, T. Weiland, H. Weise, M. Wendt, T. Wilhein, I. Will, K. Wittenburg, S. Wolff, M. V. Yurkov, and K. Zapfe, "A new powerful source for coherent VUV radiation: demonstration of exponential growth and saturation at the TTF free-electron laser," *Eur. Phys. J. D*, vol. 20, no. 1, pp. 149–156, 2002.

[23] W. Ackermann, G. Asova, V. Ayvazyan, A. Azima, N. Baboi, J. Bähr, V. Balandin, B. Beutner, A. Brandt, A. Bolzmann, R. Brinkmann, O. I. Brovko, M. Castellano, P. Castro, L. Catani, E. Chiadroni, S. Choroba, A. Cianchi, J. T. Costello, D. Cubaynes, J. Dardis, W. Decking, H. Delsim-Hashemi, A. Delserieys, G. D. Pirro, M. Dohlus, S. Düsterer, A. Eckhardt, H. T. Edwards, B. Faatz, J. Feldhaus, K. Flöttmann, J. Frisch, L. Fröhlich, T. Garvey, U. Gensch, C. Gerth, M. Görler, N. Golubeva, H.-J. Grabosch, M. Grecki, O. Grimm, K. Hacker, U. Hahn, J. H. Han, K. Honkavaara, T. Hott, M. Hüning, Y. Ivanisenko, E. Jaeschke, W. Jalmuzna, T. Jezynski, R. Kammering, V. Katalev, K. Kavanagh, E. T. Kennedy, S. Khodyachykh, K. Klose, V. Kocharyan, M. Körfer, M. Kollewe, W. Koprek, S. Korepanov, D. Kostin, M. Krassilnikov, G. Kube, M. Kuhlmann, C. L. S. Lewis, L. Lilje, T. Limberg, D. Lipka, F. Löhl, H. Luna, M. Luong, M. Martins, M. Meyer, P. Michelato, V. Miltchev, W. D. Möller, L. Monaco, W. F. O. Müller, O. Napieralski, O. Napoly, P. Nicolosi, D. Nölle, T. Nuñez, A. Oppelt, C. Pagani, R. Paparella, N. Pchalek, J. Pedregosa-Gutierrez, B. Petersen, B. Petrosyan, G. Petrosyan, L. Petrosyan, J. Pflüger, E. Plönjes, L. Poletto, K. Pozniak, E. Prat, D. Proch, P. Pucyk, P. Radcliffe, H. Redlin, K. Rehlich, M. Richter, M. Roehrs, J. Roensch, R. Romaniuk, M. Ross, J. Rossbach, V. Rybnikov, M. Sachwitz, E. L. Saldin, W. Sandner, H. Schlarb, B. Schmidt, M. Schmitz, P. Schmüser, J. R. Schneider, E. A. Schneidmiller, S. Schnepp, S. Schreiber, M. Seidel, D. Sertore, A. V. Shabunov, C. Simon, S. Simrock, E. Sombrowski, A. A. Sorokin, P. Spanknebel,

R. Spesyvtsev, L. Staykov, B. Steffen, F. Stephan, F. Stulle, H. Thom, K. Tiedtke, M. Tischer, S. Toleikis, R. Treusch, D. Trines, I. Tsakov, E. Vogel, T. Weiland, H. Weise, M. Wellhöfer, M. Wendt, I. Will, A. Winter, K. Wittenburg, W. Wurth, P. Yeates, M. V. Yurkov, I. Zagorodnov, and K. Zapfe, "Operation of a free-electron laser from the extreme ultraviolet to the water window," *Nature Photonics*, vol. 1, no. 6, pp. 336–342, 2007.

[24] L. H. Yu, L. Di Mauro, A. Doyuran, W. S. Graves, E. D. Johnson, R. Heese, S. Krinsky, H. Loos, J. B. Murphy, G. Rakowsky, J. Rose, T. Shaftan, B. Sheehy, J. Skaritka, X. J. Wang, and Z. Wu, "First ultraviolet high-gain harmonic-generation free-electron laser," *Phys. Rev. Lett.*, vol. 91, p. 074801, 2003.

[25] A. Singer, I. A. Vartanyants, M. Kuhlmann, S. Duesterer, R. Treusch, and J. Feldhaus, "Transverse-coherence properties of the free-electron-laser FLASH at DESY," *Phys. Rev. Lett.*, vol. 101, p. 254801, 2008.

[26] E. Allaria, R. Appio, L. Badano, W. Barletta, S. Bassanese, S. Biedron, A. Borga, E. Busetto, D. Castronovo, P. Cinquegrana, S. Cleva, D. Cocco, M. Cornacchia, P. Craievich, I. Cudin, G. D'Auria, M. Dal Forno, M. Danailov, R. De Monte, G. De Ninno, P. Delgiusto, A. Demidovich, S. Di Mitri, B. Diviacco, A. Fabris, R. Fabris, W. Fawley, M. Ferianis, E. Ferrari, S. Ferry, L. Froehlich, P. Furlan, G. Gaio, F. Gelmetti, L. Giannessi, M. Giannini, R. Gobessi, R. Ivanov, E. Karantzoulis, M. Lonza, A. Lutman, B. Mahieu, M. Milloch, S. Milton, M. Musardo, I. Nikolov, S. Noe, F. Parmigiani, G. Penco, M. Petronio, L. Pivetta, M. Predonzani, F. Rossi, L. Rumiz, A. Salom, C. Scafuri, C. Serpico, P. Sigalotti, S. Spampinati, C. Spezzani, M. Svandrlik, C. Svetina, S. Tazzari, M. Trovo, R. Umer, A. Vascotto, M. Veronese, R. Visintini, M. Zaccaria, D. Zangrando, and M. Zangrando, "Highly coherent and stable pulses from the FERMI seeded free-electron laser in the extreme ultraviolet," *Nature Photonics*, vol. 6, pp. 699–704, 2012.

[27] J. W. Goodman, *Statistical Optics*. Wiley, 2000.

[28] L. Mandel and E. Wolf, *Optical Coherence and Quantum Optics*. Cambridge University Press, 1995.

[29] R. Ischebeck, J. Feldhaus, C. Gerth, E. Saldin, P. Schmüser, E. Schneidmiller, B. Steeg, K. Tiedtke, M. Tonutti, R. Treusch, and M. Yurkov,

"Study of the transverse coherence at the TTF free electron laser," *Nuclear Instruments and Methods in Physics Research Section A: Accelerators, Spectrometers, Detectors and Associated Equipment*, vol. 507, no. 1, pp. 175–180, 2003.

[30] R. Treusch, C. Gerth, T. Lokajczyk, and J. Feldhaus, "Photon diagnostics on the VUV FEL at DESY: first lasing around 100nm," *Nuclear Instruments and Methods in Physics Research A*, vol. 467, pp. 30–33, 2001.

[31] T. Plath, P. Amstutz, J. Bödewadt, G. Brenner, N. Ekanayake, B. Faatz, K. Hacker, K. Honkavaara, L. L. Lazzarino, C. Lechner, T. Maltezopoulos, M. Scholz, S. Schreiber, M. Vogt, J. Zemella, and T. Laarmann, "Free-electron laser multiplex driven by a superconducting linear accelerator," *Journal of Synchrotron Radiation*, vol. 23, no. 5, pp. 1070–1075, 2016.

[32] T. Maltezopoulos, M. Mittenzwey, A. Azima, J. Bödewadt, H. Dachraoui, M. Rehders, C. Lechner, M. Schulz, M. Wieland, T. Laarmann, J. Roßbach, and M. Drescher, "A high-harmonic generation source for seeding a free-electron laser at 38 nm," *Applied Physics B*, vol. 115, no. 1, pp. 45–54, 2014.

[33] A. E. Siegman, *Lasers*. University Science Books, 1990.

[34] V. G. Dmitriev, G. G. Gurzadyan, and D. N. Nikogosyan, *Handbook of Nonlinear Optical Crystals*. Springer, 3rd ed., 1999.

[35] G. Angelova, V. Ziemann, A. Meseck, P. Salén, P. van der Meulen, M. Hamberg, M. Larsson, J. Bödewadt, S. Khan, A. Winter, H. Schlarb, F. Löhl, E. Saldin, E. Schneidmiller, and M. Yurkov, "Observation of two-dimensional longitudinal-transverse correlations in an electron beam by laser-electron interactions," *Phys. Rev. ST Accel. Beams*, vol. 11, p. 070702, 2008.

[36] P. Salén, M. Hamberg, P. van der Meulen, M. Larsson, G. Angelova-Hamberg, V. Ziemann, H. Schlarb, F. Löhl, E. Saldin, E. Schneidmiller, M. Yurkov, J. Bödewadt, A. Winter, S. Khan, and A. Meseck, "Results from the optical replica synthesizer at FLASH," in *Proceedings of FEL 2009, Liverpool, UK.*, 2009.

[37] T. Plath, P. Amstutz, J. Bödewadt, L. L. Lazzarino, C. Lechner, T. Maltezopoulos, V. Miltchev, N. Ekanayake, T. Laarmann, and

J. Rossbach, "Mapping few-femtosecond slices of ultra-relativistic electron bunches," *Scientific Reports*, vol. 7, p. 2431, 2017.

[38] K. Wille, *The Physics of Particle Accelerators, An Introduction.* Oxford University Press, 2001.

[39] H. Wiederman, *Particle Accelerators Physics.* Springer, 3rd ed., 2007.

[40] G. A. Loew and O. H. Altenmueller, "Design and applications of R.F. deflecting structures at SLAC," *SLAC Technical Report SLAC-PUB-135*, p. 511, 1965.

[41] L. L. Lazzarino, E. Di Palma, M. P. Anania, M. Artioli, A. Bacci, M. Bellaveglia, E. Chiadroni, A. Cianchi, F. Ciocci, G. Dattoli, D. Di Giovenale, G. Di Pirro, M. Ferrario, G. Gatti, L. Giannessi, A. Mostacci, P. Musumeci, A. Petralia, V. Petrillo, R. Pompili, J. V. Rau, A. R. Rossi, E. Sabia, C. Vaccarezza, and F. Villa, "Self-amplified spontaneous emission free electron laser devices and nonideal electron beam transport," *Phys. Rev. ST Accel. Beams*, vol. 17, p. 110706, 2014.

[42] A. Azima, J. Bödewadt, O. Becker, S. Düsterer, N. Ekanayake, R. Ivanov, M. M. Kazemi, L. L. Lazzarino, C. Lechner, T. Maltezopoulos, B. Manschwetus, V. Miltchev, J. Müller, T. Plath, A. Przystawik, M. Wieland, R. Assmann, I. Hartl, T. Laarmann, J. Rossbach, W. Wurth, and M. Drescher, "Direct measurement of the pulse duration and frequency chirp of seeded XUV free electron laser pulses," *New Journal of Physics*, vol. 20, no. 1, p. 013010, 2018.

[43] T. Plath, *Measurements and detailed analysis of seeded high-gain free-electron lasers at FLASH.* PhD thesis, Universität Hamburg, 2017.

[44] U. Frühling, M. Wieland, M. Gensch, T. Gebert, B. Schütte, M. Krikunova, R. Kalms, F. Budzyn, O. Grimm, J. Rossbach, E. Plönjes, and M. Drescher, "Single-shot terahertz-field-driven x-ray streak camera," *Nature Photonics*, vol. 3, pp. 523–528, 2009.

[45] J. Hebling, G. Almási, I. Z. Kozma, and J. Kuhl, "Velocity matching by pulse front tilting for large-area THz-pulse generation," *Opt. Express*, vol. 10, no. 21, pp. 1161–1166, 2002.

[46] U. Frühling, "Light-field streaking for FELs," *Journal of Physics B: Atomic, Molecular and Optical Physics*, vol. 44, no. 24, p. 243001, 2011.

[47] S. Ackermann, A. Azima, S. Bajt, J. Bödewadt, F. Curbis, H. Dachraoui, H. Delsim-Hashemi, M. Drescher, S. Düsterer, B. Faatz, M. Felber, J. Feldhaus, E. Hass, U. Hipp, K. Honkavaara, R. Ischebeck, S. Khan, T. Laarmann, C. Lechner, T. Maltezopoulos, V. Miltchev, M. Mittenzwey, M. Rehders, J. Rönsch-Schulenburg, J. Rossbach, H. Schlarb, S. Schreiber, L. Schroedter, M. Schulz, S. Schulz, R. Tarkeshian, M. Tischer, V. Wacker, and M. Wieland, "Generation of coherent 19- and 38-nm radiation at a free-electron laser directly seeded at 38 nm," *Phys. Rev. Lett.*, vol. 111, p. 114801, 2013.

[48] J. Bödewadt, R. Assmann, N. Ekanayake, B. Faatz, I. Hartl, M. M. Kazemi, T. Laarmann, C. Lechner, A. Przystawik, P. Amstutz, A. Azima, M. Drescher, W. Hillert, L. L. Lazzarino, T. Maltezopoulos, V. Miltchev, T. Plath, J. Rossbach, K. Hacker, S. Khan, N. Lockmann, and R. Molo, "Experience in operating sFLASH with high-gain harmonic generation," in *Proc. 8th International Particle Accelerator Conference, Copenhagen*, 2017.

[49] B. E. A. Saleh, *Fundamentals of Photonics*. Wiley, 2nd ed., 2007.

[50] A. Monmayrant, S. Weber, and B. Chatel, "A newcomer's guide to ultrashort pulse shaping and characterization," *Journal of Physics B: Atomic, Molecular and Optical Physics*, vol. 43, no. 10, p. 103001, 2010.

[51] R. Thurston, J. Heritage, A. Weiner, and W. Tomlinson, "Analysis of picosecond pulse shape synthesis by spectral masking in a grating pulse compressor," *IEEE Journal of Quantum Electronics*, vol. 22, no. 5, pp. 682–696, 1986.

[52] D. Goswami, "Optical pulse shaping approaches to coherent control," *Physics Reports*, vol. 374, no. 6, pp. 385–481, 2003.

[53] S.-H. Shim and M. T. Zanni, "How to turn your pump-probe instrument into a multidimensional spectrometer: 2D IR and Vis spectroscopies via pulse shaping," *Phys. Chem. Chem. Phys.*, vol. 11, pp. 748–761, 2009.

[54] Y. Silberberg, "Quantum coherent control for nonlinear spectroscopy and microscopy," *Annual Review of Physical Chemistry*, vol. 60, no. 1, pp. 277–292, 2009.

[55] K. T. Hartinger, S. Nord, and P. Monkhouse, "Temperature- and pressure-dependent absorption coefficients for CO2 and O2 at 193 nm," *Applied Physics B*, vol. 70, no. 1, pp. 133–137, 2000.

[56] D. Bigourd, B. Chatel, W. P. Schleich, and B. Girard, "Factorization of numbers with the temporal talbot effect: Optical implementation by a sequence of shaped ultrashort pulses," *Phys. Rev. Lett.*, vol. 100, p. 030202, 2008.

[57] H. P. Sardesai, C. C. Chang, and A. M. Weiner, "A femtosecond code-division multiple-access communication system test bed," *Journal of Lightwave Technology*, vol. 16, no. 11, pp. 1953–1964, 1998.

[58] T. Laarmann, I. Shchatsinin, P. Singh, N. Zhavoronkov, C. P. Schulz, and I. V. Hertel, "Femtosecond pulse shaping as analytic tool in mass spectrometry of complex polyatomic systems," *Journal of Physics B: Atomic, Molecular and Optical Physics*, vol. 41, no. 7, p. 074005, 2008.

[59] C. Froehly, B. Colombeau, and M. Vampouille, "Shaping and analysis of picosecond light pulses," *Progress in Optics*, vol. 20, pp. 63–153, 1983.

[60] C. Bocchetta, D. Bulfone, P. Craievich, M. B. Danailov, G. D'Auria, G. DeNinno, S. D. Mitri, B. Diviacco, M. Ferianis, A. Gomezel, F. Iazzourene, E. Karantzoulis, F. Parmigiani, G. Penco, M. Trovo, J. Corlett, W. Fawley, S. Lidia, G. Penn, A. Ratti, J. Staples, R. Wilcox, A. Zholents, W. Graves, F. O. Ilday, F. Kaertner, D. Wang, T. Zwart, M. Cornacchia, P. Emma, Z. Huang, and J. Wu, "FERMI @ ELETTRA - a seeded harmonic cascade FEL for EUV and soft x-rays," in *Proceedings of FEL2005, Stanford, California, US.*, 2005.

[61] E. L. Saldin, E. A. Schneidmiller, and M. V. Yurkov, "Longitudinal space charge-driven microbunching instability in the TESLA test facility linac," *Nuclear Instruments and Methods in Physics Research Section A: Accelerators, Spectrometers, Detectors and Associated Equipment*, vol. 528, no. 1-2, pp. 355–359, 2004.

[62] G. Penco, E. Allaria, L. Badano, P. Cinquegrana, P. Craievich, M. Danailov, A. Demidovich, R. Ivanov, A. Lutman, L. Rumiz, P. Sigalotti, C. Spezzani, M. Trovó, and M. Veronese, "Optimization of a high brightness photoinjector for a seeded FEL facility," *Journal of Instrumentation*, vol. 8, p. 05015, 2013.

[63] H. Wang, P. Bencok, P. Steadman, E. Longhi, J. Zhu, and Z. Wang, "Complete polarization analysis of an APPLE II undulator using a soft x-ray polarimeter," *Journal of Synchrotron Radiation*, vol. 19, no. 6, pp. 944–948, 2012.

[64] E. Allaria, B. Diviacco, C. Callegari, P. Finetti, B. Mahieu, J. Viefhaus, M. Zangrando, G. De Ninno, G. Lambert, E. Ferrari, J. Buck, M. Ilchen, B. Vodungbo, N. Mahne, C. Svetina, C. Spezzani, S. Di Mitri, G. Penco, M. Trovó, W. M. Fawley, P. R. Rebernik, D. Gauthier, C. Grazioli, M. Coreno, B. Ressel, A. Kivimäki, T. Mazza, L. Glaser, F. Scholz, J. Seltmann, P. Gessler, J. Grünert, A. De Fanis, M. Meyer, A. Knie, S. P. Moeller, L. Raimondi, F. Capotondi, E. Pedersoli, O. Plekan, M. B. Danailov, A. Demidovich, I. Nikolov, A. Abrami, J. Gautier, J. Lüning, P. Zeitoun, and L. Giannessi, "Control of the polarization of a vacuum-ultraviolet, high-gain, free-electron laser," *Phys. Rev. X*, vol. 4, p. 041040, 2014.

[65] E. Ferrari, C. Spezzani, F. Fortuna, R. Delaunay, F. Vidal, I. Nikolov, P. Cinquegrana, B. Diviacco, D. Gauthier, G. Penco, P. c. v. R. Ribič, E. Roussel, M. Trovó, J.-B. Moussy, T. Pincelli, L. Lounis, M. Manfredda, E. Pedersoli, F. Capotondi, C. Svetina, N. Mahne, M. Zangrando, L. Raimondi, A. Demidovich, L. Giannessi, G. De Ninno, M. B. Danailov, E. Allaria, and M. Sacchi, "Widely tunable two-colour seeded free-electron laser source for resonant-pump resonant-probe magnetic scattering," *Nature Communications*, vol. 7, p. 10343, 2016.

[66] B. L. Henke, E. M. Gullikson, and J. C. Davis, "X-ray interactions: photoabsorption, scattering, transmission, and reflection at E=50-30000 eV, Z=1-92," *Atomic Data and Nuclear Data Tables*, vol. 54, no. 2, pp. 181–342, 1993.

[67] M. Zhang and Y. Nakayama, "Effect of ultraviolet light irradiation on amorphous carbon nitride films," *Journal of Applied Physics*, vol. 82, no. 10, pp. 4912–4915, 1997.

[68] T. Gebert, D. Rompotis, M. Wieland, F. Karimi, A. A., and D. M., "Michelson-type all-reflective interferometric autocorrelation in the VUV regime," *New Journal of Physics*, vol. 16, p. 073047, 2014.

[69] S. Usenko, A. Przystawik, L. L. Lazzarino, M. A. Jakob, F. Jacobs, C. Becker, C. Haunhorst, D. Kip, and T. Laarmann, "Split-and-delay

unit for FEL interferometry in the XUV spectral range," *Applied Sciences*, vol. 7, no. 6, p. 544, 2017.

[70] X. Yang, H. Li, Q. Bi, L. Su, and J. Xu, "Growth of large-sized Ce:YAG scintillation crystal by the temperature gradient technique (TGT)," *Journal of Crystal Growth*, vol. 311, no. 14, pp. 3692–3696, 2009.

[71] S. Usenko, A. Przystawik, L. L. Lazzarino, M. A. Jakob, G. Brenner, S. Toleikis, C. Haunhorst, D. Kip, and T. Laarmann, "Attosecond interferometry with self-amplified spontaneous emission of a free-electron laser," *Nature Communications*, vol. 8, p. 15626, 2017.

[72] G. E. Hale and F. L. O. Wadsworth, "Theory of the objective spectroscope," *Astrophysical Journal*, vol. 4, p. 54, 1896.

[73] R. W. Boyd, *Nonlinear Optics*. Academic Press, 3rd ed., 2008.

[74] D. E. Aspnes and A. A. Studna, "Dielectric functions and optical parameters of Si, Ge, GaP, GaAs, GaSb, InP, InAs, and InSb from 1.5 to 6.0 eV," *Phys. Rev. B*, vol. 27, pp. 985–1009, 1983.

[75] A. D. Rakić, "Algorithm for the determination of intrinsic optical constants of metal films: application to aluminum," *Appl. Opt.*, vol. 34, no. 22, pp. 4755–4767, 1995.

[76] J. C. Vaughan, T. Feurer, K. W. Stone, and K. A. Nelson, "Analysis of replica pulses in femtosecond pulse shaping with pixelated devices," *Opt. Express*, vol. 14, no. 3, pp. 1314–1328, 2006.

[77] M. Wollenhaupt, A. Präkelt, C. Sarpe-Tudoran, D. Liese, T. Bayer, and T. Baumert, "Femtosecond strong-field quantum control with sinusoidally phase-modulated pulses," *Phys. Rev. A*, vol. 73, p. 063409, 2006.

[78] C. K. Chan, P. Brumer, and M. Shapiro, "Coherent radiative control of IBr photodissociation via simultaneous (ω1,ω3) excitation," *The Journal of Chemical Physics*, vol. 94, no. 4, pp. 2688–2696, 1991.

[79] M. E. Riley and M. A. Gusinow, "Laser beam divergence utilizing a lateral shearing interferometer," *Appl. Opt.*, vol. 16, no. 10, pp. 2753–2756, 1977.